

Inelastic Hydrogen Atom Scattering from Semiconductor Surfaces

Dissertation

zur Erlangung des mathematisch-naturwissenschaftlichen Doktorgrades
„Doctor rerum naturalium“
der Georg-August-Universität Göttingen

im Promotionsprogramm Chemie
der Georg-August University School of Science (GAUSS)

vorgelegt von
Kerstin Krüger
aus Langenhagen

Göttingen, 2023

Betreuungsausschuss:

Prof. Dr. Alec M. Wodtke

Institut für Physikalische Chemie, Georg-August-Universität Göttingen

Prof. Dr. Dirk Schwarzer

Max-Planck-Institut für Multidisziplinäre Naturwissenschaften, Göttingen

PD Dr. Oliver Bünermann

Institut für Physikalische Chemie, Georg-August-Universität Göttingen

Mitglieder der Prüfungskommission:

Referent:

Prof. Dr. Alec M. Wodtke

Institut für Physikalische Chemie, Georg-August-Universität Göttingen

Korreferent:

Prof. Dr. Dirk Schwarzer

Max-Planck-Institut für Multidisziplinäre Naturwissenschaften, Göttingen

Weitere Mitglieder der Prüfungskommission:

Prof. Dr. Burkhard Geil

Institut für Physikalische Chemie, Georg-August-Universität Göttingen

Prof. Dr. Christian Jooß

Institut für Materialphysik, Georg-August-Universität Göttingen

J. Prof. Dr. Daniel Obenchain

Institut für Physikalische Chemie, Georg-August-Universität Göttingen

Prof. Dr. Martin Suhm

Institut für Physikalische Chemie, Georg-August-Universität Göttingen

Tag der mündlichen Prüfung: 01.06.2023

Abstract

The adiabatic approximation is widely applied to describe interactions of atoms and molecules with solid surfaces. It assumes that the electronic system stays in the lowest-energy ground state during the interaction and energy is exclusively distributed via lattice vibrations in the solid. However, in case of light hydrogen atoms, it predicts inefficient energy transfer to the atoms of heavier solids, contradicting experimental findings of inelastic H atom scattering from germanium surfaces. Germanium is an elemental semiconductor and, unlike frequently studied metals, does not have partly-filled electronic states around the Fermi level, but filled and empty states separated by a fundamental energy gap, the band gap. Using H atom beams with incidence translational energies ranging from around 0.4 eV to more than 6 eV, a non-adiabatic scattering channel is observed at high energy-losses, provided that the incidence energy exceeds the value of the surface band gap. This scattering channel is studied at a variety of experimental conditions, including H/D isotope substitution, varying surface temperatures and different surface structures, leading to the conclusion that it involves electronic interband excitations of the semiconductor surface. An electronically adiabatic low energy-loss channel is consistently observed at all scattering conditions.

Contents

Abstract	iii
1 Introduction	1
2 Surface properties of germanium	7
2.1 Structural and electronic properties	11
2.2 Temperature dependence	21
2.3 Hydrogenated surfaces	24
3 Experimental setup	29
3.1 The H atom scattering apparatus	29
3.2 The transfer system	32
3.3 Ultraviolet and vacuum-ultraviolet photolysis	34
4 Hydrogen atom scattering from germanium surfaces	43
4.1 Evidence of adiabatic and non-adiabatic energy transfer	43
4.2 The isotope effect: H and D atom scattering	55
4.3 The influence of surface temperature	65
4.4 The influence of surface structure: Ge(100) vs. Ge(111)	81
4.5 Scattering from hydrogenated Ge(111)	93
5 Conclusion and Outlook	101
List of Abbreviations	108
Bibliography	109
Acknowledgments	127
List of Publications	131

1 Introduction

Adsorption is the process by which a particle – an atom, ion or molecule – sticks to a surface. Prior to adsorption, that particle has been in gaseous or liquid phase, possessing a certain amount of translational energy. To adsorb on the surface, it needs to get rid of this energy and – lacking other possibilities – usually transfers the energy to the surface. This energy transfer is essential for the process of adsorption. However, on an atomic scale, it is not always fundamentally understood. How do the atoms move and which forces are acting upon them? What are the possibilities for energy dissipation within the surface? How important are the specific properties of the surface?

These questions are of central interest in the field of chemical dynamics at surfaces. Inelastic hydrogen (H) atom scattering experiments carried out under well-defined conditions represent one approach to provide answers, while reducing the complexity of the system as much as possible using the simplest atom as a probing particle.

Adsorption of atomic hydrogen is not only the simplest reaction in surface chemistry but its initial study by Irving Langmuir in 1912 also marked the advent of the era of modern surface science in general. Langmuir observed that molecular hydrogen gets dissociated on a hot tungsten wire, producing atomic hydrogen, which then adsorbs on the glass walls of the vessel used to carry out the experiment [1]. Of course, alongside adsorption, reactivity on surfaces can involve more steps, the so-called elementary steps of a surface reaction. These include dissociation, diffusion, bond formation and desorption, making surface reactions increasingly complex when compared to reactions proceeding in the gas phase only. Again, it was Langmuir who suggested to use well-defined plane surfaces in scientific studies in order to simplify the complex systems as much as possible and gain insight on the fundamental principles underlying surface reactions [2]. However, even for the simplest surface reaction one could think of, there are two major differences when compared to a gas phase reaction. Firstly, the solid is a possible source or drain of energy that cannot be ignored in the study of surface reactions. Secondly, the number of particles is huge due to the presence of a surface, which increases the dimensionality of the system and complicates its description by theoretical models.

Nonetheless, a close collaboration between experimental and theoretical chemistry has been essential for our current understanding of dynamics at surfaces. From experimen-

1 Introduction

tally validated theoretical simulations, we can draw a detailed picture of the mechanisms proceeding on an atomic level. Furthermore, a model that has shown to provide accurate results for a particular system can potentially be used to make predictions on a related system, too, expanding our knowledge of gas-surface interactions.

Since the discovery of quantum mechanics more than a century ago, the physical laws governing chemical reactions have been understood in great detail. However, as soon as more than two nuclei are involved in a system, or, very commonly, more than one electron is involved, an analytical solution of the quantum mechanical equations is unknown. In addition, for large-size systems, numerical solutions are intractable, too, despite the huge advances in computational capability that have been made over the last decades. For practical applications, theoretical chemistry therefore relies on simplifications and approximations.

The Born-Oppenheimer approximation (BOA), formulated by Max Born and Robert Oppenheimer in 1927, is one of the most fundamental approximations and widely applied in theoretical chemistry [3, 4]. Based on the different timescales of nuclear and electronic motion, it assumes that the electronic configuration of a system readjusts instantaneously to a change of the nuclear configuration. Following this, the Schrödinger equation can be separated into an electronic and a nuclear part, which allows the calculation of electronic energies as a parametric function of the nuclear coordinates. From this, a so-called potential energy surface (PES) for the respective system can be constructed.

To theoretically predict the dynamics of a chemical system, a threefold approach is commonly applied. Firstly, the potential energy of the system is calculated for various geometric arrangements using electronic structure methods. Secondly, an appropriate analytical function is fitted to the data, providing a direct functional relation between the atomic configuration and its energy, essentially forming an analytic expression of the PES. In the final step, the PES is used as a basis for calculating the dynamics of the system, i.e., the forces acting upon the particles affecting their motion as well as the energy exchange between them. Here, another approximation is widely applied, propagating the nuclear degrees of freedom classically by applying Newton's equations of motion instead of treating them quantum mechanically. Nuclear quantum effects, such as tunneling or zero point energies, are neglected in molecular dynamics simulations based on the classical approximation. However, particularly for small particles, such as hydrogen atoms or molecules, nuclear quantum-mechanical effects can be important [5]. To deal with the large number of nuclear degrees of freedom typically involved in surface chemistry, approximations of reduced dimensionality may also be required, neglecting for example surface atom motion [6], restricting the dynamics of reacting particles to

specific surface sites [7], or treating only a subset of molecular degrees of freedom [8]. Last but not least, calculations of the potential energies are mostly restricted to methods based on density functional theory (DFT) as higher-level quantum chemistry methods, commonly used in simpler gas phase problems, are not feasible for the typical system sizes required to model surface reactions.

To test the applicability of approximations employed in theoretical simulations, the outcome of these simulations is compared to the results of experiments performed under well-defined conditions to mimic those applied theoretically. In this regard, numerous studies have focused on the validity of the BOA for particle-surface interactions studying energy dissipation at surfaces. Within the BOA, dynamics on a so-called electronically adiabatic PES cannot capture any electronic excitations induced by nuclear motion and energy is solely distributed via lattice vibrations (phonons) within the solid. In contrast, for electronically non-adiabatic processes, the nuclear motion is not restricted to the electronic ground state of the system and can lead to electronic excitation of the surface. While there are many systems that perfectly comply with the BOA, meaning that electronic excitations can be fully ignored or play at most a very minor role [9–13], there is also striking experimental evidence that, in other systems, they cannot be ignored, leading to a so-called BOA breakdown [14–20]. In general, the probability for adiabatic behavior of a system increases with increasing energetic separation of its electronic states. Moreover, the nuclei of the system must move sufficiently slowly, so that the electrons can adjust completely to their motion [21]. Due to their continuum of electronic states, metal surfaces have been frequently used in research studies aimed at testing the validity of the BOA, typically combined with small atoms and molecules colliding with these surfaces at high incidence translational energies. In this regard, inelastic H atom scattering turned out to be perfectly suited to unmask electronically non-adiabatic effects [16, 22–25]. Due to its low mass, an electronically adiabatic picture predicts inefficient energy transfer between H atoms and the atoms of most solids, so that energy-losses due to non-adiabatic effects can be easily identified. In addition, H atoms only possess translational degrees of freedom. Compared to molecules that can also rotate and vibrate, H atoms as probing particles reduce the complexity of the scattering process. Furthermore, being one of the simplest model systems for energy conversion at surfaces, H atom scattering is particularly attractive for comparison of high-level experiments and theories.

As early as 1979, Nørskov and Lundqvist predicted that electronic excitations must be considered to explain high adsorption probabilities of light adsorbates, such as hydrogen atoms, on heavy substrates, such as metal surfaces, where the phonon contribution to energy dissipation is rather small due to the large mass difference of adsorbate and

1 Introduction

substrate [26]. According to a simple collinear binary collision model based on momentum and translational energy conservation, an H atom colliding with an atom of a gold surface is expected to transfer only 2 % of its translational energy per collision, too little to explain its high adsorption probability [16]. Experimentally, however, energy-losses of about 30 % were found. In contrast, H atom scattering from an insulating surface resulted in considerably less energy-loss, that matched the predictions of both the simple binary collision model and an electronically adiabatic molecular dynamics simulation. The energy-loss to the metallic gold surface, on the other hand, can be theoretically modeled by applying molecular dynamics with electronic friction [27, 28]. Electronic friction (EF) is a weak coupling approximation and accounts for non-adiabatic effects by means of frictional and fluctuating forces acting on the nuclei, which are moving on a single, effective PES. Alternatively, independent-electron surface hopping (IESH) [29–32], time-dependent density functional theory (TDDFT) [33] or the Newns-Anderson model [34] are used to account for electronically non-adiabatic effects in theoretical simulations.

As a metal, gold has no band gap between filled and empty electronic states but exhibits partly-filled states around the Fermi level. Resonant electronic intraband excitations are available to couple with translational degrees of freedom associated with the H atom’s nuclear motion. On insulating surfaces, on the other hand, no evidence of electronic excitation induced by H atom scattering has been observed so far [16, 35]. Insulators possess large band gaps between filled and empty states, precluding electronic intraband excitations. In contrast, interband excitations promoting electrons across the band gap may be possible but require impinging particles with incidence energies that exceed the band gap. Still, the question remains whether an energy transfer of several hundred meV or even more from an impinging H atom to a single electron is possible at all. However, in Schottky-diode devices, H atom adsorption on metal surfaces effectively leads to the formation of excited electrons that possess enough energy to surmount the potential barrier of the metal-semiconductor-diode and result in a measurable macroscopic current [36, 37]. Consequently, H atoms can be expected to induce electronic interband excitations in band gap materials, too, given that sufficient incident translational energy is available. Increasing the translational energy of the incident H atoms is technically possible, but challenging experimentally. Alternatively, the width of the band gap can be decreased, introducing another class of solids: semiconductors.

Rather loose definitions of semiconductors comprise their electrical resistivity lying in the range of 10^{-2} to $10^9 \Omega \text{ cm}$ or, alternatively, their band gap being larger than zero and typically smaller than 4 eV [38]. Materials with zero band gap are metals or semimetals, whereas insulators possess even larger band gaps than semiconductors. In a

simple picture, semiconductors can therefore be considered as an intermediate between metals and insulators. Semiconductors occur in many different chemical compositions with a large variety of crystal structures. Perhaps the best-known semiconductor is silicon (Si), an elemental semiconductor. Germanium (Ge) is another elemental semiconductor and silicon's higher homolog. Furthermore, compound semiconductors (e.g. gallium arsenide), layered semiconductors (e.g. molybdenum disulfide), organic semiconductors (e.g. polyacetylene) and magnetic semiconductors (e.g. europium sulfide) can be distinguished [38].

For our everyday life, the importance of semiconductors can hardly be overestimated, as they are essential components of integrated circuits, solar cells and laser diodes. However, semiconductor surface samples were only rarely investigated by atomic or molecular beam surface scattering in the past. Previous experimental studies include rare-gas atom scattering from indium phosphide (InP) surfaces [39, 40], xenon (Xe) atom scattering from Ge(100) [41], nitric oxide (NO) molecular beam scattering from clean [42–44] and oxidized [43–45] Ge(111) as well as NO scattering from oxygen-covered Si(100) [46]. Electronically non-adiabatic effects have been observed in rare-gas atom scattering from semiconductor surfaces [39–41]. Here, hyperthermal rare-gas atoms transfer a substantial amount of their translational energy to the surface atoms and create a local thermal hot spot by phonon excitation. Subsequently, this energy is transferred to electron-hole pair (EHP) excitation within the semiconductor, which leads to the occurrence of a measurable transient current. While this energy dissipation process provides clear evidence of BOA failure within semiconductor samples, the scattering dynamics suggest that the atom-surface collision itself proceeds adiabatically.

In this thesis, energy transfer between H atoms and Ge surfaces is experimentally investigated using inelastic hydrogen atom scattering. Ge is chosen because it is an elemental semiconductor and heavier than Si, which reduces the phonon contribution to energy dissipation and should simplify the separation of purely adiabatic and possibly present non-adiabatic contributions to the observed energy-loss of scattered H atoms. Specifically, Ge(111) and Ge(100) surfaces are investigated in this work. Although the (111) and (100) surface facets of both Si and Ge reconstruct, the (7×7) reconstruction of Si(111) [47, 48] includes more atoms and is more complicated than the $c(2 \times 8)$ adatom structure on Ge(111) [49], which makes the latter a better candidate for theoretical simulations.

To perform high-resolution scattering experiments, H atom beams with narrow velocity distribution are generated by photodissociation of hydrogen halide molecules [50–53] and scattered H atoms are detected using Rydberg atom tagging time-of-flight, a sensitive and accurate method to measure translational energies of H atoms [54, 55].

1 Introduction

Two well-resolved scattering channels are observed for H atoms scattering from Ge surfaces, indeed indicative of electronically adiabatic and non-adiabatic scattering, respectively. This work shows that the electronic structures of germanium surfaces allow a direct discrimination of adiabatic and non-adiabatic scattering channels in one experiment, contrasting H atom scattering from metallic surfaces where both channels are inextricably linked to each other and only one scattering channel is observed. Moreover, it highlights the existence of intraband and interband electronic excitations induced by neutral atom scattering and illustrates the potential of inelastic H atom scattering as a technique to study surface electronic structures.

In view of the long-lasting search for non-Born-Oppenheimer dynamics, H atom scattering from germanium surfaces represents a promising new system, opens new horizons for research into non-adiabatic effects and provides valuable insights to a deeper understanding of surface electronic excitations in atom-surface interactions.

The present work is structured as follows. Chapter 2 gives an introduction to the structural and electronic properties of germanium surfaces with the aim of summarizing – at least partially – the extensive literature on this subject. Chapter 3 describes the experimental setup of the H atom scattering apparatus, focusing on a newly-installed transfer system and the technique of vacuum-ultraviolet photolysis of hydrogen iodide (HI). In Chapter 4, the results of H atom scattering from germanium surfaces are presented. It is comprised of a published article comparing experimental and theoretical results on H atom scattering from Ge(111)*c*(2 × 8), another published article focusing on the investigation of the isotope effect, a draft manuscript addressing the influence of surface temperature, as well as two further sections dealing with the influence of surface structure and surface hydrogenation on H atom scattering from germanium surfaces, respectively. Concluding remarks and prospects of future investigations are given in Chapter 5.

2 Surface properties of germanium

Every solid material is bounded by surfaces. Nevertheless, most of its physical properties can be well described within the model of an infinite solid neglecting the presence of surfaces. This is reasonable for solids of macroscopic size since the number of bulk atoms usually exceeds the number of surface atoms by several orders of magnitude. Furthermore, it is widely assumed that all atoms of the solid contribute equally to commonly studied bulk properties such as transport, mechanical, thermal, magnetic or optical properties. Surface specific properties, on the other hand, are determined by surface atoms only and probed by experimental techniques that are surface sensitive. This includes for example phenomena like crystal growth, adsorption or heterogeneous catalysis that cannot be described by the infinite solid model [56].

For the discussion of surface specific phenomena, a definition of surfaces or, more generally, interfaces is required. The most inclusive definition states that an interface exists in a system if one or several properties of the system abruptly change with distance. Thus, interfaces separate spatial regions of either different matter or matter in different physical states. The particularly simple type of an interface between a solid material and its surrounding atmosphere is called a surface. For a solid crystal sample in ultra-high-vacuum only a few outermost atom layers of the solid belong to the surface. For such a system, typical properties that show sudden changes at the crystal's surface are structure, density and chemical composition [57].

For surface atoms, the number of nearest atoms is reduced compared to the bulk. Consequently, the arrangement of surface atoms frequently differs from the atomic positions within the bulk to stabilize the surface structure and therefore reduce its total energy. Surface relaxation refers to a change in the position of the surface atoms relative to the bulk position, commonly resulting in smaller interlayer spacings between the surface and outermost bulk layers. The bulk unit cell, however, is preserved at the surface. In contrast, surface reconstruction refers to a change in the two-dimensional structure of the surface layer, forming a new surface unit cell that differs from the bulk unit cell. The origin and characteristics of surface reconstructions on elemental semiconductors are one of the most intensively discussed topics in surface physics. The presumably most famous surface reconstruction is that of the Si (111) surface facet showing a large (7×7)

2 Surface properties of germanium

unit cell. Its discovery more or less marks the beginning of surface crystallography on semiconductors [58].

”Semiconductor surfaces were the launching platform for the solid state electronic revolution” [59].

This statement by Harry C. Gatos, founder of the journal *Surface Science*, illustrates the tremendous technological relevance of semiconductor surfaces that started in the 1940s with the invention and construction of the first transistor made from Ge [60], which was the key semiconductor at that time. In the 1960s and 1970s, Ge was gradually replaced by Si, which was easier to produce and handle. Most importantly, Si forms a thin, stable, and passivating silicon dioxide layer that assures chemical stability of the surface. Germanium dioxide on the other hand is soluble in water, which complicates both cleaning and handling processes. Reliable and permanent stabilization of Ge surfaces could not be ensured and consequently the solid state research focused on Si to produce durable and reproducible devices. Nowadays, Si clearly dominates the microelectronic industry [59]. However, Ge made a comeback with the invention of silicon-germanium (SiGe) alloy structures grown on Si substrates that form the basis of exceptionally high-speed transistors, while remaining compatible with existing manufacturing methods [61].

Si and Ge are both group IV elemental semiconductors and exhibit indirect bulk band gaps of 1.13 eV [62] and 0.664 eV [63], respectively, at 290 K. Both elements crystallize in the diamond cubic lattice structure that can be described as two interpenetrating face-centered cubic (fcc) crystals which are displaced relative to each other along the body diagonal. The electronic configuration of the Ge atom is $1s^2 2s^2 2p^6 3s^2 3p^6 3d^{10} 4s^2 4p^2$. The two 4s and two 4p electrons behave as valence electrons. For adjacent atoms, maximum overlap of wavefunctions is achieved when four new wavefunctions are formed by a linear combination of the original 4s, $4p_x$, $4p_y$, and $4p_z$ -orbitals forming four new sp^3 -hybrid orbitals. Accordingly, each atom is tetrahedrally coordinated in the bulk and forms covalent bonds with its four nearest neighbors. The lattice constant of Ge is $a_0 = 5.658 \text{ \AA}$ at 298 K [64]. If the diamond lattice is cut, covalent bonds break and some of the surface atoms are left unsaturated. Their broken bonds are called dangling bonds. Additional adatoms and the formation of surface dimers reduce the density of dangling bonds and, accordingly, the total energy of the surface. This is the major driving force for the formation of reconstructions on elemental semiconductor surfaces. The existence of dangling bonds introduces surface states and surface resonances in the electronic band structure of the semiconductor. Surface states are located in the fundamental bulk band gap. Surface resonances, on the other hand, are surface associ-

ated features lying within the surface projected bulk bands. On the ideally terminated bulk-like semiconductor surface, dangling bonds are initially occupied by one quarter of the respective valence electrons. Upon surface reconstruction, further lowering of the total energy of the surface is achieved by forming filled and empty dangling bond states through charge transfer instead of keeping partly-filled surface states. Charge transfer and the saturation of dangling bonds is often associated with changes of bond angles, introducing strain energy that increases the total energy of the surface. For stable surface structures, this strain energy is overcompensated by the energy gain resulting from the reduction of the number of dangling bonds and charge transfer processes [65].

A variety of surface analysis methods are available to study semiconductor surfaces. In the following paragraph, methods that are mentioned in the subsequent chapters and sections are briefly described. However, many more experimental techniques exist, which are omitted here.

Diffraction methods such as low-energy electron diffraction (LEED) utilize elastic scattering of electrons to characterize the atomic structure of surfaces, visualizing for example surface reconstructions. For LEED, the de Broglie wavelength of the used electrons fulfills the atomic diffraction condition and lies in the order of interatomic distances. Surface sensitivity is ensured by a very short mean free path of the low-energy electrons of only a few atomic layers [66].

Electron spectroscopy methods such as photoelectron spectroscopy (PES), Auger electron spectroscopy (AES) and electron energy loss spectroscopy (EELS) are used to probe the electronic structure of a surface sample. In PES and AES, energy spectra of secondary electrons emitted by surface atoms are analyzed. Bombarding the surface with photons (PES) or electrons (typically used in AES) creates secondary electrons with energies in the range of 5 – 2000 eV. The relatively short mean free path of these electrons in the solid establishes the surface sensitivity of the methods; however, bulk contributions cannot usually be avoided.

PES is the most commonly used technique to study the electronic structure of occupied states at the surface. Based on the photoelectric effect, an electron that is initially in a certain electronic state absorbs a photon and leaves the solid material with a kinetic energy that depends on the photon energy, the work function of the solid and the binding energy of the electronic state which shall be determined. Thus, the obtained photoemission spectrum contains information on the energy and density of occupied states in the probed material. In angle-resolved photoelectron spectroscopy (ARPES), photoemission spectra are recorded as a function of the polar angle with respect to the surface normal. This provides additional information on the momentum dependency

2 Surface properties of germanium

and therefore dispersion of the occupied electronic states [66].

AES is mainly used to analyze the chemical composition of a sample by measuring the energies of electrons generated through the Auger process. Here, a primary electron removes a core electron, creating a hole, and both electrons leave the atom. The hole is filled by an electron from a higher lying level, leaving the atom in a highly excited state. From this it relaxes to a lower energy state by either non-radiative transition, leading to Auger electron emission, or radiative transition, resulting in X-ray fluorescence. The kinetic energy of the ejected Auger electrons depends on the binding energies of the energy levels involved and is therefore element-specific. Hence, AES is suitable to identify contaminants on surfaces [66].

EELS analyzes the energy losses of inelastically scattered electrons after interaction with a solid sample. An electron passing through a material can lose some of its kinetic energy to induce an electron transition from an occupied to an empty state. Conventional EELS typically deals with energy losses ranging from a few eV to about 100 eV originating from electronic interband transitions as well as excitation of plasmons. EEL spectra usually contain both bulk and surface components. For a semiconductor sample, an electronic interband transition involves the excitation of an electron from an occupied bulk valence band or surface state to an empty state above the band gap. This allows the identification of unoccupied states, which is not possible using conventional PES. In core level EELS, excitation sources with higher primary energies are used to study core level excitation in particular. In contrast, EELS performed at low primary energies of less than 20 eV and high energy resolution is called high-resolution EELS and additionally provides the possibility to study surface phonons and vibrational modes of atoms and molecules adsorbed on the surface [66].

Microscopy methods are used to produce real space images of surfaces that contain information on the surface crystallography, morphology and composition. Various microscopy techniques are available, however, only scanning tunneling microscopy (STM) is described here. STM allows the acquisition of surface images with atomic resolution. Therefore, an atomically sharp metal tip is placed closely above the probed surface. The gap between the tip and the surface is about 5 – 10 Å. Applying a bias voltage between the tip and the sample establishes a tunneling current through the gap that greatly depends on the gap width. Since the tunneling current is determined by summing over electronic states of the probe material in the energy interval defined by the bias voltage, scanning the tip along the surface probes the local density of states (LDOS) on the surface. A positive tip bias voltage with respect to the sample probes the filled electronic states, i.e., the STM image corresponds to a surface map of occupied states. On the other hand, with a negative tip bias voltage, an image of the empty states is

obtained. Thus, STM is sensitive to both changes in the LDOS and changes in the surface topography. Maxima can correspond to either topographical protrusions on the surface or an increased LDOS [66]. In scanning tunneling spectroscopy (STS), STM images are recorded with changing tip bias voltage to measure the LDOS as a function of electron energy. Overall, STM is a very powerful tool for the study of both structural and electronic properties of surfaces.

The following sections give an overview of the structural and electronic properties of the Ge(111) and Ge(100) surfaces obtained using different surface analysis methods (Section 2.1). The effects of surface temperature (Section 2.2) and adsorption of hydrogen atoms (Section 2.3) on the structural and electronic surface properties are also discussed.

2.1 Structural and electronic properties

Ge(111)

Cleaving a germanium single crystal along the (111) surface facet at room temperature leads to the formation of a metastable (2×1) surface reconstruction that displays a tilted chain-like structure [58, 67]. Upon heating to about 370 – 470 K, the (2×1) structure irreversibly converts into the Ge(111) $c(2 \times 8)$ surface reconstruction [66, 68]. The presence of three domains rotated by 120° to each other and oriented along three different, but equivalent, directions at the surface leads to the commonly observed characteristic LEED pattern of the Ge(111) $c(2 \times 8)$ surface [49], which is shown in Fig. 2.6 (a) in Section 2.3.

The $c(2 \times 8)$ structure was first proposed by Chadi and Chiang in 1981 and can be described by an adatom model in which a quarter of a monolayer of Ge adatoms occupy one of the two types of three-fold surface sites on the ideal bulk-like terminated Ge(111) (1×1) surface, namely the T_4 sites [49]. The atop T_4 site is located above a second layer Ge atom, whereas the H_3 hollow site resides above a Ge atom of the fourth layer [65, 66]. As pure adatom surface with underlying bulk-like layers, the formation of Ge(111) $c(2 \times 8)$ requires additional Ge atoms. The $c(2 \times 8)$ structure has a 12.5% larger surface atom density than the ideal (1×1) structure or the tilted chain-like (2×1) structure. This need for more atoms leads to the formation of bilayer-deep holes on large and flat terraces of the surface [68]. Fig. 2.1 shows a model of the atomic structure of the $c(2 \times 8)$ reconstructed surface. Each adatom (large solid circles) binds to three formerly unsaturated atoms (unfilled circles) of the first layer and saturates their dangling bonds while the adatom itself possesses only one. In total, the number of

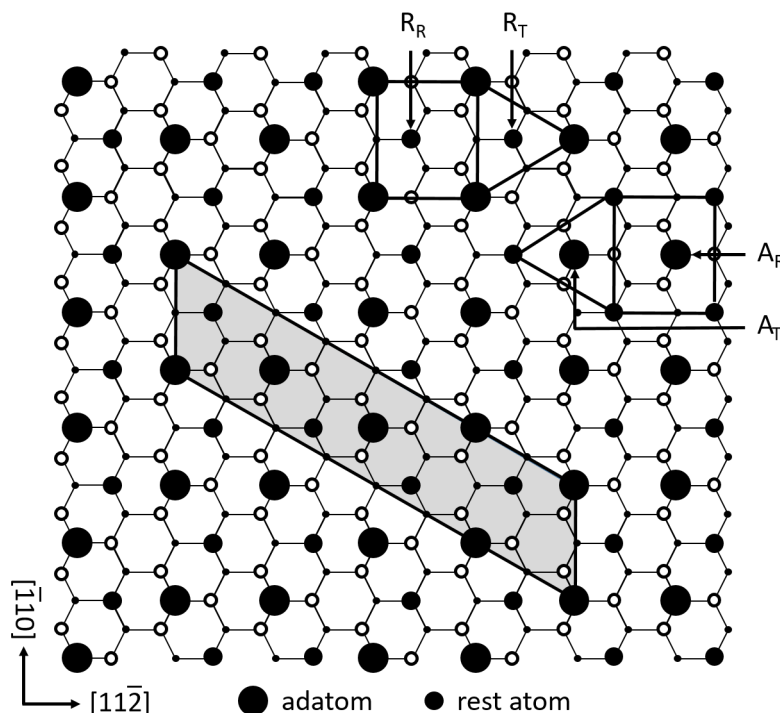


Figure 2.1: Model of the reconstructed Ge(111) $c(2 \times 8)$ surface. Large solid circles depict adatoms, medium-sized solid circles are rest atoms. Unfilled circles represent surface atoms saturated by adatoms, and the smallest solid circles depict saturated backbond atoms. There are two different kinds of adatoms (rest atoms). One kind is symmetrically surrounded by three rest atoms (adatoms), A_T (R_T), and the other one is asymmetrically surrounded by four rest atoms (adatoms), A_R (R_R). A $c(2 \times 8)$ surface unit cell is marked by a gray shaded rhomboidal shape. Each unit cell contains four adatoms and rest atoms, respectively.

dangling bonds per surface unit area is reduced by a factor of 2 for the Ge(111) $c(2 \times 8)$ surface compared to the ideal (1×1) structure, thereby lowering the total energy and stabilizing the surface. Surface atoms that preserve their dangling bonds are referred to as rest atoms (medium-sized solid circles).

The $c(2 \times 8)$ structure is constructed of alternating stacking of hexagonal (2×2) and rectangular $c(2 \times 4)$ subunit cells [69] leading to two types of rest atoms and adatoms, respectively, with different local environments. One type of adatoms (A_T) or rest atoms (R_T) is symmetrically surrounded by three rest atoms or adatoms, respectively, arranged in a triangle. The other type (A_R or R_R) is asymmetrically surrounded by four atoms forming a rectangle as shown in Fig. 2.1. The inequivalency of the rest atoms was experimentally observed by STM [70, 71]. *Ab-initio* molecular dynamics (AIMD)

[72] and DFT [73] calculations were used to determine the atomic arrangement and charge density distribution within the $c(2 \times 8)$ unit cell, confirming the inequivalency of the rest atoms, whereas the adatoms were found to be nearly equivalent. Moreover, bond angles that deviate from the ideal tetrahedral angle and lateral displacements were found leading to a strain-induced increase of the total energy of the surface [72]. Adatom backbonds on (111) surfaces of diamond cubic structure are heavily bent and these distortions can propagate into layers beneath the surface [65]. However, for stable surfaces like the $c(2 \times 8)$ -reconstructed Ge(111) surface, this increase in energy is overcompensated by the lowering of the band structure energy due to the reduction of the number of dangling bonds [65].

The electronic band structure of the Ge(111) $c(2 \times 8)$ surface has been investigated in several theoretical and experimental studies. Experimentally, surface states can be determined using techniques such as ARPES and STM.

Several ARPES studies from the 1980s focused on determining the electronic band structure of occupied surface states on Ge(111) $c(2 \times 8)$ [74–78]. One of these studies [78] identified four bands of occupied surface states that were partially found to split up in a more recent study from 2009, which combines ARPES and STM measurements with theoretical band structure calculations. A total of seven occupied surface states were identified, as shown in Fig. 2.2 [71].

The uppermost surface band A1, close to the Fermi energy E_F , has backbond character and originates from layers below the adatoms and rest atoms. It is found to be very delocalized in both planar and vertical directions [71, 72]. A2 and the slightly lower lying state A2' are localized in the vicinity of the R_R and R_T rest atoms, respectively, and exhibit dangling bond character [71]. A3 is assigned to rest atom dangling bonds as well, as it lies close to the R_T state A2'. However, A3 is only observed within the projected bulk band region and may therefore be influenced by bulk emission, too. More recent results of DFT calculations assign A3 to composite R_T dangling bond and backbond states as well as states corresponding to a mixture of both adatom and rest atom backbonds [73]. In contrast to A3, A4 and A4' are only observed in the (1×1) projected bulk band gap which supports an interpretation of pure surface-state character. A4 and A4' are associated with the A_T and A_R backbonds. Similar to the split of the rest atom dangling bond bands A2 and A2', A4 and A4' may result from a difference in the backbond states of the two types of adatoms. However, A4 and A4' could not be definitively assigned to one of the two types of adatoms, respectively [71]. Finally, A5 is found to be primarily comprised of A_T and A_R backbonds, too [73].

While the majority of STM studies focuses on the topography and atomic arrangement

2 Surface properties of germanium

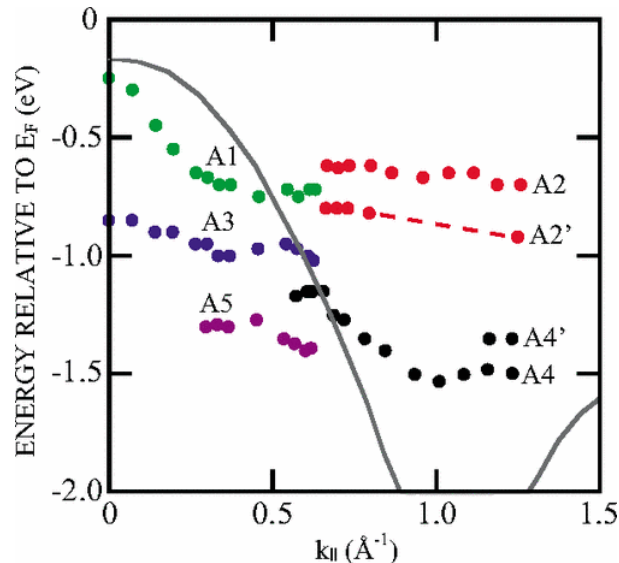


Figure 2.2: Energy dispersions, $E(k_{\parallel})$, of the $\text{Ge}(111)c(2 \times 8)$ surface states. Seven surface states (A1, A2, A2', A3, A4, A4', and A5) are observed on the surface along the $[10\bar{1}]$ azimuth. The solid line shows the upper edge of the bulk band structure projected onto a (1×1) surface Brillouin zone. Reprinted figure with permission from Ref. [71]. Copyright 2009 by the American Physical Society.

of the surface, it is also possible to draw conclusions concerning the electronic band structure from STM images recorded at different bias voltages. Filled state STM images are recorded at positive tip bias voltage, whereas empty state images are obtained at negative voltages.

In an early STM study, the obtained images showed protrusions matching either exclusively rest atoms, when probing the filled surface states, or solely adatoms, when probing empty states [79]. This leads to the conclusion that the surface is further stabilized by a complete charge transfer from the adatom dangling bonds to the rest atom dangling bonds, which are both present in equal numbers per unit area. This results in a semiconducting surface with filled and empty surface states localized at the rest atoms and adatoms, respectively. Subsequent STM studies, however, found adatom contributions in filled state images, indicating that either the electron transfer from the adatom dangling bonds to the rest atom dangling bonds is not complete or other occupied states exist that contribute to the adatom surface charge density. [70, 71, 80]. This becomes apparent in Fig. 2.3 (b) showing a filled state STM image of $\text{Ge}(111)c(2 \times 8)$. The primary occupied surface state is predominantly localized at the rest atom sites. However, adatoms are visible, too, resulting in the appearance of a hexagonal structure that is marked in Fig. 2.3 (b). As previously mentioned, surface state A1 is described to be

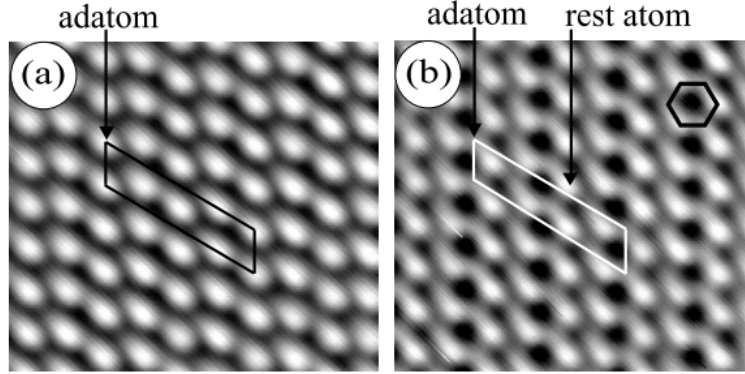


Figure 2.3: Empty (a) and filled (b) state STM images of the Ge(111) $c(2 \times 8)$ surface. The images were recorded at room temperature at a tip bias voltages of -1.2 V (a) and $+1.2$ V (b) and a tunneling current of 0.1 nA. The size of the images is $61 \times 67 \text{ \AA}^2$, respectively. Reprinted figure with permission from Ref. [71]. Copyright 2009 by the American Physical Society.

very delocalized. This is in good agreement with the results of voltage-dependent STM measurements that found an occupied surface state without dangling bond character to be situated between the Fermi level and the occupied rest atom bands. Its associated charge is found to be distributed over both adatoms and rest atoms. Accordingly, adatoms and rest atoms simultaneously appear in filled state images although the filled dangling bonds are localized at the rest atom positions only. Due to the topographically higher position of the adatoms compared to the rest atoms, adatoms are even found to be the dominant feature in filled state STM images at relatively low bias voltages [80]. In empty state images on the other hand, as shown in Fig. 2.3 (a), only adatoms are consistently visible. The primary unoccupied surface states are therefore strongly localized on the adatom sites. This is confirmed by theoretical calculations that find two surface bands above the Fermi energy, derived from the adatoms of the $c(2 \times 8)$ structure [71, 72].

The surface band gap is bounded by the bulk valence band maximum (VBM) at its lower edge and the minimum of the unoccupied adatom-induced surface band at its upper edge. Using STS, the surface band gap was determined to be 0.49 ± 0.03 eV at a surface temperature of about 30 K [81]. A similar or only slightly smaller value is expected at room temperature since the reconstruction of the surface remains unchanged. However, in principle, the surface band gap decreases with increasing temperature, just as semiconductor bulk band gaps, too.

2 Surface properties of germanium

To conclude, Ge(111) shows a stable $c(2 \times 8)$ surface reconstruction at room temperature and is semiconducting with filled and empty surface states localized at rest atoms and adatoms, respectively. The surface band gap has a width of 0.49 ± 0.03 eV and lies between the bulk VBM and the minimum of the unoccupied adatom-induced surface band.

Ge(100)

The reconstructed Ge(100) surface exhibits a surface unit cell much smaller than the $c(2 \times 8)$ one of the (111) facet, which nevertheless displays plenty of fascinating phenomena.

On the ideally-terminated Ge(100) surface, each surface atom of the first layer binds to two second layer atoms, as shown in Fig. 2.4 a, and therefore also exhibits two dangling bonds. To reduce the number of dangling bonds present on the surface, nearest-neighbor surface atoms pair to form a (2×1) -type surface reconstruction consisting of dimer rows (see Fig. 2.4 b-d) [58]. This reduces the number of dangling bonds by a factor of 2 and lowers the electronic energy of the surface. Two equally populated (2×1) domains, which are rotated by 90° and separated by single layer step edges from each other, are generally observed [82].

The surface dimers are not symmetrically arranged but show an asymmetric, tilted configuration with respect to the surface plane. One of the dimer atoms is depressed inward and the other one is moved outward. The tilt angle of the asymmetric dimers with respect to the surface plane is $16^\circ \pm 3^\circ$ [65, 82]. Such structural rearrangements are accompanied by a rehybridization of the surface bonds and, as a consequence, a rearrangement of surface charge. A threefold coordinated surface atom, which is spatially lowered with respect to the surface plane, changes its backbonds towards more sp^2 -character while its dangling bond becomes more p-like. In contrast, a surface atom that is moved outward exhibits backbonds that are more p-like so that its dangling bond becomes more s-character [65]. Following this rehybridization, electron charge is transferred from the depressed to the raised dimer atoms, which leads to filled dangling bonds on the raised atoms and empty dangling bonds at the electron donating depressed atoms. The energy of the occupied states is lowered whereas the energy of the unoccupied states is increased. As the dimers are tilted from the symmetric to the asymmetric configuration, the total energy of the dimers is therefore reduced and the surface is further stabilized [82]. Symmetric dimerization on the other hand with two equivalent dimer atoms possessing one unpaired electron each would result in a partly-filled surface band. However, STM studies clearly observe tilted dimers [83–86].

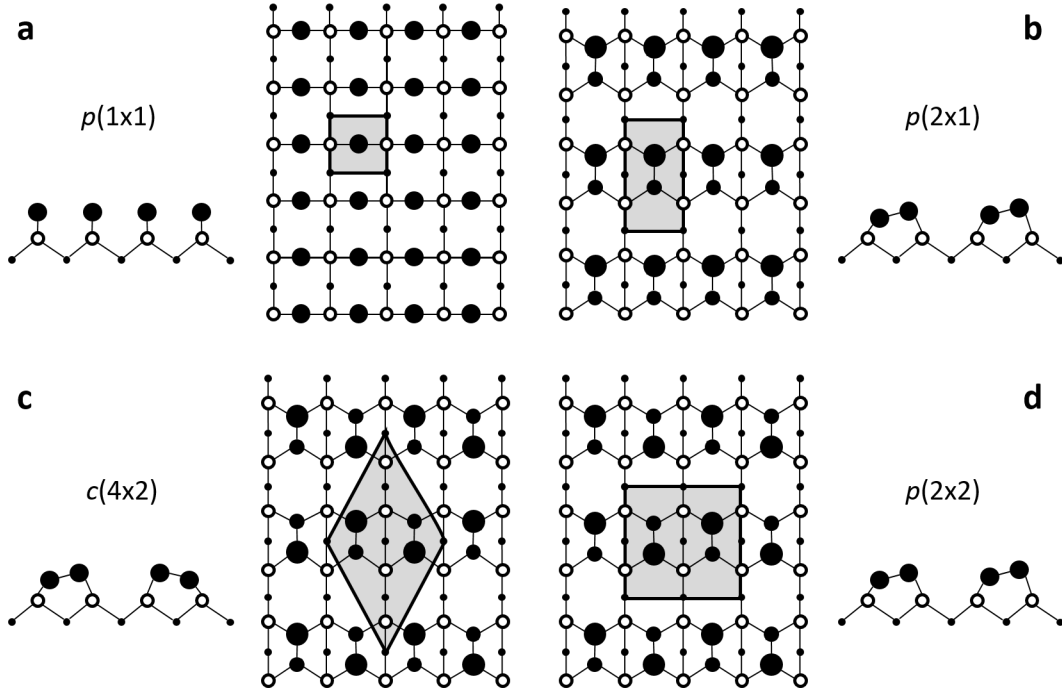


Figure 2.4: Model of the Ge(100) surface illustrating the unreconstructed surface as well as different arrangements belonging to the (2×1) family of reconstructions. Panel a shows the ideal unreconstructed $p(1 \times 1)$ surface in top and side view. Upon surface reconstruction, neighboring top atoms (large solid circles) move together to form asymmetric dimers, thereby saturating dangling bonds. Different arrangements are formed depending on the long-range dimer orientation to each other: panel b shows the $p(2 \times 1)$ surface reconstruction with asymmetric dimers, panel c depicts the $c(4 \times 2)$ surface reconstruction and panel d shows the $p(2 \times 2)$ surface reconstruction. A $p(2 \times 1)$ structure can also be formed out of symmetrical dimers. The surface units cells are marked by gray shaded areas, respectively.

The Ge(100) surface represents a system possessing both a strong short-range interaction leading to dimerization of surface atoms and an energetically weaker long-range interaction that is related to an ordering of the dimers. This gives rise to higher order surface reconstructions belonging to the (2×1) family, such as $c(4 \times 2)$ and $p(2 \times 2)$, in which neighboring dimers are tilted in opposite directions. Since the dimers are spatially separated, the interactions driving the long-range ordering of dimers are energetically weaker (≈ 0.1 eV) than the short-range interactions leading to dimer bond formation (≈ 1 eV) [83]. Out-of-phase adjacent dimer rows lead to a $c(4 \times 2)$ reconstruction (Fig. 2.4c) whereas adjacent rows with dimers that are tilted in-phase form a $p(2 \times 2)$ structure (Fig. 2.4d). *Ab-initio* calculations show that the $c(4 \times 2)$ and $p(2 \times 2)$ structures are energetically nearly degenerate and lower in energy than the asymmetric

2 Surface properties of germanium

$p(2 \times 1)$ configuration which itself is more stable than the symmetric $p(2 \times 1)$ structure [87, 88].

Nevertheless, dimers with a symmetric $p(2 \times 1)$ configuration are still observed in room temperature topographic STM images of Ge(100) [83, 89–93]. This is due to the timescale of the experimental technique, differing from that of atomic motion. Symmetric appearing dimers are actually asymmetric dimers rapidly switching between their two tilted configurations that are symmetrically imaged as a result of time average [89]. This flip-flop motion is suppressed in the vicinity of defects and at step edges so that static asymmetric dimers are also observed at room temperature [83, 90]. Molecular dynamics simulations of the closely related Si(100) surface revealed that the asymmetric and symmetric dimers rapidly interconvert on a subpicosecond timescale. Diffraction, scattering and photoemission events occur on a subfemtosecond timescale and can therefore probe the frozen surface structure. STM on the other hand typically averages the different dimer atom positions within a time period of approximately 0.1 s [94].

Extremely clean and nearly defect-free Ge(100) surfaces typically consist of almost equally populated striped $c(4 \times 2)$ and $p(2 \times 1)$ domains that are several dimer rows wide and occupy the same surface terrace [82, 84]. Fig. 2.5 shows an STM image of such a well-ordered $c(4 \times 2)/(2 \times 1)$ domain pattern with enlarged images of areas of the $p(2 \times 1)$ and $c(4 \times 2)$ reconstructions, respectively [86]. Surfaces on which the concentration of surface defects is higher than $\approx 0.05\%$ with respect to the total number of surface atoms exhibit a more disordered surface structure with coexisting areas of $c(4 \times 2)$, $p(2 \times 2)$, and $p(2 \times 1)$ domains [84].

The electronic band structure of Ge(100) has been extensively studied over the last decades from both an experimental and a theoretical point of view. Nevertheless, several key features of the electronic structure have remained controversial, in particular the question whether the surface is conducting or semiconducting at room temperature as well as the nature of the electronic states at the VBM.

As the surface reconstructs, surface states are expected to appear due to the formation of dimers as well as their asymmetric configuration. In a simple picture, the creation of dimer bonds reduces the surface energy and leads to the formation of two surface states, the bonding σ and the antibonding σ^* states. Furthermore, bonding π and antibonding π^* states are formed by the orbital overlapping of the two dangling bonds at each dimer. Tilting the dimers and the resulting charge transfer from the depressed (D_{down}) to the raised (D_{up}) dimer atoms further lowers the surface energy and leads to filled π bonding states and unoccupied π^* anti-bonding states. π states of the D_{up} lie below the Fermi level E_{F} , while π^* states of the D_{down} are located above E_{F} [85, 86]. Moreover, three

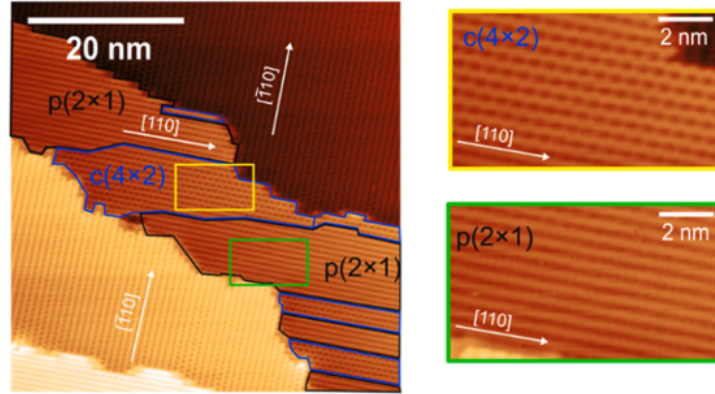


Figure 2.5: STM image of the clean Ge(100) surface showing a highly-ordered $c(4 \times 2)/(2 \times 1)$ domain pattern. The images were recorded at a tip bias voltages of -1 V at room temperature. White arrows indicate the orientation of the dimer rows on each terrace with a rotation of 90° between adjacent terraces. Within one terrace, areas of coexisting $c(4 \times 2)$ and $p(2 \times 1)$ patterns are indicated by blue and black frames, respectively. Enlarged images of $c(4 \times 2)$ and $p(2 \times 1)$ reconstructions are shown on the right side. The size of the original image on the left side is $50 \times 50 \text{ nm}^2$. Reprinted from Ref. [86], Copyright 2021, with permission from Elsevier.

occupied backbond surface states were observed at energies well below the Fermi level, namely 1.15 eV, 1.6 eV, and 3 eV below E_F [95].

Several ARPES studies focused on the nature of the π^* state and its occupation at room temperature in particular, which could entail metallic characteristics of the Ge(100) surface. Early on, the state was observed at an energy below E_F at room temperature. Consequently, it was assigned as a metallic state, which is formed by partially filled bands in the (2×1) domains due to the switching oscillation of the asymmetric dimers [96–98]. Subsequent studies, however, found the same state above E_F at elevated temperatures only, indicating that the π^* state is actually the lowest unoccupied surface state at room temperature. This led to the assignment of a semiconducting nature of the Ge(100) surface. Band gaps of 0.3 eV [99] and 0.44 eV [100] were determined at room temperature. At elevated temperatures, the state becomes thermally occupied and therefore visible in standard ARPES measurements.

Similarly, the nature of the electronic states at the top of the valence band is still under discussion with diverse results leading to interpretations in terms of bulk states [99, 101, 102], backbond surface states [103], or dangling bond surface states [100].

A very recent study re-proved the metallic nature of Ge(100) at room temperature [86]. By means of ARPES measurements, the π^* surface state was observed at 0.2 eV above

2 Surface properties of germanium

the VBM and 0.08 eV above E_F . This excludes the flip-flop motion of the asymmetric dimers within the (2×1) domains as possible origin of the occupied states at room temperature since, in that case, the partially filled bands would have to be located at or slightly below E_F . The surface state disappears at lower measurement temperature and monotonically increases in intensity with rising temperature indicating its occupation by thermally excited electrons [86]. Combining ARPES and STM measurements with first-principle calculations, fundamentally different surface electronic properties were found for the $p(2 \times 1)$ and $c(4 \times 2)$ reconstructions, respectively, potentially explaining previous controversial ARPES results. The electronic properties of the $p(2 \times 2)$ surface were found to be nearly identical to the $c(4 \times 2)$ surface which is due to the fact that the coupling within a dimer row is stronger than that between adjacent rows [86].

Theoretical analysis of the electronic properties of the asymmetric $p(2 \times 1)$ reconstruction revealed an energy gap of 0.5 eV between bulk and surface states, large enough to engender semiconducting behavior of the surface. The π -like states of the D_{up} atoms were found to merge with bulk states at the VBM to become a surface resonance, whereas the π^* surface states of the D_{down} atoms strongly contribute to the surface conduction band edge [86]. For the $c(4 \times 2)$ reconstruction, on the other hand, two surface states of the D_{down} atoms were found within the bulk band gap. One of them is located 0.15 eV above the bulk-like VBM, nearly crossing E_F and closing the surface energy gap. This feature is attributed to the surface state observed in ARPES experiments and might lead to the metallic nature of the surface at room temperature due to the occupation by thermally excited electrons [86].

Theoretically, the valence band structure of Ge(100) was found to be derived from bulk states. This could be proven experimentally as the valence band structure remains clearly resolved after keeping the surface sample 24 h in ultra-high vacuum. The surface state feature located 0.2 eV above the VBM, however, vanishes due to the adsorption of contaminants as expected for a true surface state [86].

To conclude, the Ge(100) surface reconstructs to reduce the number of dangling bonds present on the surface and thereby lowers its electronic energy. Nearest-neighbor surface atoms pair to form rows of asymmetric dimers with one dimer atom raised and the other one lowered with respect to the surface plane. Depending on the long-range order of the dimers, $p(2 \times 1)$, $c(4 \times 2)$, and $p(2 \times 2)$ surface reconstructions exhibiting different electronic properties, are formed. The interactions forcing this longer-range ordering are energetically weaker than those which led to the formation of dimers in the first place. The observed superstructure with its distinctive electronic properties can depend sensitively on minor differences in surface preparation or surface temperature.

This potentially explains why a variety of controversial results concerning the electronic band structure of Ge(100) has been published.

2.2 Temperature dependence

The low-index surfaces of Ge exhibit various reversible structural transitions as a function of surface temperature. Occasionally, atomic rearrangements are accompanied by changing electronic properties. With increasing surface temperature, more thermal energy for short-range surface atom movement is available. With decreasing temperature, weaker long-range forces might become increasingly important driving the transition into new surface structures.

Ge(111)

At room temperature, Ge(111) reconstructs to form a stable $c(2 \times 8)$ structure due to the ordering of a quarter monolayer of Ge adatoms that occupy the T_4 sites of the bulk-like terminated Ge(111) surface. With increasing surface temperature, two reversible structural transitions are observed at 573 K and 1050 K, respectively.

The first transition occurs at 573 K when the $c(2 \times 8)$ structure disorders, forming a structure characterized by an apparent " (1×1) " diffraction pattern with weak half-order spots [104, 105], the so-called moderate-temperature (MT) phase [106]. The symmetry of the $c(2 \times 8)$ reconstruction allows three different orientations of the surface unit cell on the (111)-type bulk substrate leading to the formation of differently oriented domains on the surface. Disordered regions of adatoms start to form at the domain boundaries [107] at about 510 K [108] and grow continuously with increasing temperature until the entire surface exhibits a disordered adatom arrangement at 573 K. The disordering was found to occur by diffusion of adatoms along any of the three equivalent $\langle 01\bar{1} \rangle$ surface directions [107]. At the transition temperature, half-order and eighth-order reflection intensities of the $c(2 \times 8)$ superlattice abruptly disappear in the LEED image leading to an apparent " (1×1) " pattern that nevertheless shows some low-intensity, diffuse half-ordered spots. These are attributed to the formation of an incommensurate (2×2) surface reconstruction that possibly arises from a disordering of the adatoms which then show repulsive interactions [65, 105].

A core-level study of the Ge(111) $c(2 \times 8)$ surface revealed no changes of the energy distribution of electrons photoemitted from Ge 3*d* core levels in the temperature range from 293 to 673 K, i.e., across the characteristic temperature of the structural transition.

2 Surface properties of germanium

This implies that the number of completely occupied dangling bonds at rest atoms is preserved. Adatoms supplying the charge necessary for filling the dangling bonds at the rest atoms are still present above the transition temperature but in a highly disordered arrangement with local short-range (2×2) order [109].

Ge(111) surfaces exhibit a second reversible structural transition at 1050 K, where the MT phase changes into another "(1 × 1)" structure [110], the so-called high-temperature (HT) phase which is observed to be of metallic nature [111–113]. The surface conductivity was found to gradually increase with rising temperature in the range of 600 to 1040 K and exhibits a steplike increase at the characteristic temperature of the second transition. At temperatures above 1050 K, it stays constant up to the bulk melting temperature of 1210 K [111]. Simultaneously, the (2×2) short-range ordering decays with increasing temperature above 573 K, however the adatom diffusion was found to be rather slow and adatoms are still mostly located on stable T_4 sites.

The HT phase of Ge(111) at $T \geq 1050$ K has been extensively studied by both experimental and theoretical approaches, yet two controversial descriptions exist. The first model assumes a laterally diffusive, quasi-liquid-like and metallic Ge surface bilayer due to incomplete surface-melting, supported by experimental results from photoemission and photoabsorption spectroscopy [114] as well as medium-energy ion scattering experiments [115]. In contrast, the second model assumes a structurally well-defined surface that exhibits reduced surface corrugation. It is consistent with an ordered metallic solid state and supported by experimental results from X-ray diffraction [116] and helium atom scattering [117–119]. Furthermore, using quasi-elastic helium atom scattering, the concentration of mobile adatoms on the surface was found to increase significantly at the high-temperature transition modifying the electronic structure of the surface towards metallic behavior. Additionally, the surface is found to be less corrugated, which reduces the diffusion barrier and leads to an extremely high adatom mobility [119].

In summary, the first structural transition leading to the formation of the MT phase is of order-disorder type and occurs at 573 K. The originally ordered adatom structure becomes disordered, yet the number of adatoms present on the surface remains the same while their long-range order is lost. The second transition at 1050 K leads to the formation of the HT phase and results in full surface metallization. The surface structure of the HT phase is still controversial. Experimental results indicate either an order-disorder type behavior at the transition leading to a liquid-like surface layer or an order-order type behavior that results in a structurally well-defined surface above the transition temperature.

Ge(100)

The Ge(100) surface shows an apparently simple (2×1) -type surface reconstruction at room temperature. However, it was found to be highly complex and challenging to interpret in terms of its electronic structure. Nearest-neighbor surface atoms pair to form dimers to reduce the number of dangling bonds present on the surface. Long-range ordering of the dimers gives rise to higher order surface reconstructions belonging to the (2×1) family. As a function of surface temperature, Ge(100) twice changes its character as it possesses a low-temperature transition at 220 K and a high-temperature transition at about 950 K.

The low temperature transition on Ge(100) was first observed by means of ARPES measurements as the metallic surface state close to the Fermi level E_F gradually disappears with decreasing temperature [96] leading to a semiconducting surface at low temperatures. An onset of the metallic peak was found at 220 K. This metal-to-semiconductor transition was found to be coincident with a structural transition of the Ge(100) surface, changing from a (2×1) reconstruction to an ordered $c(4 \times 2)$ structure [96, 97]. However, as described in Section 2.1, surface domains showing a $c(4 \times 2)$ reconstruction are also observed at room temperature [84–86] and the metallic surface state was found to be occupied by thermally excited electrons [86]. Naturally, this occupation declines with decreasing temperature.

Nevertheless, the $c(4 \times 2)$ reconstruction clearly predominates at low surface temperatures, which implies the existence of a driving force that promotes the formation of this structure. It is assumed that the remaining dangling bonds on the dimer atoms interact weakly with those on nearest-neighbor dimers leading to a short-range coupling that drives the $c(4 \times 2)$ ordering. Moreover, it was found that the ordering occurs in two stages, initially along one dimer row and then perpendicular to it [97].

A high-temperature reversible structural transition of the Ge(100) surface was first observed by surface X-ray diffraction measurements to occur at $955 \text{ K} \pm 7 \text{ K}$. Upon transition, the surface reconstruction changes from the (2×1) configuration to a (1×1) structure, which was explained by the creation of adatoms and vacancies on the surface inducing a breakup of the surface dimer bonds [120]. Subsequent studies confirmed the reversible nature of the transition occurring within a temperature range of 900 to 1100 K [121–124]. However, controversial interpretations concerning its physical properties exist. Apart from dimer breakup, a model based on domain wall proliferation was proposed [121, 122]. This model is in agreement with the results of both valence band and core-level photoemission spectroscopy arguing that the number of surface dimers is conserved upon transition [125]. Later on, this was disproved as the dimer concentra-

2 Surface properties of germanium

tion on the surface was found to vary from 100% to less than 1% during the transition [124]. In fact, the physical origin of the $(2 \times 1) \rightarrow (1 \times 1)$ transition was explained by a thermally excited breakup of dimer bonds. This reduces the dimer concentration and consequently the lateral interactions on the surface, which leads to a decrease in step tension and thereby promotes step proliferation, reconciling both descriptions of the transition [123]. Thus, the (2×1) long-range order is lost upon transition and simultaneously the surface roughness is found to increase with rising temperature [122, 126]. This is followed by an irreversible surface roughening at temperatures above 1130 K [123, 126]. Once heated above that temperature, it becomes impossible to restore the original (2×1) configuration upon cooling.

The electronic structure of the Ge(100) surface was investigated by valence band photoemission spectroscopy within a temperature range spanning from room temperature up to almost bulk melting temperature [127]. As expected for a semiconductor, the surface becomes increasingly metallic with rising temperature as the emission at the Fermi level continuously increases in intensity up to the transition temperature of about 960 K. At higher temperatures, it stays nearly constant implying no further change of the surface electronic structure.

In summary, an ordered $c(4 \times 2)$ structure is the most stable reconstruction on semiconducting low-temperature Ge(100) surfaces. At room temperature, $c(4 \times 2)$, $p(2 \times 2)$, and (2×1) structures are found and the surface is metallic due to a surface state near the Fermi level E_F that is occupied by thermally excited electrons. With rising temperature, the surface becomes increasingly metallic until at about 950 K the (2×1) -type surface structure changes into a (1×1) configuration due to dimer breakup. Both transitions are found to be reversible.

To conclude, both Ge surface facets exhibit surface transitions as a function of surface temperature. These transitions are defined by structural rearrangements and partially accompanied by changing electronic properties. Increasing the temperature from above room temperature up to nearly bulk melting temperature leads to an increase in surface conductivity and results in the formation of a high-temperature (1×1) structure for both Ge(111) and Ge(100).

2.3 Hydrogenated surfaces

Hydrogen modifies the structural and electronic properties of surfaces on which it is adsorbed. The presence of hydrogen can lift the surface reconstruction, change the electrical conductivity, passivate the surface reducing its reactivity or remove and introduce

surface states by terminating surface dangling bonds. Moreover, hydrogenation can be used to probe the structure of semiconductor surfaces that commonly possess bonds with varying degrees of bond strain. Depending on the reaction conditions, hydrogen atoms selectively react with these bonds facilitating the study of different bonding types at the surface [128].

To prepare hydrogenated Ge(111) and Ge(100) surfaces, the clean semiconductor surfaces are exposed to atomic hydrogen. Hydrogen atoms are commonly produced using a hot tungsten filament which is placed in front of the surface sample, while the vacuum chamber is filled with pure H₂. The hot filament cracks the molecular hydrogen forming atomic H which then reacts with the clean surfaces [129]. However, exposures are generally reported in terms of molecular hydrogen although it is the flux of atomic hydrogen that is relevant for surface hydrogenation. The atomic hydrogen flux is determined by the cracking efficiency of H₂ and the arrival rate of H on the surface. Therefore, the H atom flux is strongly influenced by the temperature and position of the filament within a particular experimental setup. Thus, the comparison of exposures from different experiments can be complicated [130].

Ge(111)

To prepare a well-ordered hydrogenated Ge(111) surface, a freshly cleaved Ge(111)(2×1) surface is exposed to atomic hydrogen [131]. Compared to the cleaved Ge(111)(2×1) surface, uniform hydrogenation of the ground state Ge(111)*c*(2×8) configuration is more complicated as it can lead to the formation of hydrogenated adatom islands that are distributed randomly on terraces of Ge(111) [128]. However, continuous atomic hydrogen treatment at elevated temperatures was found to smoothen the hydrogen-terminated surface. Specifically, the surface was heated to 500 K and dosed with 3000 L (1 L = 1 Langmuir = 10⁻⁶ Torr s) of H₂. However, the cracking efficiency of H₂ and the arrival rate of H on the surface was unknown [132]. Hydrogenation at lower temperatures cannot remove the adatom islands, whereas at higher temperatures or larger exposures, holes are created at the surface due to the reaction of H atoms with backbonds of the surface rest atom layer [132]. At 600 K, H desorbs from Ge(111). Temperature programmed desorption (TPD) measurements show a single desorption peak [133].

Depending on the sample temperature during hydrogenation, different types of hydrides are formed on the Ge(111) surface. Below 150 K, adsorption of atomic H leads to the formation of monohydride (GeH), dihydride (GeH₂) and trihydride (GeH₃). For temperatures above 400 K, only monohydride is produced. At room temperature, the monohydride formation dominates with minor production of dihydrides [134].

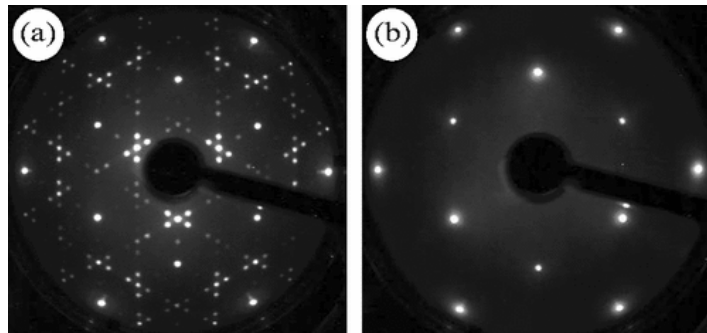


Figure 2.6: LEED patterns of the clean Ge(111) $c(2 \times 8)$ surface (a) and the hydrogenated Ge(111) (1×1) :H surface (b). Both LEED patterns are obtained at a temperature of 100 K with an electron energy of 98 eV. Reprinted figure with permission from Ref. [136]. Copyright 2009 by the American Physical Society.

The surface structure of Ge(111) changes drastically upon hydrogenation as the addition of H atoms removes the reconstruction [74, 132, 135, 136] leading to a bulk-like structure of the surface layer with a perpendicular relaxation of the Ge layer spacings. Compared to bulk values, a contraction of the first interlayer spacing by $0.10 \text{ \AA} \pm 0.05 \text{ \AA}$ was observed. A potential expansion of the second interlayer spacing was proposed [131]. Complete hydrogen-termination removes all superstructure spots visible in the LEED pattern [136]. Fig. 2.6 (a) shows a LEED pattern of the reconstructed Ge(111) $c(2 \times 8)$ surface with characteristic sharp $1/2$ - and $1/8$ -order diffraction spots as well as weak $1/4$ -order spots confirming the well-ordered periodicity of the surface. As shown in Fig. 2.6 (b), the superstructure spots disappear after hydrogen exposure and the diffraction pattern exhibits sharp (1×1) spots, given that a smooth well-ordered hydrogenated surface was formed [136].

The process of hydrogenation of Ge(111) $c(2 \times 8)$ was followed using STM [128]. Initially, hydrogen atoms react with dangling bonds present on the surface. Then they proceed to attack the strained backbonds that bind the adatoms to the rest atom layer, which leads to bond scission and generation of novel dangling bonds. H atoms react with these dangling bonds, which stabilizes the (1×1) rest layer and hydrogenates the adatoms. Ultimately, GeH_4 is formed and the adatoms are thereby removed from the surface. However, hydrogen also facilitates the formation of hydrogenated adatom islands on the surface. These islands exhibit relaxed Ge-Ge bonds and thus also relieves strained backbonds. Overall, the bulk-like rest atom layer gets mainly exposed at the surface through hydrogenation and the $c(2 \times 8)$ reconstruction is removed. In contrast, at very low initial coverages of less than 0.01 monolayer (ML), the $c(2 \times 8)$ reconstruction is retained. Under these conditions, the rest atom site was found to be the preferential

binding site [137, 138]. However, other experiments using different exposure techniques or larger coverages showed no preferential reaction at adatom or rest atom dangling bonds [128].

Modification of the surface structure upon hydrogenation is accompanied by a change of the surface electronic properties. A comparative ARPES study of Ge(111) $c(2 \times 8)$ and Ge(111)(1×1):H found that two occupied surface states at 0.8 eV and 1.4 eV below the Fermi level E_F disappear upon hydrogenation. These two states correspond to rest atom dangling bonds and adatom backbonds, respectively. Furthermore, a new feature at 5 eV below E_F emerges [74]. A more recent ARPES study even observed two new states at -4.93 eV and -4.15 eV with respect to E_F corresponding to newly formed Ge-H bonds and Ge-Ge backbonds between the first and second layer atoms. Another feature lying between these states could not be assigned [136]. EEL spectra, measured as a function of relative hydrogen coverage on the Ge(111) surface, revealed a peak that gradually decreases with increasing hydrogen coverage and completely vanishes at a coverage of $0.4 - 0.5$ ML. This peak was assigned to the transition from the Ge 3d core level to the empty dangling bond surface state originally located at the adatoms [133]. Accordingly, both rest atom and adatom dangling bond states vanish with surface hydrogenation. Moreover, hydrogen adsorption is accompanied by the disappearance of another peak within the EEL spectra that is associated with the transition from backbond states. A new hydrogen related feature is observed at an energy loss of 8.5 eV [133] that could be related to the $\sigma - \sigma^*$ Ge-H transition, with the σ -state lying 5 eV below E_F and σ^* lying 3.5 eV above E_F [129].

Ge(100)

As the Ge(100)(2×1) surface is exposed to atomic hydrogen, Ge(100)(2×1):H monohydride is formed. Surface dimers are preserved and possess one hydrogen atom per Ge dimer atom [139]. Consequently, the (2×1) LEED pattern remains unchanged upon hydrogenation [133, 139, 140]. The asymmetry of the surface dimers, however, gets lifted by hydrogen exposure leading to hydrogenated symmetric dimers on the surface [95, 133]. Several early studies from the 1970s and 1980s concluded that only monohydride is formed on Ge(100) and that it is not possible to produce the dihydride Ge(100)(1×1):2H surface by additional hydrogen adsorption [133, 139, 140]. Later studies also observed a stable dihydride configuration at room temperature [130, 141]. However, prolonged hydrogen exposures are needed to break the Ge surface dimer bonds and form dihydride Ge atoms with two H atoms each. Moreover, it was shown that the hydrogen uptake curve for monohydride formation has a well-defined plateau. This

2 Surface properties of germanium

leads to the conclusion that previous reports observing the monohydride phase only might not have used high enough hydrogen exposures to create the dihydride [130].

To study the effect of hydrogenation on the surface electronic structure of Ge(100), photoelectron spectra were recorded for both the clean (2×1) and the hydrogenated $(2 \times 1):H$ surface reconstructions. Upon hydrogenation, surface states corresponding to surface dangling bonds and backbonds vanish. However, similar to the hydrogenated Ge(111) surface, two new hydrogen-related surface states emerge at 4.5 eV and 5.5 eV below E_F [95]. Moreover, as for Ge(111), EELS measurements recorded as a function of relative hydrogen coverage on the Ge(100) surface revealed a gradually decreasing peak with increasing hydrogen coverage, which is assigned to transitions from the Ge 3d core level to the empty dangling bond surface state. A new hydrogen-related feature was found at an energy loss of 8.2 eV leading to the assumption of an hydrogen-induced empty state at about 3 eV above E_F [133].

In conclusion, hydrogenation impacts the atomic arrangement on the Ge (111) and (100) surfaces. Moreover, the surface electronic structures and consequently possible electronic transitions between surface and/or bulk states get strongly altered by hydrogen atom adsorption.

3 Experimental setup

The H atom scattering experiments presented and discussed in this thesis have been performed using an apparatus particularly designed for this purpose and previously described in Ref. [142]. However, during the course of the experimental work for this thesis, the setup has been modified in two ways. A transfer system for sample storage and fast sample exchange was installed and vacuum-ultraviolet photolysis of hydrogen iodide was used for the first time. In this chapter, I will therefore describe the general setup of the apparatus very briefly and the made modifications in more detail. The scattering apparatus is mainly presented in Section 3.1, while Section 3.2 gives an additional overview of the transfer system and Section 3.3 describes the method of ultraviolet and vacuum-ultraviolet photolysis.

3.1 The H atom scattering apparatus

The H atom scattering apparatus combines techniques known from gas phase experiments with surface science methods. Photolysis of a hydrogen halide supersonic molecular beam is used to generate an H atom beam with narrow energy distribution [50–53]. H atom detection employs the Rydberg atom tagging time-of-flight technique providing high sensitivity and translational energy resolution [54, 55]. Scattering experiments from well-defined crystal surfaces further require ultra-high vacuum (UHV) conditions as well as tools for surface preparation and characterization.

The vacuum system of the apparatus consists of a surface preparation chamber, where the crystal samples are cleaned, prepared and characterized, an adjacent transfer chamber for sample storage and exchange, a source chamber for H atom beam generation, two additional chambers serving as differential pumping stages, and the main scattering chamber, where the H atoms get scattered from surface samples and subsequently detected. The crystal is held by a sample mount at the end of a five-axis manipulator that is mounted on top of the apparatus. By translating the manipulator along the z -direction, the sample mount can be moved from the preparation chamber to the subjacent scattering chamber and vice versa. Furthermore, the manipulator provides

3 Experimental setup

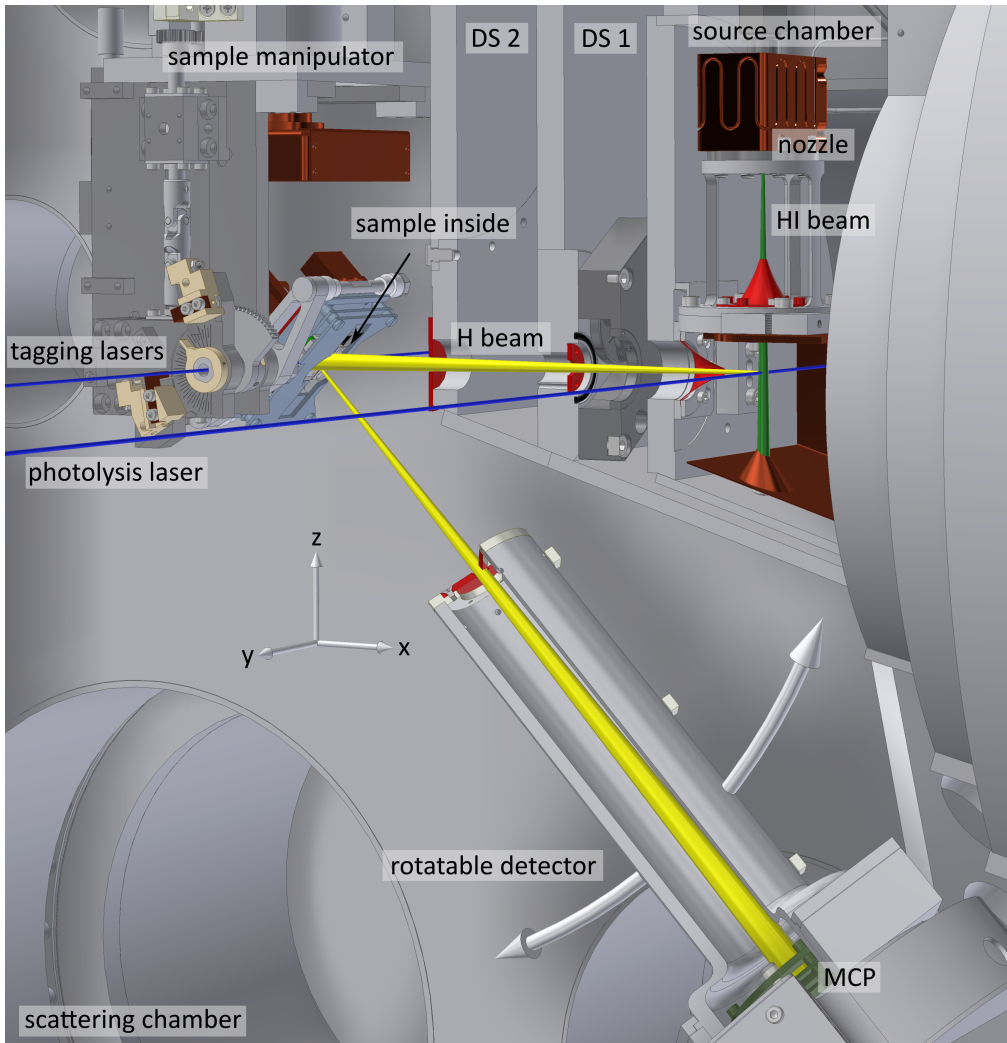


Figure 3.1: Experimental setup. In the source chamber, a hydrogen iodide supersonic molecular beam (green) is generated by a pulsed nozzle, passes a skimmer (red), gets intersected by the photolysis laser beam (blue) and hits a liquid-nitrogen cooled beam catcher plate (copper). Generated H atoms travelling towards the scattering chamber (yellow) pass a second skimmer and two differential pumping stages (DS 1 and DS 2) before they enter the scattering chamber and collide with the sample surface. The sample is mounted on a five-axis manipulator that allows translation in x -, y -, and z -direction as well as rotation about the y - and z -direction (see coordinate system for the definition of the axes). The surface can be heated using either electron bombardment heating or resistive heating and cooled using a flow cryostat with liquid nitrogen or liquid helium. The scattered H atoms get excited to a high Rydberg state using two tagging laser pulses (blue), pass an aperture that defines the angular resolution of the detector (red), get field ionized and subsequently detected by a MCP detector (olive). The detector can be rotated in the plane perpendicular to the tagging lasers allowing to record angular-resolved measurements. The preparation chamber and the transfer system are situated on top of the scattering chamber and not shown.

3.1 The H atom scattering apparatus

translation in the x - and y -directions as well as rotation about the y - and z -axes. This allows precise alignment of the sample previous to the scattering experiment and positioning in front of the surface preparation and characterization tools, which are mounted on the preparation chamber. For surface cleaning, an argon ion sputter gun is installed. The preparation chamber is further equipped with an Auger electron spectrometer and a low-energy electron diffractometer for surface sample characterization as well as with a hydrogen atom cannon and an ultrahigh vacuum leak valve for surface dosing. The sample is heated using either electron bombardment heating or resistive heating. For cooling, a liquid nitrogen or liquid helium flow cryostat can be used. Ge surface samples were purchased from *Crystal*. According to the manufacturer, undoped Ge single crystals are grown using the Czochralski method [143] and have a purity of 99.999%. The crystals are cut along a certain lattice plane to produce a surface sample with the desired low-index surface facet and polished on one side.

Another chamber, which is part of the newly installed transfer system, is mounted next to the preparation chamber. Both chambers can be separated from each other by an all-metal gate valve. The new chamber is used as a load lock and allows – together with a magnetically coupled transfer arm – a fast and easy sample exchange. The complete transfer system is described in more detail in Section 3.2.

The remaining parts of the vacuum system are shown in Fig. 3.1. The source chamber contains a pulsed nozzle to produce an internally cooled supersonic molecular beam of HI. The HI molecules pass a skimmer before getting photodissociated by an (vacuum-) ultraviolet laser pulse to generate hydrogen and iodine atoms. A liquid nitrogen cooled beam catcher is installed below the photolysis region to ensure that no HI molecules enter the scattering chamber and contaminate the surface sample during the time frame of the experiment. H atoms travelling towards the scattering chamber pass a second skimmer and both differential pumping stages before they enter the UHV scattering chamber, where they collide with the sample surface. After scattering, the H atoms are detected using the Rydberg atom tagging time-of-flight (RAT-TOF) technique. The H atoms are excited to a high Rydberg state by a two-step process. First, the $1s-2p$ transition is excited at 121.57 nm. A second photon with a wavelength of about 365 nm subsequently excites the H atom to Rydberg states with high principal quantum numbers ($n = 30 - 70$). After tagging, the neutral Rydberg atoms fly a total distance of about 250 mm. After 90 mm, they pass an aperture defining the angular resolution and shortly before reaching the multichannel plate (MCP) detector, they are field-ionized by a moderate electric field. The generated ions are accelerated towards the MCP detector, which is mounted 4 mm away from the point of ionization. A multichannel scaler records their time-of-flight. The detector is rotatable over an angular range of $0^\circ - 150^\circ$

3 Experimental setup

with respect to the atomic beam in the plane perpendicular to the tagging laser beams, allowing to perform scattering-angle resolved measurements.

The overall energy resolution of the instrument is influenced by both incident H atom beam properties and the resolution of the detection system. The incident H atom beam has a certain translational energy width that is determined by the bandwidth and focal size of the photolysis laser as well as by the rotational temperature of the hydrogen iodide molecular beam. The relative energy resolution of the detector is determined by three factors: the uncertainty in flight distance, which is given by the size of the tagging point, the pulse duration of the tagging laser, which is 10 ns, and the angular acceptance, which is 3° and determined by the aperture in front of the detector. The overall resolution therefore depends on the settings of the respective experiment, such as the choice of neat or seeded molecular beams as well as the properties of photolysis and tagging lasers. A maximum energy resolution of $E/\Delta E \approx 1000$ can be achieved. However, a high energy resolution is usually attended by low signal flux, making high resolution experiments complicated and longsome. In contrast, for experimental settings optimized to maximize signal, an energy resolution of $E/\Delta E \approx 100$ is typically achieved.

3.2 The transfer system

During the course of the experimental work for this thesis, a transfer system for sample storage and fast sample exchange was installed to the H atom scattering apparatus. The tremendous advantage of the new transfer system is given by the ability to exchange samples while preserving UHV conditions in the preparation and scattering chamber. Thereby, samples can be switched in between experiments within a few hours rather than several days since venting and subsequent bake-out of the whole apparatus are no longer inevitable for sample exchange.

The transfer system consists of a cubic stainless steel chamber that was machined at the institute's fine mechanics workshop. The chamber is equipped with a sample parking stage, a magnetically coupled transfer arm (*VAb* MDS 40-800), an O-ring sealed rectangular chamber door as well as a *Pfeiffer Vacuum* HiPace[®] 300M turbomolecular pump, an *Edwards* Active Ion Gauge and a DN 100 CF flange viewport.

The transfer chamber is mounted next to the preparation chamber. Both chambers can be separated from each other by an all-metal gate valve that is able to seal UHV from atmospheric pressure. The chamber is used as a load lock and contains a three-level rack at the inside of the chamber door as well as a magnetically coupled transfer arm. Apart

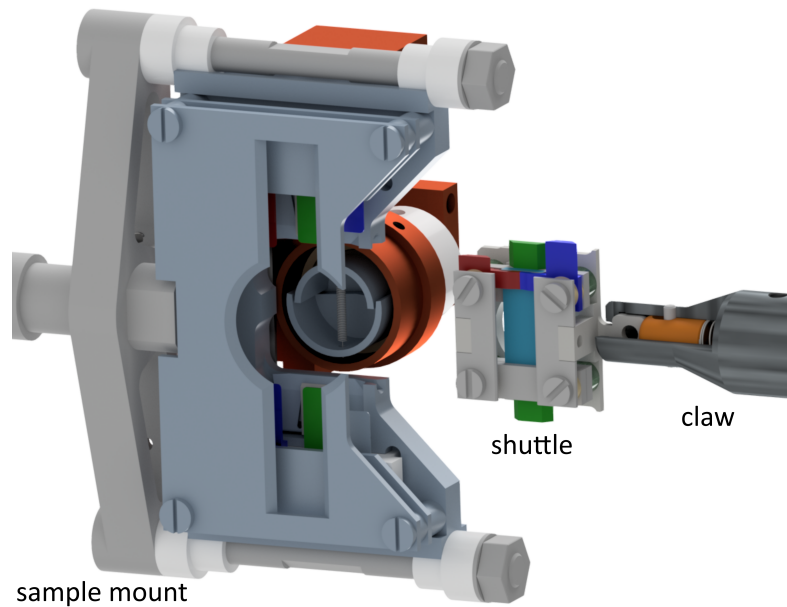


Figure 3.2: Transfer system sample mount (left) and shuttle (middle) hold by a spring-loaded claw (right) at the end of a magnetically coupled transfer arm. The crystal sample (turquoise) is mounted on a shuttle setup. The shuttle is based upon a flag style sample ground plate and contains electrical contacts for grounding or resistive heating (green) as well as thermocouple contacts (red and blue). A claw (dark gray, partially shown on the right side) at the end of the transfer arm (not shown) can hold the shuttle as it slides over the ground plate's handle, which is locked in place by a spring-loaded piston (ocher). The ground plate of the shuttle accurately fits into two slits at the reception on the sample mount. Once the shuttle is properly attached to the sample mount, measurement of the sample temperature via thermocouple junction is possible and electric contacts for grounding or resistive heating are established. Alternatively, a filament mounted behind the reception can be used for electron bombardment heating.

from the sample mounted on the main sample holder, the rack can store two additional crystal samples. The transfer arm can be moved along the x -direction from the transfer chamber to the preparation chamber and vice versa if the gate valve is open. This allows a fast sample exchange under vacuum conditions. The transfer chamber can be vented separately from the remaining vacuum system to insert new samples. After pumping down, a new sample can directly be transferred into the UHV preparation chamber profoundly improving the process of sample exchange that was previously associated with venting the whole apparatus and subsequent bake-out for several days.

The transfer system sample mount is positioned at the end of the five-axis manipulator, as shown in Fig. 3.1. Fig. 3.2 shows the sample mount and shuttle carrying the crystal

3 Experimental setup

sample in more detail. The design of the shuttle is based on a commercially available flag style ground plate possessing a handle on one side. Two cover plates that are screw-fastened to the ground plate hold the crystal as well as several insulating spacers and electric contacts in place. The rectangular-shaped crystal sample (shown in turquoise in Fig. 3.2) has dimensions of $15\text{ mm} \times 5\text{ mm} \times 0.5\text{ mm}$. Contacts for grounding or resistive heating (green) are centrally arranged on both sides of the shuttle, thermocouple contacts (red and blue) for temperature measurements are additionally mounted on one side of the shuttle. The respective counterpart contacts are precisely positioned at the reception of the sample mount. The shuttle can be manipulated along the x -direction from the transfer chamber to the preparation chamber by a magnetically coupled transfer arm. A claw at the end of the transfer arm, which is partially shown in Fig. 3.2, has a slit at the top end that accurately slides over the ground plate's handle (see cutout). After rotating the transfer arm about 90° either way, the handle locks in place and is fixed by a spring-loaded piston (ocher). Back rotation releases the shuttle as the ground plate's handle is again in the right position to slide out of the claw's slit. Using the magnetically coupled transfer arm, the shuttle is pushed into two slits at the reception on the sample mount that precisely fit to the dimensions of the flag style ground plate. Once the shuttle is properly attached to the sample mount, measurement of the sample temperature via thermocouple junction is possible and electric contacts for grounding or resistive heating are established. Alternatively, electron bombardment can be used for heating. As electron source, a thoriated tungsten filament (1% ThO_2) is mounted between two electrically isolated but spatially interlocked molybdenum half cylinders on the back side of the reception. High voltage ($U \approx 0.4\text{ kV}$) is applied to the half cylinders with a small electric potential difference between both to generate a current ($I \approx 3\text{ A}$) through the filament. Emitted electrons get repelled from the half cylinders and are focused onto the backside of the grounded crystal sample.

Another shuttle design for circular-shaped crystals and exclusively electron bombardment heating is available but has not been used for the experiments discussed in this thesis. Currently, there is also an additional sample mount that can replace the one optimized for the transfer system. This sample mount cannot be used together with the transfer system, however, it additionally allows azimuthal rotation about the crystal normal. A third version, optimized for cold temperature experiments, is planned.

3.3 Ultraviolet and vacuum-ultraviolet photolysis

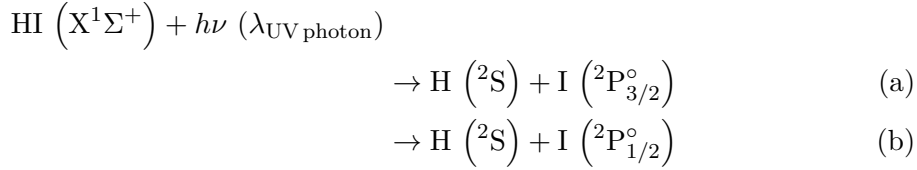
Atomic hydrogen beams with tunable translational energy and narrow velocity spread are essential to perform well-defined H atom-surface scattering experiments. Within the

3.3 Ultraviolet and vacuum-ultraviolet photolysis

used experimental setup, H atom beams are generated by either 1-photon ultraviolet (UV) or 1-photon vacuum-ultraviolet (VUV) photolysis of HI molecules. Therefore, two photolysis laser systems are available; an excimer laser operated with ArF or KrF as well as a Nd:YAG pumped dye laser system.

This section starts with a discussion of the principles of UV and VUV photodissociation, overviews the properties of the experimentally generated H atom beams and describes the techniques applied for VUV photolysis of HI in detail.

The first UV absorption band of HI at $33000 - 53000 \text{ cm}^{-1}$ is broad and featureless and peaks at about 45000 cm^{-1} ($\lambda_{\text{UV photon}} \approx 220 \text{ nm}$), as shown in Fig. 3.3 [144, 145]. The continuous absorption band involves four transitions from the $X^1\Sigma^+$ ground state to the $A^1\Pi_1$, $a^3\Pi_1$, $a^3\Pi_{0+}$, and $t^3\Sigma^+$ repulsive states. Transitions to the $A^1\Pi_1$, $a^3\Pi_1$, and $a^3\Pi_{0+}$ states dominate and arise from $\pi \rightarrow \sigma^*$ excitations. The fourth repulsive state, $t^3\Sigma^+$, arising from $\sigma \rightarrow \sigma^*$ excitation, has a minor contribution. The repulsive states promptly dissociate to form ground state H atoms as well as iodine atoms either in the electronic ground state (a) or in the first excited state (b) [50, 146, 147].



HI is excited to the $A^1\Pi_1$ and $a^3\Pi_1$ repulsive states via a perpendicular transition ($\Delta\Omega = \pm 1$, for a Hund's case (c) coupled molecule such as HI) and subsequently dissociates to form ground state H and I atoms, following channel (a). In contrast, excitation to the $a^3\Pi_{0+}$ state via parallel transition ($\Delta\Omega = 0$) corresponds to dissociation channel (b) forming ground state H atoms and spin-orbit excited I atoms. A minor contribution of a perpendicular transition to channel (b) is attributed to the fourth excited state, $t^3\Sigma^+$. The branching ratio determining the fraction to which iodine is formed in the ground or first excited state during photolysis is a fundamental characteristic of the photofragmentation reaction and depends on the particular excitation wavelength [50]. To employ UV photodissociation of HI within our experiment, an excimer laser operated with ArF or KrF is used. It emits unpolarized laser light at wavelengths of 193.3 nm or 248.35 nm, respectively. Using a photolysis wavelength of 248.35 nm, both reaction channels (a) and (b) are accessed with nearly equal propensity. However, using 193.3 nm, the reaction follows nearly exclusively channel (a) [50, 148].

Maximum photon absorption probability is observed when the transition dipole mo-

3 Experimental setup

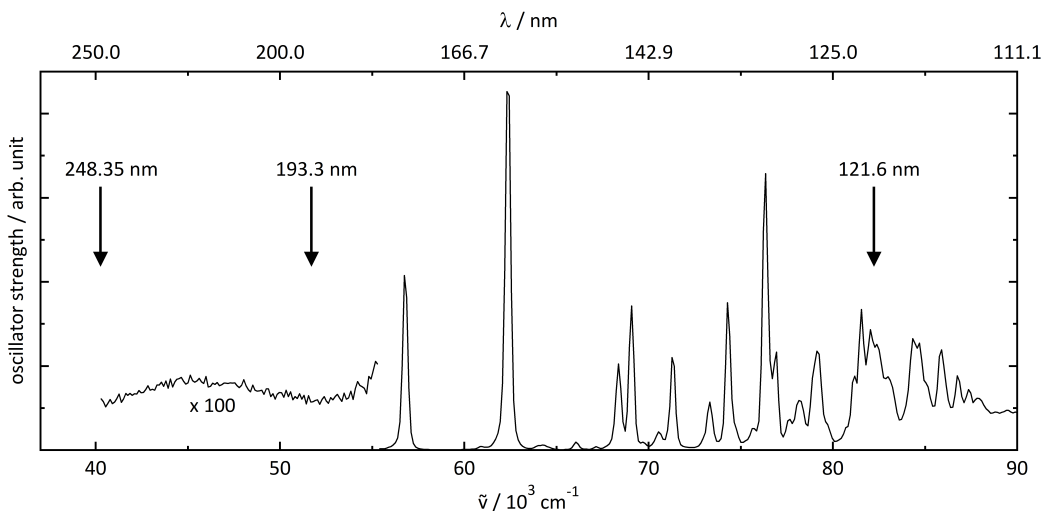


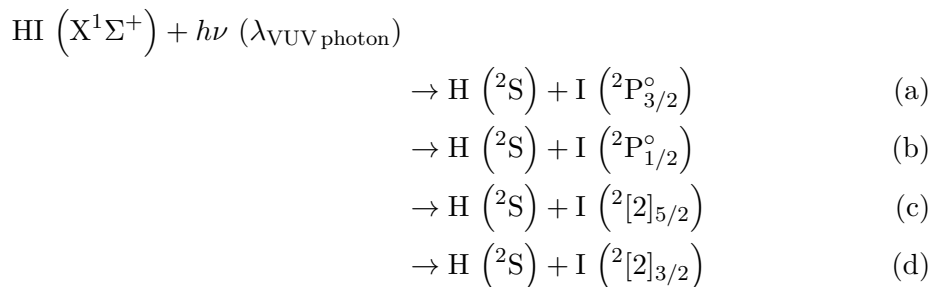
Figure 3.3: Photoabsorption spectrum for the discrete and low energy continuum regions of the valence shell of HI. Vertical arrows mark the photolysis laser wavelengths employed during the experimental work of this thesis. 248.35 nm and 193.3 nm UV radiation is generated using a KrF or ArF excimer laser, respectively. VUV photons with wavelengths of about 121.6 nm are formed by degenerate four-wave mixing. The figure is adapted from Fig. 3 in Ref. [145].

ment $\vec{\mu}$ is aligned parallel to the electric field vector of linearly polarized light. The photofragments of a dissociating diatomic molecule separate along the internuclear axis. In a parallel transition with a transition dipole moment parallel to the molecular axis, molecules that are aligned parallel to the electric field vector of light are predominantly excited and the photodissociation fragments separate along this direction. In contrast, for a perpendicular transition both fragments fly apart from each other perpendicular to the transition dipole moment and electric field vector. In both cases a strong anisotropic angular distribution of the photofragments is observed. However, the excimer radiation used for UV photolysis within our experimental setup is unpolarized. Consequently, isotropic H atom angular distributions are obtained since the precursor molecules in the supersonically expanded beam are neither oriented nor aligned. Only a small fraction of H atoms travelling along the x -direction reach the surface sample after passing a skimmer and several apertures. Increasing the laser power leads to a rising number of H atoms incident on the surface as the fraction of dissociating precursor molecules increases. However, increasing the laser power is accompanied by a pressure rise in the source chamber and is therefore only possible to a limited extent. Alternatively, a polarizer can be installed that only transmit light of a certain polarization, which then

3.3 Ultraviolet and vacuum-ultraviolet photolysis

enters the source chamber. This way, HI molecules, which are properly aligned with respect to the plane of polarization, are selectively dissociated leading to a strong H atom signal while the overall pressure rise is kept as small as possible. Purely parallel or perpendicular transitions can be selected by rotating the plane of laser polarization with respect to the x -axis. Currently, a thin film polarizer suitable for polarization selection of the excimer laser radiation is available and will be installed soon.

The continuum intensity of the first UV absorption band decreases to a minimum around 53300 cm^{-1} and then grows monotonically into a second UV continuum that merges with a discrete spectrum of transitions corresponding to bound molecular states at around 56500 cm^{-1} . A region with discrete transitions to Rydberg states extends up to about 90000 cm^{-1} , as shown in Fig. 3.3 [145]. Using VUV photons within this energy range, indirect photodissociation via resonantly excited rovibrational levels of pre-dissociating Rydberg states is possible [52]. In contrast to the prompt dissociation from repulsive states excited within the first UV absorption band, predissociation processes involve for example coupling of the initially excited state to different repulsive states or gateway states that are themselves coupled to repulsive states [53]. Complex photoabsorption spectra reflect these VUV photodissociation dynamics of HI. Using VUV radiation with energies in the vicinity of Lyman- α radiation ($\tilde{\nu}_{\text{VUV}} \approx 82259\text{ cm}^{-1}$), four dissociation channels forming ground state hydrogen atoms are accessible:



Channel (a) leads to ground state H and I atoms, whereas ground state H atoms and electronically excited I atoms are formed within channels (b) to (d). Assignments of the electronic states of the I atom cofragments rely on the known energy levels of iodine.

The translational energy of the H atoms generated by UV or VUV photolysis, $E_{\text{kin}}(\text{H})$, is determined by the conservation of energy and momentum during the dissociation reaction. Conservation of energy requires the initially available energy to be distributed among the translational and internal degrees of freedom of the atomic product frag-

3 Experimental setup

ments. $E_{\text{kin}}(\text{H})$ depends on the photolysis photon energy, $h\nu$, the initial kinetic energy of the HI molecules, $E_{\text{kin}}(\text{HI})$, the initial internal energy of the HI molecules, $E_{\text{int}}(\text{HI})$, determined by the rotational and vibrational temperatures, the bond dissociation energy of HI, $D_0(\text{H}-\text{I})$, the final kinetic energy of the iodine fragment, $E_{\text{kin}}(\text{I})$, as well as the final internal energies of the H and I fragments, $E_{\text{int}}(\text{H})$ and $E_{\text{int}}(\text{I})$:

$$h\nu + E_{\text{kin}}(\text{HI}) + E_{\text{int}}(\text{HI}) = E_{\text{kin}}(\text{H}) + D_0(\text{H}-\text{I}) + E_{\text{kin}}(\text{I}) + E_{\text{int}}(\text{H}) + E_{\text{int}}(\text{I}) \quad (3.1)$$

The HI molecular beam is generated by a supersonic beam expansion. Collisions during the supersonic expansion cause strong translational, vibrational, and rotational cooling, so that the initial internal energy of the HI molecules can be approximated to be zero. The H atom fragments are generated in their electronic ground state, since the energy provided by UV photons is smaller than the energy required to excite an H atom from the ground state to any excited state. For VUV photolysis, the accessible dissociation channels also produce ground state H atoms. In summary, the translational energy of the generated H atoms is thus given by:

$$E_{\text{kin}}(\text{H}) = h\nu + E_{\text{kin}}(\text{HI}) - D_0(\text{H}-\text{I}) - E_{\text{kin}}(\text{I}) - E_{\text{int}}(\text{I}) \quad (3.2)$$

Using 248.35 nm and 193.3 nm excimer radiation, H atom beams with translational energies of about 1 – 3 eV and energy widths of $\Delta E \approx 10 - 20$ meV are generated. Changing the precursor molecule from HI to DI allows isotope experiments with incidence translational energies in the same energy range. To extend the range of available incidence energies, VUV photodissociation of HI at wavelengths of about 121.4 nm has additionally been employed. Thereby, H atom beams with translational energies of about 6 and 7 eV and energy widths of $\Delta E \approx 20$ meV as well as H atom beams with translational energies of about 0.2 and 0.4 eV and energy widths of $\Delta E \approx 1 - 2$ meV can be produced. Fig. 3.4 shows the translational energy distributions of H atom beams produced by both UV and VUV photolysis. Exact H atom beam energies, energy widths and used photolysis wavelengths are given in the associated caption.

VUV photons are produced by non-linear ($2\tilde{\nu}_{\text{UV}} - \tilde{\nu}_{\text{IR}}$) degenerate four-wave mixing (FWM). The experimental setup used for FWM prior to photolysis corresponds to the one employed for the generation of Lyman- α radiation used within the Rydberg atom tagging scheme of H atoms after scattering [142]. A UV laser pulse ($\tilde{\nu}_{\text{UV}} = 47046 \text{ cm}^{-1}$) and a tunable infrared (IR) laser pulse ($\tilde{\nu}_{\text{IR}} = 11600 - 12200 \text{ cm}^{-1}$) are colinearly focused into a krypton/argon gas cell to generate VUV radiation in the energy range of $\tilde{\nu}_{\text{VUV}} = 81900 - 82450 \text{ cm}^{-1}$. The gas cell consists of a 200 mm long stainless steel cylinder with an inner diameter of 10 mm. The cylinder is sealed to atmosphere by a

3.3 Ultraviolet and vacuum-ultraviolet photolysis

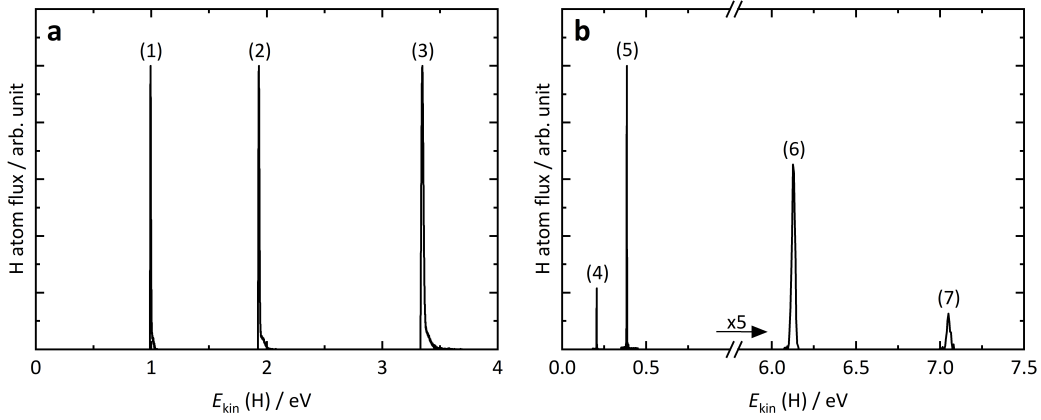


Figure 3.4: Translational energy distributions of H atom beams produced by two different photolysis laser systems. Panel a shows translational energy distributions of H atoms generated by UV photodissociation of HI with laser wavelengths of 248.35 nm, (1) and (2), or 193.3 nm, (3), produced by a KrF or ArF excimer laser, respectively. (1): $E_{\text{kin}}(\text{H}) = 0.99$ eV and $\Delta E = 7$ meV, (2): $E_{\text{kin}}(\text{H}) = 1.92$ eV and $\Delta E = 11$ meV, and (3): $E_{\text{kin}}(\text{H}) = 3.33$ eV and $\Delta E = 22$ meV. All three distributions are peak-normalized. Panel b shows the kinetic energy distributions of H atom beams formed by VUV photolysis of HI with laser wavelengths of 121.35 nm, (4) and (5), 121.41 nm, (6), and 121.46 nm, (7). (4): $E_{\text{kin}}(\text{H}) = 0.21$ eV and $\Delta E = 1$ meV (10%), (5): $E_{\text{kin}}(\text{H}) = 0.38$ eV and $\Delta E = 2$ meV (80%), (6): $E_{\text{kin}}(\text{H}) = 6.17$ eV and $\Delta E = 23$ meV (100%), and (7): $E_{\text{kin}}(\text{H}) = 7.10$ eV and $\Delta E = 20$ meV (20%). The relative intensities with respect to the signal obtained for H atoms with $E_{\text{kin}}(\text{H}) = 6.17$ eV are given as percentages in parentheses. All four distributions are normalized to the area and multiplied with a factor corresponding to their relative intensity.

fused silica window and to UHV by a differentially pumped LiF lens that also collimates the generated VUV radiation. In the employed sum-difference frequency mixing scheme, a Kr atom is resonantly excited into the $4p^5 5p$ state by absorbing two UV photons of frequency $\tilde{\nu}_{\text{UV}}$. Simultaneously, one IR photon with the frequency $\tilde{\nu}_{\text{IR}}$ induces relaxation to the $4p^6$ ground state under emission of a VUV photon. Phase matching ($\vec{k}_{\text{VUV}} = 2\vec{k}_{\text{UV}} - \vec{k}_{\text{IR}}$) is achieved by adjusting the composition of the Kr/Ar mixture as well as the total pressure in the gas cell [149]. Within the used experimental setup, a Kr/Ar mixture with a partial pressure ratio of 1 : 3 and a total pressure of 100 – 150 mbar were found to work best. The laser system used for FWM comprises a single Q-switched nanosecond Nd:YAG laser that pumps two dye lasers operating at 30 Hz. UV photons are produced by stepwise tripling the output of a dye laser (DCM dissolved in ethanol) in two non-linear crystals whereas for the IR laser radiation the fundamental of a second dye laser (LDS 821 and LDS 867 dissolved in ethanol) is used.

3 Experimental setup

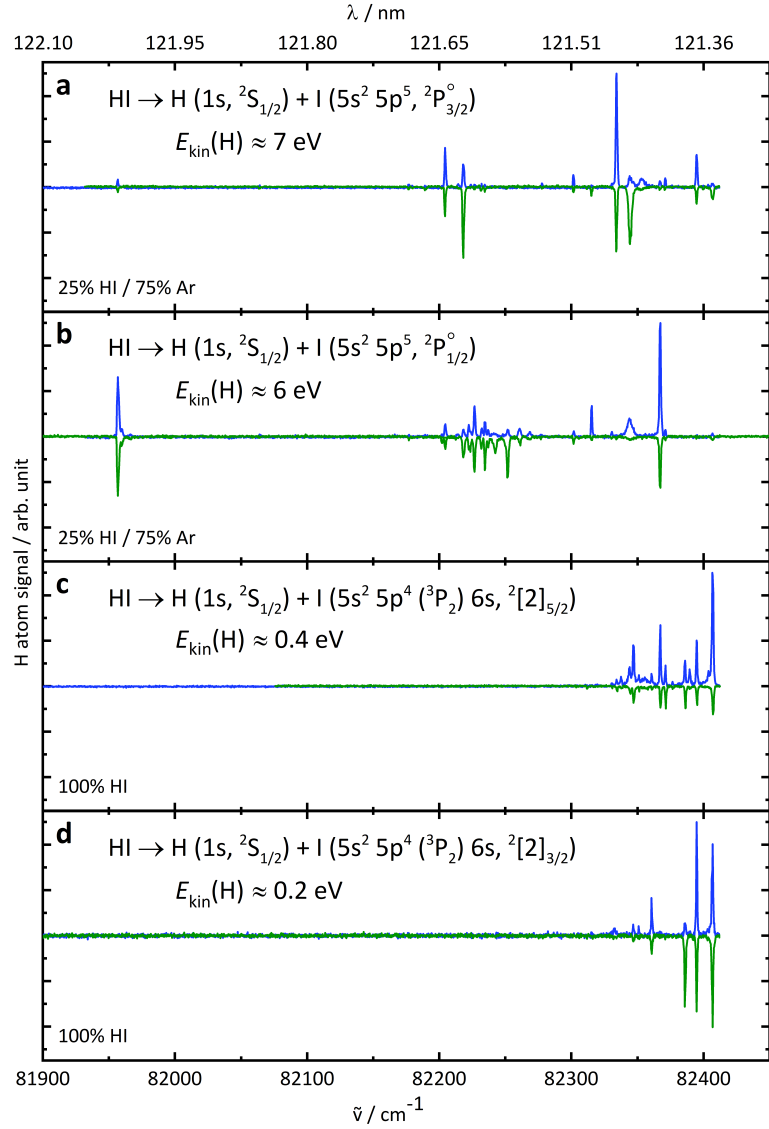


Figure 3.5: H atom signal generated by VUV photolysis of HI as a function of the photolysis photon energy. Several resonant transitions to pre-dissociating rovibrational levels of Rydberg states are found within the energy range of $\tilde{\nu} = 81900 - 82450 \text{ cm}^{-1}$. Four dissociation channels are accessible within the used energy range leading to different electronic states of the iodine fragment, as shown in panel a to d. H atoms are detected using the RAT-TOF technique. The time delay between the photolysis and tagging laser pulses can be adjusted to discriminate between H atoms with different velocities and thereby differentiate between the four dissociation channels. The polarization of the photolysis laser beam is tuned using a half-waveplate. Signal obtained with a linearly polarized laser beam parallel to the direction of the H atom beam (blue solid line) is compared to the signal obtained with perpendicular laser beam polarization (green solid line, multiplied with a factor of -1). For each dissociation channel, the signal is normalized to the peak maximum obtained at parallel laser beam polarization.

3.3 Ultraviolet and vacuum-ultraviolet photolysis

Both UV and IR laser beams are linearly polarized. Typical energies for the laser pulses are 1 mJ for the UV pulse and 8 mJ for the IR pulse.

Fig. 3.5 shows H atom signal generated according to the four dissociation channels (a) to (d) accessible using VUV photolysis and measured as a function of the photolysis photon energy. The photon energy is scanned in the range of $\tilde{\nu}_{\text{VUV}} = 81900 - 82450 \text{ cm}^{-1}$ with a step size of $\Delta\tilde{\nu}_{\text{VUV}} = 0.3 \text{ cm}^{-1}$. Several resonances are observed within each dissociation channel. The wavelength and polarization of the VUV radiation is changed by tuning the wavelength and polarization of the precursor IR radiation ($\tilde{\nu}_{\text{IR}}$) prior to FWM. A linearly polarized laser beam was used with the electric field vector aligned either parallel or perpendicular to the direction of the H atom beam (x -direction). The time delay between the photolysis and tagging laser pulses was adjusted to discriminate between H atoms with different translational energies as generated via dissociation channels (a) to (d). H atoms with a translational energy of about 7 eV are formed in association with ground state I ($^2\text{P}_{3/2}^{\circ}$) atoms (Fig. 3.5 a), whereas approximately 6 eV H atoms are generated together with first excited state I ($^2\text{P}_{1/2}^{\circ}$) atoms (Fig. 3.5 b). Dissociation processes forming iodine atoms in the two higher electronically excited states ($^2[2]_{5/2}$ and $^2[2]_{3/2}$) generate H atoms with translational energies of about 0.4 eV (Fig. 3.5 c) and 0.2 eV (Fig. 3.5 d), respectively. Following equation 3.2, the exact H atom translational energy depends on the applied photolysis photon energy and therefore changes slightly within the investigated energy range. Within the scattering ex-

Table 3.1: Utilized photon energies for VUV photolysis. For each dissociation channel, the routinely used VUV photon energy is given. VUV photons are produced by degenerate FWM using a fixed UV laser pulse ($\tilde{\nu}_{\text{UV}} = 47046 \text{ cm}^{-1}$) and a tunable IR laser pulse $\tilde{\nu}_{\text{IR}}$. For each dissociation channel, corresponding translational energies and energy widths of the generated H atom beams are given as well as relative intensities of the respective H atom signal with respect to the strongest signal obtained for H atoms with $E_{\text{kin}}(\text{H}) = 6.17 \text{ eV}$, generated via channel (b).

dissociation channel	relative intensity	$E_{\text{kin}}(\text{H})$ /eV	$\Delta E_{\text{kin}}(\text{H})$ /meV	λ_{VUV} /nm	$\tilde{\nu}_{\text{VUV}}$ / cm^{-1}	$\tilde{\nu}_{\text{IR}}$ / cm^{-1}
(a)	0.2	7.10	20	121.46	82334	11758
(b)	1.0	6.17	23	121.41	82367	11725
(c)	0.8	0.38	2	121.35	82407	11685
(d)	0.1	0.21	1	121.35	82407	11685

3 Experimental setup

periments, the resonant transition leading to the highest H atom beam intensity within each dissociation channel was generally utilized. For all four channels, this was found to be a parallel transition with the VUV laser beam polarization parallel aligned to the direction of the H atom beam. The exact VUV photon energies used in the experiments are given in Table 3.1. The corresponding translational energy distributions of the H atom beams are given in Fig. 3.4 b.

4 Hydrogen atom scattering from germanium surfaces

4.1 Evidence of adiabatic and non-adiabatic energy transfer

Section 4.1 is comprised of Ref. [150], an open access article titled "*Hydrogen atom collisions with a semiconductor efficiently promote electrons to the conduction band*", published in *Nature Chemistry*. The article (DOI 10.1038/s41557-022-01085-x) is licensed under a Creative Commons Attribution 4.0 International License (CC BY 4.0) (<https://creativecommons.org/licenses/by/4.0/>).

Material from: Kerstin Krüger, Yingqi Wang, Sophia Tödter, Felix Debbeler, Anna Matveenko, Nils Hertl, Xueyao Zhou, Bin Jiang, Hua Guo, Alec M. Wodtke & Oliver Bünermann, Hydrogen atom collisions with a semiconductor efficiently promote electrons to the conduction band, *Nature Chemistry*, published 2022, Springer Nature.

In this article, translational energy-loss distributions of H atoms scattered from Ge(111) $c(2 \times 8)$ are presented, obtained from both experimental and theoretical investigations. Results of electronically adiabatic molecular dynamics simulations are provided by the group of Prof. Dr. Hua Guo, University of New Mexico, NM, USA. Through a comparison of experimental and theoretical results, a fundamental interpretation of the scattering dynamics is derived. Experiments show bimodal energy-loss distributions reflecting two scattering channels, while adiabatic MD simulations reproduce only one. The second channel transfers much more energy and is absent in the simulations. Furthermore, it exhibits an energy-loss onset equal to the Ge surface band gap. This leads to the conclusion that two types of interactions are possible for H atoms scattering from Ge(111) $c(2 \times 8)$. They may either experience electronically adiabatic, mechanical interactions well described within the BOA or strongly non-adiabatic interactions capable of promoting electrons to energies above the band gap.

The article is Ref. [150] in this thesis:

- [150] K. Krüger, Y. Wang, S. Tödter, F. Debbeler, A. Matveenko, N. Hertl, X. Zhou, B. Jiang, H. Guo, A. M. Wodtke, O. Bünermann, Hydrogen atom collisions with a semiconductor efficiently promote electrons to the conduction band, *Nat. Chem.* **2023**, *15*, 326-331, <https://doi.org/10.1038/s41557-022-01085-x>.

Author contributions:

K.K. performed the experiments. Y.W., X.Z., B.J. and H.G. constructed the NN-PES and Y.W. performed the MD simulations. S.T., F.D. and A.M. assisted in part of the experiments during their master and bachelor theses. Y.W. and K.K. analyzed the data. O.B., A.M.W. and K.K. wrote the manuscript with feedback from Y.W., N.H., B.J. and H.G.

With Ref. [150] associated articles:

1. J. L. Miller, A solid-state failure of the Born-Oppenheimer approximation, *Phys. Today* **2023**, *76*, 16-17, <https://doi.org/10.1063/PT.3.5172>.
2. H. Nienhaus, Mysterious energy losses, *Nat. Chem.* **2023**, *15*, 301-302, <https://doi.org/10.1038/s41557-023-01145-w>.



Hydrogen atom collisions with a semiconductor efficiently promote electrons to the conduction band

Received: 14 April 2022

Accepted: 6 October 2022

Published online: 21 November 2022

Check for updates

Kerstin Krüger¹, Yingqi Wang², Sophia Tödter¹, Felix Debbeler¹, Anna Matveenko¹, Nils Hertl^{3,6}, Xueyao Zhou⁴, Bin Jiang⁴, Hua Guo², Alec M. Wodtke^{1,3,5} & Oliver Bünermann^{1,3,5}✉

The Born–Oppenheimer approximation is the keystone of modern computational chemistry and there is wide interest in understanding under what conditions it remains valid. Hydrogen atom scattering from insulator, semi-metal and metal surfaces has helped provide such information. The approximation is adequate for insulators and for metals it fails, but not severely. Here we present hydrogen atom scattering from a semiconductor surface: Ge(111)c(2 × 8). Experiments show bimodal energy-loss distributions revealing two channels. Molecular dynamics trajectories within the Born–Oppenheimer approximation reproduce one channel quantitatively. The second channel transfers much more energy and is absent in simulations. It grows with hydrogen atom incidence energy and exhibits an energy-loss onset equal to the Ge surface bandgap. This leads us to conclude that hydrogen atom collisions at the surface of a semiconductor are capable of promoting electrons from the valence to the conduction band with high efficiency. Our current understanding fails to explain these observations.

Atoms and molecules colliding at solid surfaces create time-varying electric fields that, due to their finite masses and associated low speeds, represent frequencies typically $\leq 10^{13}$ Hz, whereas much lighter electrons in solids oscillate at frequencies one to two orders of magnitude higher than this. This separation of timescales is used to justify the Born–Oppenheimer approximation (BOA)¹, the bedrock of computational surface chemistry², where electronic quantum states rapidly adjust to the motion of nuclei. Inelastic H atom surface scattering experiments have provided excellent benchmarks against which theoretical methods can and have been tested and proved³. Using this approach, the BOA has been shown to be justified for H atom scattering from Xe, where molecular dynamics (MD) simulations using a full-dimensional

potential energy surface (PES) quantitatively reproduced energy losses measured in high-resolution scattering experiments⁴. The validity of the BOA in that case is not surprising since the lowest energy electronic excitations in Xe exceeded the energies of that work. Similar energy-loss measurements from experiments scattering H and D from the semi-metal graphene, where low-energy electron–hole pair (EHP) excitations are possible, also showed no signs of BOA failure^{5–7}. Despite these successes, there are reasons to question the validity of the BOA (refs. ^{8,9}). For example, energetic H atoms colliding at metal surfaces always excite EHPs (refs. ^{10,11}). However, theoretical methods could successfully treat this with a weak-coupling ‘electronic-friction’ approximation^{12,13}, suggesting BOA failure is not severe and can be accounted for in a perturbative fashion.

¹Institute of Physical Chemistry, Georg-August University, Göttingen, Germany. ²Department of Chemistry and Chemical Biology, University of New Mexico, NM, USA. ³Department of Dynamics at Surfaces, Max-Planck-Institute for Multidisciplinary Sciences, Göttingen, Germany. ⁴Hefei National Research Center for Physical Science at the Microscale, Department of Chemical Physics, University of Science and Technology of China, Hefei, China. ⁵International Center of Advanced Studies of Energy Conversion, Georg-August University, Göttingen, Germany. ⁶Present address: Department of Chemistry, University of Warwick, Coventry, United Kingdom. ✉e-mail: oliver.buenermann@chemie.uni-goettingen.de

Experiments with semiconductors present an opportunity to make predictions from our current understanding about a fundamentally different class of solids. This is true if semiconductors behave in some hybrid fashion, reflecting some intermediate between insulators and metals. However, let us consider semiconductors from the point of view of another kind of time-varying electric field. We know visible light with electric fields oscillating at $\sim 10^{14-15}$ Hz efficiently excites electrons from the valence band (VB) to the conduction band (CB), forming the basis for a large fraction of optical science and technology. This raises the question: if collisions of atoms and molecules with semiconductors could produce time-varying electric fields oscillating at similar frequencies, would they not also excite VB electrons to the CB and might this not provide important new avenues of research with the promise of new technology? If we were to adopt the physical picture derived from our study of metals, where electronic friction describes BOA failure, the answer to this question would certainly be 'no' or more precisely 'only weakly', as electronic-friction theories lead to hot EHP distributions that still favour low-energy excitation near the Fermi level¹². Unfortunately, scattering experiments with semiconductors that test the validity of the BOA are rare. Transient currents were observed when Xe atoms with energies between 3 and 10 eV were scattered from surfaces of semiconductors¹⁴⁻¹⁶. However, this resulted from the creation of a local hot spot where initial phonon excitation subsequently transferred energy to EHPs. While these experiments provide us with clear evidence of BOA failure in a semiconductor, we can gain only little insight into the dynamics of the atom-surface collision. In fact, an electronically adiabatic model could describe the energy loss of scattered Xe atoms.

In the work presented in this article, we produce H atoms whose speeds are high enough to test the limits of the BOA directly by investigating the characteristics of their collisions with a semiconductor surface. The measured H atom energy-loss spectra and angular distributions reveal the excitations appearing in the solid on the sub-picosecond time scale. We find that, not only is VB-CB excitation possible, at sufficiently high energies it dominates the energy-transfer dynamics, showing that new physical mechanisms are at play. Specifically, we present translational energy-loss measurements on energetic H atoms scattered from a reconstructed Ge(111)c(2 × 8) surface along with first principles electronically adiabatic MD simulations, performed with a newly developed high-dimensional neural-network PES (NN-PES). When incidence energies are below the bandgap, only one scattering channel arises with small energy losses nearly identical to those seen in the MD simulations. These exhibit collision dynamics similar to those seen in H scattering from Xe. Surprisingly, at higher incidence energies, a second channel appears whose energy-loss onset is coincident with the semiconductor bandgap. This channel is absent in the MD simulations with and without electronic friction. The importance of this channel increases rapidly with H atom velocity—a signature of BOA failure—and accounts for ~90% probability at the highest H atom incidence energies of this work.

Results

Figure 1 shows experimental translational energy-loss distributions for H atoms scattered from Ge(111)c(2 × 8)¹⁷ at incidence energies E_i above and below the 0.49 eV surface bandgap¹⁸. We note that the given value for the surface bandgap was determined at a surface temperature of 30 K. However, a similar value is expected at room temperature since the reconstruction of the surface is unchanged. Also shown are the predictions of the electronically adiabatic MD trajectory calculations. Below the bandgap (Fig. 1a) only a single feature appears in the energy-loss distribution. The MD simulations reproduce the experimental result extremely well. MD simulations with electronic friction¹⁹ at the level of local density friction approximation (LDFA)²⁰ fail to describe the energy-loss distributions (Extended Data Fig. 1). Analysis of adiabatic MD trajectories shows that H atoms interact with the Ge surface for only a few femtoseconds and that energy exchange is limited. Figure 1b-d

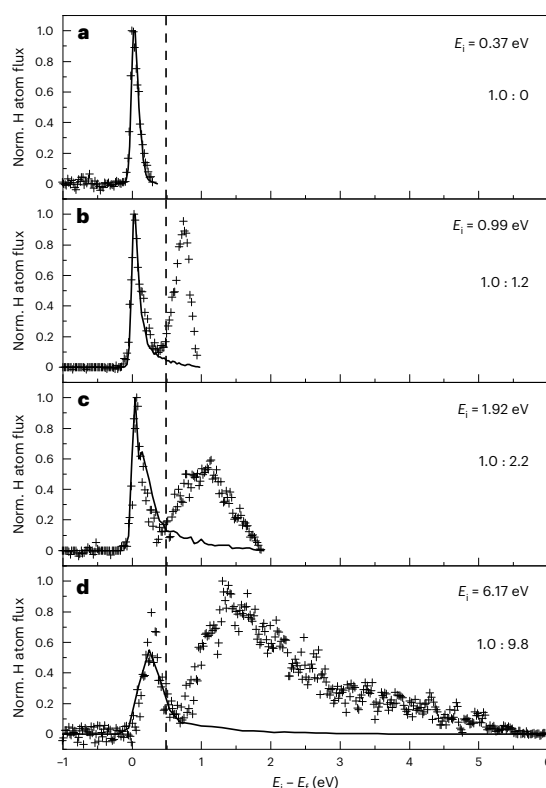


Fig. 1 | Translational energy-loss distributions for H atoms scattered from Ge(111)c(2 × 8). The incident H atoms travel along the [110] surface direction, while the polar incidence and scattering angles θ_i and θ_r , respectively, were both 45° with respect to the surface normal. The surface temperature T_s was 300 K. **a–d.** Experimental data (+) and the results of adiabatic molecular dynamics simulations (solid lines) for four H atom translational incidence energies are shown: $E_i = 0.37$ eV (**a**), 0.99 eV (**b**), 1.92 eV (**c**) and 6.17 eV (**d**). The bandgap of the surface is 0.49 eV and is indicated by the vertical dashed line. The experimentally obtained ratio of the adiabatic to the VB-CB channel appears in each panel. All experimental curves are normalized to the peak intensity. The MD curves are scaled to fit the adiabatic channel.

shows energy-loss distributions for three values of E_i larger than the surface bandgap. In all three cases, the distributions are bimodal and the MD trajectories reproduce only the feature seen at low values of energy loss. Hereafter, we refer to this feature as the adiabatic channel. The second feature appearing at higher energy losses is absent in the adiabatic MD simulations, strongly suggesting that this channel involves conversion of H atom translational energy to electronic excitation of the Ge solid. This idea is further supported by the observation that the energy-loss onset of this feature is coincident (within experimental uncertainty) with the Ge surface bandgap of 0.49 eV at all values of E_i . Furthermore, as expected for a channel involving BOA failure, this channel is strongly promoted by incidence translational energy, becoming about 90% of the observed scattering at the highest value of $E_i = 6.17$ eV. For these reasons, we assign the high energy-loss feature to an electronically non-adiabatic process where the collision of the H atom at the surface promotes an electron above the bandgap of the Ge surface. We refer to this mechanism hereafter as the VB-CB channel.

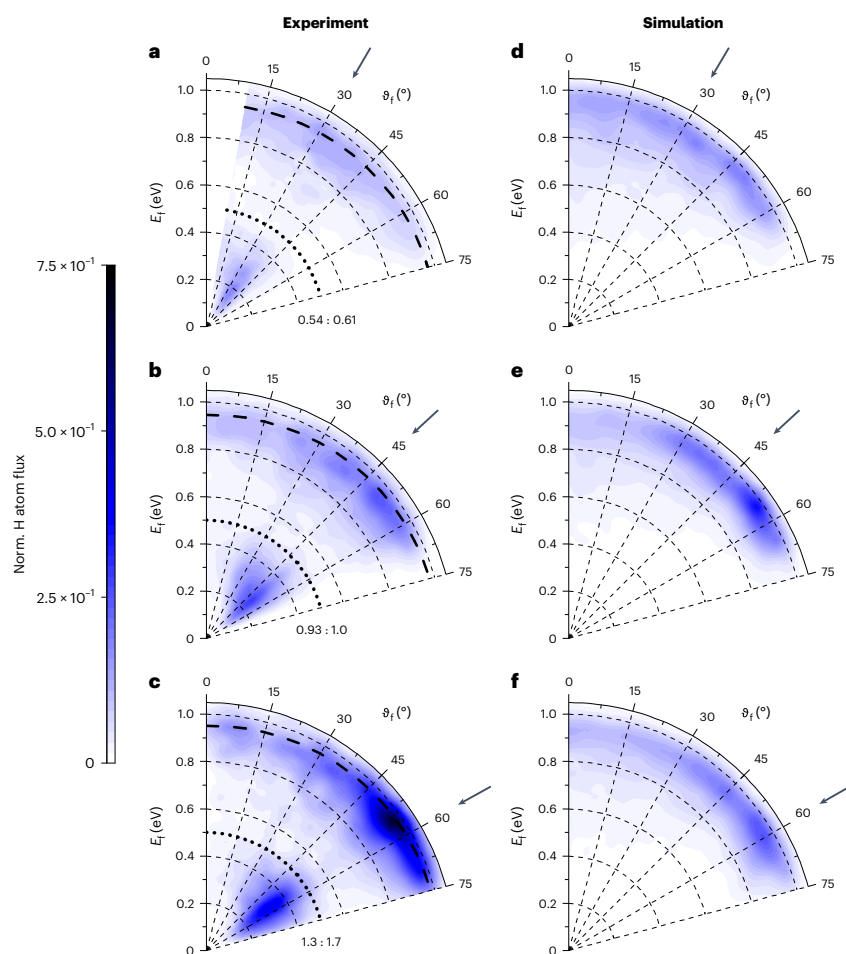


Fig. 2 | Incidence-angle dependence of H atoms scattered from Ge(111)c(2 × 8). Energy-resolved angular distributions derived from in-plane scattering flux are shown for three incidence angles, $\theta_i = 30, 45$ and 60° and an incidence translational energy $E_i = 0.99$ eV. The surface temperature was $T_s = 300$ K. **a–f**, Experimental results (**a–c**) are compared to MD simulations (**d–f**). The adiabatic and the VB–CB channels both exhibit maximum scattering flux near the specular scattering angle (arrows). The MD simulations reproduce the behaviour of the adiabatic channel only. To construct the experimental plots, data were recorded in 5° increments from $\theta_f = 0$ to 75° . All six polar plots are normalized

to the incident H atom flux. The numbers show the ratios of the experimentally observed scattering channels with respect to the adiabatic channel for an incidence angle of $\theta_i = 45^\circ$: the left one corresponds to the VB–CB channel and the right one to the adiabatic channel. The MD simulations are scaled to experiment such that at an incidence angle of $\theta_i = 45^\circ$, the integrated adiabatic channels are equal in both. The black dashed lines represent the final energy predicted by a line-of-centres binary collision model: $E_f = E_i [1 - \cos^2[(\theta_i + \theta_f)/2] \times [1 - (m_H - m_{Co})^2 / (m_H + m_{Co})^2]]$. The black dotted lines indicate the surface bandgap of 0.49 eV.

Figure 2 shows differential properties from both experiment and theory for H atoms incident at three angles θ_i and at $E_i = 0.99$ eV. Here, polar plots display the final translational energy E_f as a function of final scattering angle θ_f . The black dotted lines show the expected minimal energy loss for excitation of an electron across the surface bandgap, which demarcates the adiabatic from the VB–CB channel. Experiment shows that the VB–CB channel exhibits a much narrower angular distribution (Table 1) than the adiabatic channel at all three incidence angles. The MD simulations yield similar differential scattering maps as seen in experiment for the adiabatic channel only. The energy loss agrees with experiment and even the experimentally observed dependency

of the angular distribution on θ_i is reproduced. The VB–CB channel is absent in the MD simulations.

Figure 3 shows polar plot representations similar to Fig. 2 emphasizing the incidence energy dependence of the scattering. As before, the experimental results show bimodal scattering distributions with two well-resolved channels separated in energy space by the bandgap energy, marked as black dotted lines. The angular distributions of both channels broaden between $E_i = 0.99$ and 1.92 eV, but the VB–CB channel broadens significantly more as it is narrower at $E_i = 0.99$ eV (Table 1). The adiabatic MD simulations (Fig. 3c,d) reproduce this effect for the adiabatic channel.

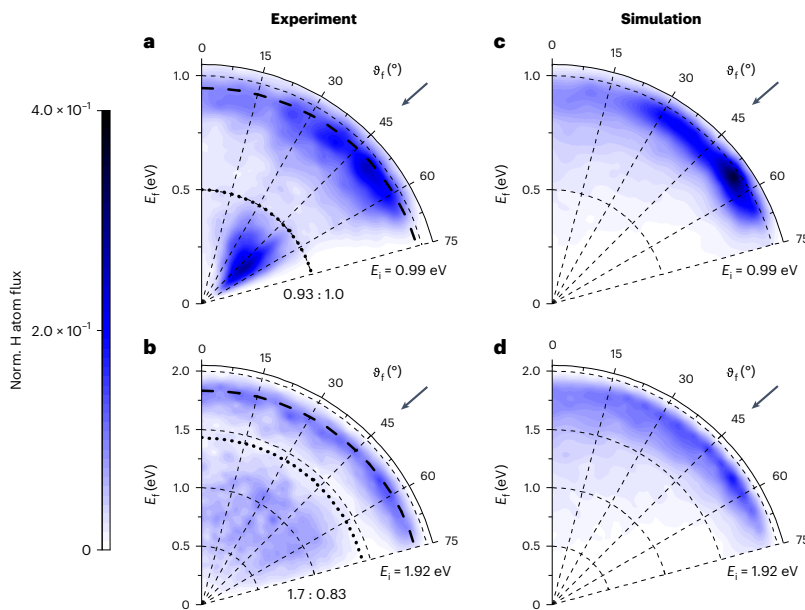


Fig. 3 | Incidence-energy dependence of H atoms scattered from Ge(111)c(2 × 8). **a–d.** Energy-resolved angular distributions derived from in-plane scattering flux are shown for two incidence translational energies $E_i = 0.99$ eV (**a** and **c**) and 1.92 eV (**b** and **d**). The surface temperature was $T_s = 300$ K and the incidence angle is $\theta_i = 45^\circ$. Experimental results (**a** and **b**) are compared to MD simulations (**c** and **d**). The MD simulations reproduce the behaviour of the adiabatic channel only. To construct the experimental plots, data were recorded in 5° increments from $\theta_f = 0$ to 75° . All four polar plots are normalized to the incident H atom flux. The

numbers show the ratios of the experimentally observed scattering channels with respect to the adiabatic channel for an incidence energy of $E_i = 0.99$ eV: the left one corresponds to the VB–CB channel and the right one to the adiabatic channel. The MD simulations are scaled to experiment such that at an incidence energy of $E_i = 0.99$ eV, the integrated adiabatic channels are equal in both. The black dashed lines represent the final energy predicted by a line-of-centres binary collision model: $E_f = E_i [1 - \cos^2((\theta_i + \theta_f)/2) \times [1 - (m_H - m_{Ge})^2 / (m_H + m_{Ge})^2]]$. The black dotted lines indicate the surface bandgap of 0.49 eV.

The average energy losses derived from the experiments are summarized in Table 2. Note that for the adiabatic channel, the average energy transferred to the surface $\langle E_i - E_f \rangle$ is a small and nearly constant fraction ($10 \pm 5\%$) of E_i . The VB–CB channel behaves differently, as the fraction of incidence energy transferred to the solid goes up dramatically as E_i is reduced. This is an influence of the surface bandgap, where the absolute of energy lost must exceed 0.49 eV, regardless of E_i . Hence, at lower values of E_i the fractional energy loss must sharply increase. Note also that the average energy lost decreases only slightly with increasing θ_f for both channels.

Discussion

We start by highlighting some of the key observations just presented and their implications. First, Fig. 2 shows clearly that the most probable value of θ_f depends on the chosen value of θ_i , proving the scattered atoms did not thermalize with the solid. Thermalization occurs on the picosecond timescale. Thus, we conclude that the scattered atoms in both channels experience a sub-picosecond interaction time with the surface. Second, there is evidence of sticking, even though integrated scattering probabilities such as sticking probabilities cannot be easily obtained from in-plane differential scattering measurements, since the fraction of incident atoms that scatter out of the detection plane may also depend on incidence conditions and branching channel. We can nevertheless integrate the observed scattering at flux over E_f and θ_f . These integrals scaled to the experimentally observed adiabatic channel at $E_i = 0.99$ eV and $\theta_i = 45^\circ$ appear as numbers next to each differential scattering diagram in Figs. 2 and 3. They are given as ratios that report the relative contributions of the two scattering channels. There is an overall loss of signal between $E_i = 1.92$ and 0.99 eV. If we were to

Table 1 | Angular full width at half maximum for the experimental angular distributions of this work

E_i	VB–CB			Adiabatic		
	$\theta_i = 30^\circ$	$\theta_i = 45^\circ$	$\theta_i = 60^\circ$	$\theta_i = 30^\circ$	$\theta_i = 45^\circ$	$\theta_i = 60^\circ$
0.99 eV	24°	31°	24°	>56°	44°	34°
1.92 eV	–	>70°	–	–	>73°	–

assume the out-of-plane scattering fraction was independent of E_i , we would conclude that the sticking probability decreases with increasing incidence energy. A similar trend is seen in the MD simulations. Note also that the branching ratios shown in Fig. 3a,b are consistent with those of Fig. 1b,c, which represent the branching between the two scattering channels detected at $\theta_f = 45^\circ$ only. This agreement suggests that the branching seen in Fig. 1c ($E_i = 1.92$ eV) is representative of other scattering angles.

The major outcome of this work is the observation that an H atom scattering from a semiconductor may experience one or the other of two types of interaction, either a mechanical interaction well described within the BOA or a strong non-adiabatic interaction capable of promoting an electron to energies above the bandgap. We emphasize that while there are similarities with past work, the behaviour seen here is qualitatively different from previous observations involving insulators, metals or semi-metals. For example, the adiabatic channel seen in Figs. 1–3 exhibits marked similarities to H atom scattering from insulating Xe. However, that system exhibited no BOA failure whatsoever. Conversely, H scattering trajectories describing collisions with metals simultaneously excite both phonons and EHPs (refs. 10–13), the two excitations being inextricably linked

Table 2 | Average energy-loss in experimentally obtained specular ($\theta_i = \theta_r$) H atom scattering

E_i	θ_i	VB-CB		Adiabatic	
		$\langle E_i - E_f \rangle$	$\frac{\langle E_i - E_f \rangle}{E_i} \times 100$	$\langle E_i - E_f \rangle$	$\frac{\langle E_i - E_f \rangle}{E_i} \times 100$
0.37 eV	45°	–	–	0.05 eV	14% (13%)
0.99 eV	30°	0.75 eV	75%	0.15 eV	15% (17%)
	45°	0.71 eV	72%	0.13 eV	13% (12%)
	60°	0.69 eV	70%	0.10 eV	10% (8.1%)
1.92 eV	45°	1.12 eV	58%	0.20 eV	10% (14%)
6.17 eV	45°	2.28 eV	37%	0.32 eV	5.2% (7.7%)

Values in parentheses were computed from adiabatic MD trajectories

to one another. The question remains, what gives rise to the branching between the two channels in the H/Ge system?

The fact that H scattering from Ge exhibits branching behaviour between two distinct dynamical channels is consistent with a two-state picture. We envision that the H atom proceeds initially along the ground electronic state until it encounters a seam of crossing associated with a short-lived electronically excited state. (Note that the word state is used here loosely as many electronic states are involved in the VB and CB of the system.) We assume that this state rapidly decays into unoccupied electronic states within the CB. At low incidence energies, reaching the seam of crossing requires specific approach, but at higher energies other regions of the seam become accessible with reduced steric restrictions.

Evidence supporting this picture can be found in observations of this work, especially Fig. 2. Note that the VB-CB channel exhibits a narrow angular distribution, peaking near the specular scattering angle (arrows in Fig. 2). This shows that there is no preference for loss of incidence energy parallel or perpendicular to the surface when inducing electronic excitation. A narrow angular distribution is typical of scattering influenced by directional forces associated with atomic orbitals with preferred orientations, which is consistent with the suggested mechanism of a curve crossing, where H atom collisions must occur at specific surface sites (Ge atoms) and with specific approaching geometries. Figure 3 shows that at a higher energy these steric restrictions appear to be less severe and consequently the VB-CB scattering angular distribution broadens.

Contrasting this behaviour, the adiabatic channel exhibits a markedly broader angular distribution even at low incidence energies. This indicates a large corrugation of the PES experienced by the atoms passing through the adiabatic channel. Despite the many final scattering angles, the energy loss follows a hard-sphere line-of-centres binary collision model (black dashed lines). This indicates that the H atom scattered through the adiabatic channel is experiencing binary collisions with many impact parameters. It is not surprising, due to the complex surface structure of the Ge(111)c(2 × 8) surface, if the H atoms scattering through the adiabatic channel sample a large fraction of the surface unit cell.

Bimodal energy-loss distributions may be produced without electronic excitation. For example, H scattering from a graphene layer involves trajectories that either fail or succeed in surmounting a chemisorption barrier^{5–7}. H atoms reflected from the barrier experience weak van der Waals interactions with little energy transferred, while H atoms surmounting the barrier couple strongly to in-plane phonons of the graphene layer⁵. In contrast to this behaviour, the electronically adiabatic MD simulations carried out in this work show no sign of bimodal distributions. This is consistent with the absence of a chemisorption barrier in the H/Ge system. The combined strength of the experimental and theoretical results supports our assignment of an electronically adiabatic and a non-adiabatic channel.

While it is common knowledge that absorption of photons in the bulk of a semiconductor excites electrons from the VB to the CB, this work shows that a colliding atom may efficiently promote electrons in a similar way in a purely surface-specific process. The probability to convert translational energy of the H atom to electronic excitation of the solid dramatically increases with incidence energy, as does the average excitation energy. The large excitation probability as well as the large energy loss is inconsistent with electronic-friction theories. Hence, this work stands as a challenge for new theories of electronically non-adiabatic surface chemistry. We hasten to add that the designation of this behaviour as VB-CB represents a simplified viewpoint. The precise nature of the excited electronic states involved is still unknown. Transient surface-localized excitations (even plasmons) might be important. Nevertheless, the observation that electronic excitation dominates the dynamics in collisions of a simple atom with a semiconductor opens new horizons for research into non-adiabatic effects in surface chemistry and chemical sensors.

Online content

Any methods, additional references, Nature Portfolio reporting summaries, source data, extended data, supplementary information, acknowledgements, peer review information; details of author contributions and competing interests; and statements of data and code availability are available at <https://doi.org/10.1038/s41557-022-01085-x>.

References

- Born, M. & Oppenheimer, R. Zur Quantentheorie der Molekeln. *Ann. Phys.* **84**, 0457–0484 (1927).
- Tully, J. C. Perspective on “Zur Quantentheorie der Molekeln” - Born M, Oppenheimer R (1927) *Ann Phys* 84: 457. *Theor. Chem. Acc.* **103**, 173–176 (2000).
- Bünermann, O., Kandratsenka, A. & Wodtke, A. M. Inelastic scattering of H atoms from surfaces. *J. Phys. Chem. A* **125**, 3059–3076 (2021).
- Hertl, N., Kandratsenka, A., Bünermann, O. & Wodtke, A. M. Multibounce and subsurface scattering of H atoms colliding with a van der Waals solid. *J. Phys. Chem. A* **125**, 5745–5752 (2021).
- Jiang, H. Y. et al. Imaging covalent bond formation by H atom scattering from graphene. *Science* **364**, 379–382 (2019).
- Jiang, H. Y. et al. Small nuclear quantum effects in scattering of H and D from graphene. *J. Phys. Chem. Lett.* **12**, 1991–1996 (2021).
- Wille, S. et al. An experimentally validated neural-network potential energy surface for H-atom on free-standing graphene in full dimensionality. *Phys. Chem. Chem. Phys.* **22**, 26113–26120 (2020).
- Tully, J. C. Chemical dynamics at metal surfaces. *Annu. Rev. Phys. Chem.* **51**, 153–178 (2000).
- Wodtke, A. M., Tully, J. C. & Auerbach, D. J. Electronically non-adiabatic interactions of molecules at metal surfaces: Can we trust the Born–Oppenheimer approximation for surface chemistry? *Int. Rev. Phys. Chem.* **23**, 513–539 (2004).
- Bünermann, O. et al. Electron-hole pair excitation determines the mechanism of hydrogen atom adsorption. *Science* **350**, 1346–1349 (2015).
- Jiang, H. Y., Dorenkamp, Y., Krüger, K. & Bünermann, O. Inelastic H and D atom scattering from Au(111) as benchmark for theory. *J. Chem. Phys.* **150**, 184105 (2019).
- Kandratsenka, A. et al. Unified description of H-atom-induced chemisorption and inelastic scattering. *Proc. Natl Acad. Sci. USA* **115**, 680–684 (2018).
- Dorenkamp, Y. et al. Hydrogen collisions with transition metal surfaces: Universal electronically nonadiabatic adsorption. *J. Chem. Phys.* **148**, 034706 (2018).
- Amirav, A. & Cardillo, M. J. Electron-hole pair creation by atomic scattering at surfaces. *Phys. Rev. Lett.* **57**, 2299–2302 (1986).

4 Hydrogen atom scattering from germanium surfaces

Article

<https://doi.org/10.1038/s41557-022-01085-x>

15. Amirav, A. et al. Electron-hole pair creation at a Ge(100) surface by ground-state neutral Xe atoms. *J. Appl. Phys.* **59**, 2213–2215 (1986).
16. Weiss, P. S., Amirav, A., Trevor, P. L. & Cardillo, M. J. Hyperthermal gas-surface scattering. *J. Vac. Sci. Technol. A* **6**, 889–894 (1988).
17. Chadi, D. J. & Chiang, C. New $c - 2 \times 8$ unit cell for the Ge(111) surface. *Phys. Rev. B* **23**, 1843–1846 (1981).
18. Feenstra, R. M., Lee, J. Y., Kang, M. H., Meyer, G. & Rieder, K. H. Band gap of the Ge(111) $c(2 \times 8)$ surface by scanning tunneling spectroscopy. *Phys. Rev. B* **73**, 035310 (2006).
19. Head-Gordon, M. & Tully, J. C. Molecular dynamics with electronic frictions. *J. Chem. Phys.* **103**, 10137–10145 (1995).
20. Juaristi, J. I., Alducin, M., Muino, R. D., Busnengo, H. F. & Salin, A. Role of electron-hole pair excitations in the dissociative adsorption of diatomic molecules on metal surfaces. *Phys. Rev. Lett.* **100**, 116102 (2008).

Publisher's note Springer Nature remains neutral with regard to jurisdictional claims in published maps and institutional affiliations.

Open Access This article is licensed under a Creative Commons Attribution 4.0 International License, which permits use, sharing, adaptation, distribution and reproduction in any medium or format, as long as you give appropriate credit to the original author(s) and the source, provide a link to the Creative Commons license, and indicate if changes were made. The images or other third party material in this article are included in the article's Creative Commons license, unless indicated otherwise in a credit line to the material. If material is not included in the article's Creative Commons license and your intended use is not permitted by statutory regulation or exceeds the permitted use, you will need to obtain permission directly from the copyright holder. To view a copy of this license, visit <http://creativecommons.org/licenses/by/4.0/>.

© The Author(s) 2022

Methods

The experimental setup is described in detail in refs. ^{3,21}. Briefly, ultraviolet ($\lambda_{\text{photolysis}} = 248.35 \text{ nm}$) or vacuum ultraviolet ($\lambda_{\text{photolysis}} = 121.4 \text{ nm}$) photodissociation of a supersonic molecular beam of hydrogen iodide produces a H atom beam with translational energies of $E_i = 0.37, 0.99, 1.92$ or 6.17 eV that then passes through two differential pumping chambers to enter an ultra-high vacuum scattering chamber before colliding with a germanium crystal. The Ge sample is held on a five-axis manipulator, allowing the variation of the polar incidence angle θ_i with respect to the surface normal. The scattered H atoms are excited to a long-lived Rydberg state just below the ionization limit²² and fly 250 mm before they are field ionized and detected by a multichannel plate assembly. A multichannel scaler records the arrival time to obtain the time-of-flight distributions, which we convert to energy spectra by applying the appropriate Jacobians. The detector is rotatable in the plane defined by the incident H atom beam and the surface normal allowing time-of-flight distributions to be obtained at various final scattering angles θ_f . The used Ge crystal is undoped with a purity of 99.999%. The Ge(111) surface was cleaned with cycles of Ar⁺ ion sputtering and annealing to $-670 \text{ }^\circ\text{C}$. Auger electron spectroscopy (AES) and low-energy electron diffraction (LEED) validated the cleanliness and $c(2 \times 8)$ structure of the surface.

To perform theoretical simulations, a neural-network PES (NN-PES) was constructed for the H@Ge(111) $c(2 \times 8)$ system and MD simulations were performed. Data for the NN fitting were obtained with spin-polarized DFT calculations, carried out with the Vienna Ab initio Simulation Package (VASP)^{23,24} with the frozen-core all-electron projector-augmented wave (PAW) method^{25,26}. The electronic wave function was expanded using plane waves with an energy cutoff of 250 eV. The electron exchange-correlation energies were described by the Perdew-Burke-Ernzerhof (PBE) functional within the generalized gradient approximation (GGA)²⁷. The reconstructed Ge(111) $c(2 \times 8)$ surface was modelled by repeated slabs separated by a vacuum space of 16 Å in the z direction. Each slab contained eight atomic layers, with four additional Ge adatoms added on top of the first layer. The Ge atoms in the bottom layer not seen by the scattering H atoms in the MD simulations were capped by Ge-H bonds. The Ge adatoms and top six layers were allowed to move while the remaining atoms were fixed throughout the calculations. Therefore, there were a total of 101 movable atoms in the unit cell. The Brillouin zone was sampled with a $3 \times 1 \times 1$ k-point grid. Ab initio molecular dynamics (AIMD) trajectories were used to provide training data for the NN fitting. The AIMD trajectories employed initial positions of the H atom randomly sampled 6 Å above the surface. About 100 AIMD trajectories were run for H atoms with incidence energies of 0.99 and 1.92 eV, an incidence angle of 45° and a surface temperature of 300 K, providing $\sim 150,000$ points. Additional single-point DFT calculations were performed to augment the AIMD points. The data set were culled using a Euclidean distance of 0.3 Å to remove points that were too close to one another. About 26,000 points (including both energy and gradient) were finally selected to fit a 303-dimensional PES using an embedded-atom neural network (EANN) approach²⁸. The EANN PES obtained in this way was thoroughly tested, giving a root-mean-square error (RMSE) of about 80 meV per cell (or 0.8 meV per atom). MD trajectories were calculated with a modified Venus program²⁹. The timesteps were chosen separately for each incidence energy: 0.10, 0.05, 0.03 and 0.01 fs for 0.37, 0.99, 1.92 and 6.17 eV, respectively.

To study possible non-adiabatic effects, an electron-friction model was applied^{19,30}. The electronic-friction coefficient was calculated based on the local-density friction approximation (LDFA)^{20,31}. The electron density of the Ge(111) $c(2 \times 8)$ surface was obtained from about 100 configurations at 300 K. To obtain an analytical expression for the electron density the data were again fitted with the EANN method.

Data availability

Source data are provided with this paper.

Code availability

The EANN code of B.J. is available at <https://github.com/zhangylich/REANN>. The VENUS code is available at <https://www.depts.ttu.edu/chemistry/Venus/index.php>.

References

- Bünemann, O., Jiang, H. Y., Dorenkamp, Y., Auerbach, D. J. & Wodtke, A. M. An ultrahigh vacuum apparatus for H atom scattering from surfaces. *Rev. Sci. Instrum.* **89**, 094101 (2018).
- Schnieder, L., Seekampprahn, K., Liedeker, F., Steuwe, H. & Welge, K. H. Hydrogen-exchange reaction H + D₂ in crossed beams. *Faraday Discuss.* **91**, 259–269 (1991).
- Kresse, G. & Furthmüller, J. Efficient iterative schemes for ab initio total-energy calculations using a plane-wave basis set. *Phys. Rev. B* **54**, 11169–11186 (1996).
- Kresse, G. & Furthmüller, J. Efficiency of ab initio total energy calculations for metals and semiconductors using a plane-wave basis set. *Comput. Mater. Sci.* **6**, 15–50 (1996).
- Blöchl, P. E. Projector augmented-wave method. *Phys. Rev. B* **50**, 17953–17979 (1994).
- Kresse, G. & Joubert, D. From ultrasoft pseudopotentials to the projector augmented-wave method. *Phys. Rev. B* **59**, 1758–1775 (1999).
- Perdew, J. P., Burke, K. & Ernzerhof, M. Generalized gradient approximation made simple. *Phys. Rev. Lett.* **77**, 3865–3868 (1996).
- Zhang, Y. L., Hu, C. & Jiang, B. Embedded atom neural network potentials: Efficient and accurate machine learning with a physically inspired representation. *J. Phys. Chem. Lett.* **10**, 4962–4967 (2019).
- Hase, W. L. et al. VENUS96: A general chemical dynamics computer program. *QCPE Bulletin* **16**, 671 (1996).
- Li, Y. G. & Wahnström, G. Nonadiabatic effects in hydrogen diffusion in metals. *Phys. Rev. Lett.* **68**, 3444–3447 (1992).
- Puska, M. J. & Nieminen, R. M. Atoms embedded in an electron gas: Phase shifts and cross sections. *Phys. Rev. B* **27**, 6121–6128 (1983).

Acknowledgements

We thank D.J. Auerbach and A. Kandratsenka for helpful discussions. A.M.W. thanks the Max Planck Society for the Advancement of Science. O.B. and A.M.W. acknowledge support from the Deutsche Forschungsgemeinschaft (DFG) under SFB 1073 (217133147), project A04 and from the DFG, the Ministerium für Wissenschaft und Kultur, Niedersachsen and the Volkswagenstiftung under grant no. INST 186/902-1. A.M.W. and H.G. acknowledge support from the Alexander von Humboldt Foundation. H.G. acknowledges support from the National Science Foundation under grant no. CHE-1951328. B.J. acknowledges support from the National Natural Science Foundation of China under grant no. 22073089 and from the K. C. Wong Education Foundation under grant no. GJTD-2020-15.

Author contributions

A.M.W. and O.B. conceived the project. O.B. supervised the experiments and H.G. and B.J. supervised the theoretical simulations. K.K. performed the experiments and S.T., F.D. and A.M. assisted in part of the experiments. Y.W., X.Z., B.J. and H.G. constructed the NN-PES and Y.W. performed the MD simulations. K.K. and Y.W. analysed the data. K.K. and O.B. wrote the manuscript with feedback from A.M.W., Y.W., N.H., B.J. and H.G.

4 Hydrogen atom scattering from germanium surfaces

Article

<https://doi.org/10.1038/s41557-022-01085-x>

Funding

Open access funding provided by Max Planck Society.

Competing interests

The authors declare no competing interests.

Additional information

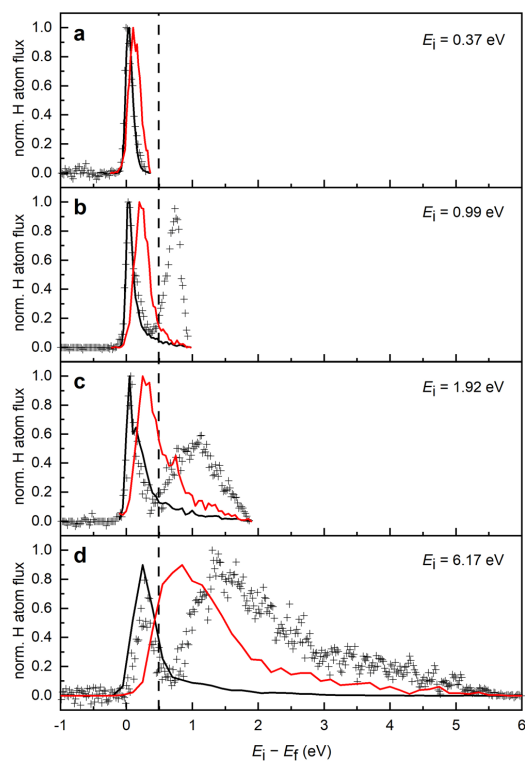
Extended data is available for this paper at <https://doi.org/10.1038/s41557-022-01085-x>.

Correspondence and requests for materials should be addressed to Oliver Bünermann.

Peer review information *Nature Chemistry* thanks Eckart Hasselbrink, Hermann Nienhaus and the other, anonymous, reviewer(s) for their contribution to the peer review of this work.

Reprints and permissions information is available at www.nature.com/reprints.

4.1 Evidence of adiabatic and non-adiabatic energy transfer



Extended Data Fig. 1 | Comparison of molecular dynamics including electronic friction (EF) to adiabatic MD simulations and experiment.

The incident H atoms travel along the $[110]$ surface direction, while the polar incidence and scattering angles θ_i and θ_r , respectively, were both 45° with respect to the surface normal. The surface temperature T_s was 300 K. **a-d**, Experimental data (+) as well as the results of adiabatic MD simulations (black solid lines) and

MD simulations including EF (red solid lines) for four H atom translational incidence energies are shown: $E_i = 0.37$ eV (**a**), 0.99 eV (**b**), 1.92 eV (**c**) and 6.17 eV (**d**). The bandgap of the surface is 0.49 eV and indicated by the vertical dashed line. All experimental curves are normalized to the peak intensity. The MD curves are scaled to fit the experiment.

4 Hydrogen atom scattering from germanium surfaces

4.2 The isotope effect: H and D atom scattering

Section 4.2 is comprised of Ref. [151], an open access article titled "*Isotope effect suggests site-specific nonadiabaticity on Ge(111)c(2 × 8)*", published in *Natural Sciences*. The article (DOI 10.1002/ntls.20230019) is licensed under a Creative Commons Attribution 4.0 International License (CC BY 4.0) (<https://creativecommons.org/licenses/by/4.0/>).

Material from: Kerstin Krüger, Yingqi Wang, Lingjun Zhu, Bin Jiang, Hua Guo, Alec M. Wodtke & Oliver Bünermann, Isotope effect suggests site-specific nonadiabaticity on Ge(111)c(2 × 8), *Natural Sciences*, published 2023, Wiley-VCH.

In this article, the isotope effect is investigated by comparing H and D atom scattering from Ge(111)c(2 × 8) with the aim of verifying our prior interpretation of the adiabatic scattering channel and gaining new insights concerning the non-adiabatic scattering channel. Results of electronically adiabatic molecular dynamics simulations are provided by the group of Prof. Dr. Hua Guo, University of New Mexico, NM, USA. The adiabatic channel shows an isotope effect that can be explained by the mass difference of H and D atoms and is reproduced by MD simulations. The non-adiabatic channel shows almost no isotope effect and is absent in the simulations. Supported by electronic band structure calculations provided by the group of Prof. Dr. Bin Jiang, University of Science and Technology of China, Hefei, China, site-specific scattering dynamics are suggested for this channel.






The article is Ref. [151] in this thesis:

[151] K. Krüger, Y. Wang, L. Zhu, B. Jiang, H. Guo, A. M. Wodtke, O. Bünermann, Isotope effect suggests site-specific nonadiabaticity on Ge(111)c(2 × 8), *Nat. Sci.* **2023**, e20230019, <https://doi.org/10.1002/ntls.20230019>.

Author contributions:

K.K. performed the experiments. Y.W. and L.Z. performed the simulations. Y.W. and K.K. analyzed the data. O.B. and K.K. wrote the manuscript with feedback from A.M.W., Y.W., L.Z., B.J. and H.G.

Isotope effect suggests site-specific nonadiabaticity on Ge(111)c(2×8)

Kerstin Krüger¹  | Yingqi Wang^{2,3} | Lingjun Zhu⁴ | Bin Jiang⁴  | Hua Guo^{2,3}  |
Alec M. Wodtke^{1,5,6}  | Oliver Bünermann^{1,5,6} 

¹Institute of Physical Chemistry, Georg-August University, Göttingen, Germany

²Department of Chemistry and Chemical Biology, University of New Mexico, Albuquerque, New Mexico, USA

³Center for Computational Chemistry, University of New Mexico, Albuquerque, New Mexico, USA

⁴Key Laboratory of Precision and Intelligent Chemistry, Department of Chemical Physics, University of Science and Technology of China, Hefei, China

⁵Department of Dynamics at Surfaces, Max-Planck-Institute for Multidisciplinary Sciences, Göttingen, Germany

⁶International Center of Advanced Studies of Energy Conversion, Georg-August University, Göttingen, Germany

Correspondence

Oliver Bünermann, Institute of Physical Chemistry, Georg-August University, Göttingen, Germany.

Email:

oliver.buenermann@chemie.uni-goettingen.de

Funding information

Max-Planck-Gesellschaft; Deutsche Forschungsgemeinschaft, Grant/Award Numbers: INST 186/902-1, SFB1073, projectA04(217133147); National Science Foundation, Grant/Award Numbers: CHE-1951328, CHE-2306975; Volkswagen Foundation, Grant/Award Number: INST 186/902-1; Niedersächsisches Ministerium für Wissenschaft und Kultur, Grant/Award Number: INST 186/902-1; Alexander von Humboldt-Stiftung; K. C. Wong Education Foundation, Grant/Award Number: GJTD-2020-15

Abstract

Energy transferred in atom-surface collisions typically depends strongly on projectile mass, an effect that can be experimentally detected by isotopic substitution. In this work, we present measurements of inelastic H and D atom scattering from a semiconducting Ge(111)c(2×8) surface exhibiting two scattering channels. The first channel shows the expected isotope effect and is quantitatively reproduced by electronically adiabatic molecular dynamics simulations. The second channel involves electronic excitations of the solid and, surprisingly, exhibits almost no isotope effect. We attribute these observations to scattering dynamics, wherein the likelihood of electronic excitation varies with the impact site engaged in the interaction.

Key Points

- Previous work revealed that H atoms with sufficient translational energy can excite electrons over the band gap of a semiconductor in a surface collision.
- We studied the isotope effect of the energy transfer by H/D substitution and performed band structure calculations to elucidate the underlying excitation mechanism.
- Our results suggest a site-specific mechanism that requires the atom to hit a specific surface site to excite an electron-hole pair.

KEYWORDS

Born–Oppenheimer failure, H atom, isotope effect, semiconductor, surface dynamics

This is an open access article under the terms of the [Creative Commons Attribution License](https://creativecommons.org/licenses/by/4.0/), which permits use, distribution and reproduction in any medium, provided the original work is properly cited.

© 2023 The Authors. *Natural Sciences* published by Wiley-VCH GmbH.

INTRODUCTION

A common experimental approach to elucidate reaction, scattering, and energy transfer mechanisms of atom–surface interactions employs the isotope effect, usually using H/D substitution.^{1–9} Depending on the underlying mechanism, different responses of the system to isotopic substitution are found. Inelastic scattering may result from mechanical excitation of lattice vibrations (phonons) by the impinging projectile. Here, the influence of isotopic substitution on energy transfer can be understood as the result of momentum conservation and D will transfer more energy than H. This behavior is seen for scattering from an insulator surface, where the energy loss of D atoms is about two times larger than for H atoms.¹⁰ Alternatively, electron-hole pairs (EHPs) can be excited by the collision via an electronic friction mechanism¹¹; here, iso-energetic H and D impinge at the surface with different velocities, resulting in reduced friction and reduced energy transfer for D compared to H. For example, strong isotope effects are observed in chemicurrent measurements,^{5,12–15} where ultrathin metal film Schottky diode detectors enable the direct detection of electronic excitation that results from chemisorption. Here, deuterium-induced chemicurrents are two to five times smaller than those measured with H atom exposure. In fact, both isotope effects are present in inelastic scattering experiments from metals,^{8,16,17} where a reduced isotope effect is due to compensation of two mass-dependent effects on the energy transfer: an increased energy loss to the phonon system and a decreased energy loss to electronic excitation for D compared to H.

In a recent study on H atom scattering from the semiconducting, reconstructed Ge(111)c(2×8) surface, a bimodal energy-loss distribution was observed when the incident translational energy exceeds the energy of the surface band gap.¹⁸ One channel, which is present for translational energies both above and below the band gap, could be well described by an electronically adiabatic molecular dynamics (MD) simulation, whereas, until now, there are no theoretical models, including an electronic friction model capable of describing the second channel, which only emerges when translational energies exceed the surface band gap.¹⁹ Due to its large energy loss with an onset close to the surface band gap and its absence in the adiabatic simulations, the second channel was assigned to an electronically nonadiabatic process leading to the excitation of a surface electron across the surface band gap.

The goal of the present work is to provide further insights into the scattering dynamics by studying the isotope effect. This approach helps to confirm the previous conclusions of the adiabatic behavior of the first scattering channel; it also serves to help us gain a deeper understanding of the nature of the second nonadiabatic channel. In particular, we present translational energy-loss measurements of D atoms scattered from Ge(111)c(2×8) with incidence translational energies of about 1 and 2 eV and compare them to H atom scattering with similar incidence energies. The experiments reveal bimodal energy-loss distributions for D that are very similar to those for H; one scattering channel exhibits low energy loss, while the other one transfers much more energy to the surface. The experimental results are further compared to electronically adiabatic MD simulations, which were

performed using a high-dimensional neural network potential energy surface (NN-PES). MD simulations reproduce the energy-loss distribution for both isotopes, but only for one of the two scattering channels. Comparing the results of H to D atom scattering reveals that the adiabatic channel shows an isotope effect matching the prediction for an adiabatic energy transfer mechanism. In contrast, nearly no isotope effect is observed for the second, nonadiabatic channel. The results give further insights into the properties of the second channel suggesting the importance of site-specific nonadiabatic coupling.

METHODS

Experimental methods

The experimental setup is described in detail in Refs. 20, 21. In short, an H or D atomic beam with translational energies of $E_{iH} = 0.99$ and 1.92 eV or $E_{iD} = 0.94$ and 1.87 eV, is produced by ultraviolet photodissociation ($\lambda_{\text{photolysis}} = 248.35$ nm) of a supersonic molecular beam of hydrogen iodide or deuterium iodide, respectively. The H or D atom beam passes two differential pumping chambers to enter an ultra-high vacuum scattering chamber before colliding with the germanium crystal. The Ge sample is mounted on a 5-axis manipulator allowing the variation of the polar incidence angle ϑ_i with respect to the surface normal. The translational energy and angular distributions of the scattered H or D atoms are detected by Rydberg atom tagging time-of-flight. Here, the atoms are excited to a long-lived Rydberg state just below the ionization limit,²² pass a distance of 250 mm, are field-ionized, and then detected by a multichannel plate assembly. A multichannel scaler records the arrival time to obtain the time-of-flight (TOF) distributions, which we convert to energy spectra by applying the appropriate Jacobians. The detector is rotatable in the plane defined by the surface normal and the incident H/D atom beam allowing to measure TOF distributions at various final scattering angles ϑ_f . The used Ge crystal is undoped with a purity of 99.999%. The Ge(111) surface was cleaned with cycles of Ar⁺ ion sputtering and annealing at $\sim 670^\circ\text{C}$. The cleanliness and c(2×8) structure of the surface is validated by Auger electron spectroscopy and low-energy electron diffraction.

Theoretical methods

To perform theoretical simulations, a previously constructed NN-PES was improved and used for the D@Ge(111)c(2×8) system, and MD simulations were performed. For the MD simulations, the reconstructed Ge(111)c(2×8) surface was modeled using the c(2×8) surface unit cell, see Figure 1b. Details on the density functional theory (DFT) calculations, NN-PES, and MD simulations can be found in the Methods section of Ref. 18. Briefly, the Ge(111)c(2×8) slab consists of six mobile atomic layers plus two fixed layers with the bottom layer capped with H. The experimental lattice constant of 5.6575 Å²³ was used in the calculation. The supercell contains 148 atoms with a 3×1×1 *k*-grid. The Perdew–Burke–Ernzerhof functional²⁴ was used, and the core

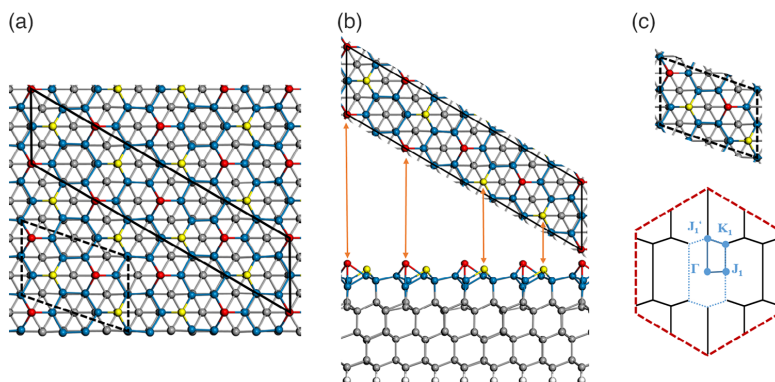


FIGURE 1 Top and side views of the Ge(111)c(2×8) surface structure and surface Brillouin zone. Panel (a) shows the Ge(111)c(2×8) surface structure in top view with marked c(2×8) surface unit cell (black solid line) and c(2×8) primitive surface unit cell (black dashed line). The red, yellow, blue, and gray balls represent adatoms, rest atoms, saturated atoms, and sublayer atoms, respectively. Panel (b) shows the c(2×8) surface unit cell used in MD simulations in top and side view. The black line in the top view represents the periodic boundary. The white balls are H atoms used to terminate unsaturated Ge atoms of the lowermost layer in the theoretical model. Orange arrows point to adatoms and rest atoms in the front row of the side view representation. Panel (c) shows the c(2×8) primitive surface unit cell as well as a schematic of the (1×1) (red dashed lines) and c(2×8) primitive (blue dotted lines) surface Brillouin zones.

electrons were treated with the augmented project wave method.²⁵ About 6000 points were added to the original dataset to cover more configuration space and the newly fitted NN-PES has a root mean square error of about 80 meV/cell (or 0.8 meV/atom). For each experimental condition, 400,000 trajectories were calculated to achieve sufficient statistics and the error due to statistical sampling is negligible. These trajectories were initiated with conditions mimicking the experimental conditions and only scattered trajectories within $\pm 20^\circ$ of the incidence plane were collected to imitate the in-plane experimental detection. For the energy-loss spectra, a polar acceptance angle of $\pm 2.5^\circ$ was chosen. For one experimental condition, a few percent of the overall trajectories contribute to the energy-loss spectrum.

To gain insight into the change of local electronic structures of specific surface sites upon hydrogen impact, we computed the band structures of the clean Ge(111)c(2×8) surface in a primitive cell (one-half the size of the Ge(111)c(2×8) cell, see Figure 1c)²⁶ and the ones with an H atom adsorbed at adatom or rest atom site. Spin-polarized DFT calculations were performed using the Vienna Ab initio Simulation Package (VASP)^{27,28} with a Meta Simple (MS2)²⁹ exchange-correlation functional at the meta-generalized gradient approximation (meta-GGA) level. This MS2 functional was chosen differently from that used for generating the NN-PES, because it yields similar band structures with a finite band gap for the Ge(111)c(2×8) surface (0.32 eV) as predicted by the more advanced yet much more costly hybrid functional (HSE06).³⁰ The plane-wave kinetic energy cutoff was 400 eV and the Brillouin zone was sampled by a $6 \times 2 \times 1$ Gamma-centered *k*-point grid. All adsorption geometries have been reoptimized with the MS2 functional and the same experimental lattice constant for band structure calculations. The suggested *k*-path in band structure calculations was along the Γ - J_1 - K_1 - J_1 - Γ symmetry directions in the Brillouin zone of the clean surface. The VASPKIT code³¹ was used for post-processing of the VASP calculated data. Other settings of

the slab model are identical to those used for generating the training data of the NN-PES, as detailed in Ref. 18. A more complete theoretical analysis of this system will be described in a forthcoming publication.

RESULTS

Figure 2 shows experimental translational energy-loss distributions for H and D atoms scattered from Ge(111)c(2×8) with incidence energies, E_i , of approximately 1 eV (Figure 2a) and 2 eV (Figure 2b). At both incidence energies, bimodal energy-loss distributions are obtained for both isotopes. One channel shows low energy loss, while the other channel shows high energy loss with an onset close to the surface band gap of the Ge(111)c(2×8) surface of 0.49 eV (marked by the vertical black dashed lines in Figure 2). We note that the value of the surface band gap was measured at a surface temperature of 30 K,³² whereas our measurements were performed at 300 K. Nevertheless, a similar, slightly lower, value of the surface band gap is expected at 300 K since the reconstruction of the surface remains the same. The H atom's low energy-loss channel was previously assigned to a mechanical interaction that can be described within an adiabatic model, whereas the high energy-loss channel is presumably formed by H atoms that induced electronic excitation of the surface.¹⁸

The two channels show different isotope effects. While the adiabatic channel shifts toward higher energy losses for deuterium, the high energy-loss channel shows no significant isotope effect. Also shown in Figure 2 are the ratios of the adiabatic to the nonadiabatic channel obtained at the specified experimental conditions. The branching ratio is nearly independent of isotopic substitution. For both isotopes, the nonadiabatic channel is strongly promoted by incidence translational energy.

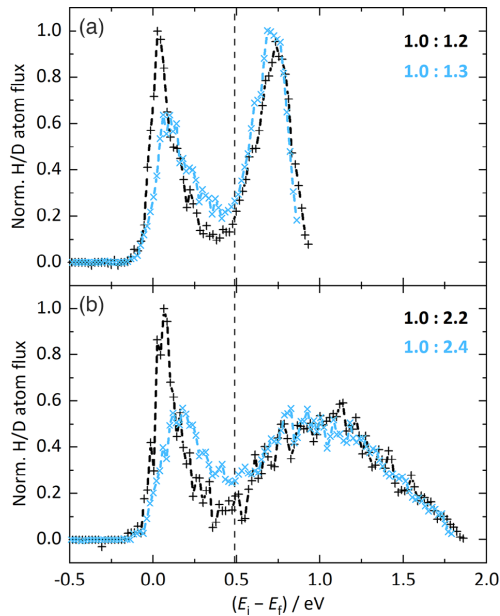


FIGURE 2 Experimental translational energy-loss distributions of H and D atoms scattered from Ge(111)c(2×8). The polar incidence and scattering angles θ_i and θ_f were both 45° and the incident atoms travel along the $[1\bar{1}0]$ surface direction. The surface temperature T_S was 300 K. Experimental data for the two isotopes are shown for translational incidence energies of $E_{i,H} = 0.99$ eV and $E_{i,D} = 0.94$ eV (a) as well as $E_{i,H} = 1.92$ eV and $E_{i,D} = 1.87$ eV (b) for H (black) and D (blue), respectively. The band gap of the surface is 0.49 eV and indicated by the vertical dashed line. The experimentally obtained ratio of the low energy-loss channel to the high energy-loss channel, separated by the value of the surface band gap, appears in each panel for both isotopes, H (black) and D (blue). All curves are normalized to the integrated signal.

Figure 3 shows the comparison of the experimental data to the results of electronically adiabatic MD simulations for H and D atoms scattered at the specular angle. The MD simulations reproduce the adiabatic channel for both isotopes quite well. Additionally, vertical dotted lines show the energy losses predicted by a line-of-centers binary collision model for both isotopes and incidence energies. These values are close to the peaks of the experimentally and theoretically obtained distributions. The observed isotope effect for the adiabatic channel is well reproduced by the MD simulations. For both H and D atom scattering, the high energy-loss feature is not accounted for by the adiabatic MD simulation.

In Figure 4, we present polar plots that show energy-resolved angular distributions of the scattered atoms. Experimental data (Figure 4a,b) are compared to the results of adiabatic MD simulations (Figure 4c,d). Incidence translational energies of $E_{i,H} = 0.99$ eV and $E_{i,D} = 0.94$ eV for H and D, respectively, were used. In Figure 4a,b, black dotted lines show the expected minimal energy loss for the exci-

tation of an electron across the band gap of the surface, separating the adiabatic channel from the nonadiabatic channel for scattered H and D atoms. The adiabatic channel shows a broad angular distribution. The nonadiabatic channel exhibits a narrower angular distribution than the adiabatic feature for both isotopes. Again, the ratio of the nonadiabatic channel to the adiabatic channel is only slightly larger for D compared to H. The results of MD simulations (Figure 4c,d) reproduce the broad angular distributions of the adiabatic channels, while the nonadiabatic channel is absent. In Figure 5, the data given in Figure 4 are further analyzed and direct comparisons of the angle-integrated translational energy loss and energy-integrated angular distributions are shown for both isotopes. The energy loss of the adiabatic channel is well reproduced by the MD simulations. The angular distributions of the adiabatic channel obtained from experiment and theory show slight differences but still compare fairly well. In this representation, the different angular distributions of the adiabatic and nonadiabatic channels are especially pronounced: the angular distribution of the nonadiabatic channel is narrower.

DISCUSSION

A bimodal energy-loss distribution is observed for both H and D atoms scattered from the semiconducting Ge(111)c(2×8) surface. Both scattering channels show distinct isotope effects. We will first discuss the isotope effect on the energy loss and the angular distribution of the adiabatic channel, followed by the isotope effect on the nonadiabatic channel and finally, we will discuss the isotope effect on the branching ratio between both channels. We focus on the scattering dynamics of the nonadiabatic channel that has not yet been characterized theoretically.

Figure 2 reveals a small isotope effect on the energy loss of the adiabatic channel that is reproduced by both the adiabatic MD simulations and a simple binary collision model, as shown in Figure 3. The amount of transferred energy is larger for D than for H. This can be attributed to the higher mass of the D atoms compared to H leading to a more efficient energy transfer during the mechanical interaction with the Ge surface atoms. As shown in Figures 4 and 5, the angular distributions are broad and similar for both isotopes and fairly well reproduced by MD simulations. Overall, the isotope effect of the adiabatic channel reflects the expectations for a mechanical interaction and confirms the prior interpretation.

The observed energy loss of the nonadiabatic channel is very similar for both isotopes, see Figure 2. The value of the surface band gap of Ge(111)c(2×8) seems to determine the onset of the energy-loss distribution for both isotopes. Also, the shape and the peak of the energy-loss distributions are nearly identical for both isotopes. This is somewhat surprising, since one might expect—for example, within an electronic friction picture—different EHP excitation spectra for the two isotopes, with a smaller EHP excitation probability for D atoms.⁸ Furthermore, the angular distributions of the nonadiabatic channel, which are considerably narrower than those of the adiabatic channel at 1 eV, are very similar for both isotopes, as shown in Figures 4 and 5.

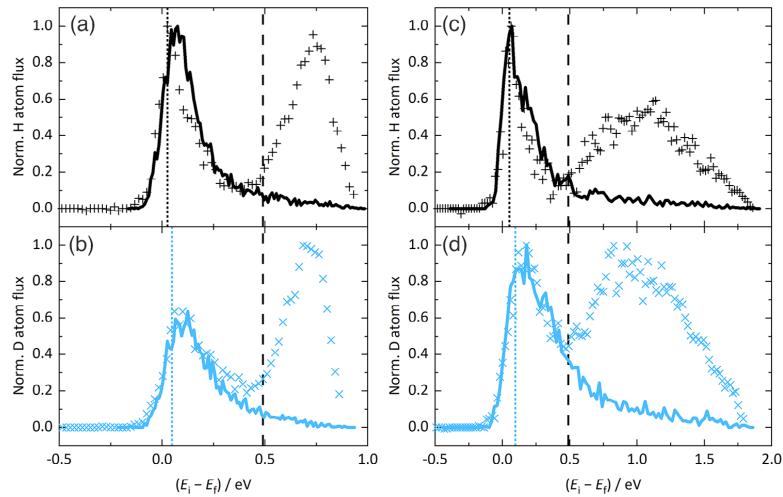


FIGURE 3 Comparison of experimental data to the results of adiabatic MD simulations for H and D atoms scattering from Ge(111)c(2×8) at the specular angle. Translational energy-loss distributions for H (black) and D (blue) atoms are shown for incidence translational energies of $E_{i,H} = 0.99$ eV (a) or $E_{i,H} = 1.92$ eV (c) and $E_{i,D} = 0.94$ eV (b) or $E_{i,D} = 1.87$ eV (d), respectively. The experimental conditions are the same as in Figure 2. Experimental data (+, x) are compared to the results of adiabatic MD simulations (solid lines). All experimental curves are normalized to the peak intensity. The MD curves are scaled to fit the adiabatic channel. The band gap of the surface is 0.49 eV and indicated by the vertical black dashed lines. Dotted lines represent the energy loss predicted by a line-of-centers binary collision model: $E_i - E_f = E_i \cos^2[(\theta_i + \theta_f)/2] \times [1 - (m_H - m_{Ge})^2 / (m_H + m_{Ge})^2]$.

Our observations suggest that the shape of the energy-loss distribution of the nonadiabatic channel is controlled by the density of states of the involved surface states. The narrow angular distribution could be caused by the fact that a specific surface site has to be hit in a certain geometry for an EHP excitation to occur.

The ratios of the nonadiabatic channel to the adiabatic channel are given in Figure 4a,b for both isotopes for incidence translational energies of about 1 eV. A similar branching ratio is observed for H and D, with a slightly stronger nonadiabatic channel for the heavier isotope. We want to highlight that the probability to initiate electronic excitation during a collision with the surface is nearly equal for H and D at a given incidence energy. From past work, one expects a smaller EHP excitation probability for deuterium. In chemcurrent experiments with Schottky diodes, for example, differences in EHP detection efficiency are observed for impinging H and D atoms.^{13–15} Such an isotope effect is clearly not seen in the current study, leading to the conclusion that the observed branching ratio cannot be determined by the probability to induce nonadiabatic processes. It has to be related to another property of the system. To understand this, we next consider the surface electronic structure.

The formally defined Ge(111) surface structure is highly unstable, as each atom of the first surface layer exhibits a dangling bond. This situation is remedied by the formation of a c(2×8) reconstructed surface shown in Figure 1. The surface consists of 0.25 monolayer adatoms (shown in red) each possessing a single dangling bond and bound to three saturated atoms of the first layer (shown in blue). Additional

dangling bonds are located at rest atoms in the first layer (shown in yellow). The surface is further stabilized by the transfer of one dangling bond electron from adatoms to rest atoms, which are present in equal quantities.³³ Also note that there are also second layer (shown in blue) and sublayer (shown in gray) tetravalent Ge atoms.

Figure 6 shows calculations of the electronic structure of the surface and how it is changed in the presence of an H atom. The left panel shows the calculated band structure of the pristine Ge(111)c(2×8) surface, whereas the other two panels show the band structures obtained for H adsorbed on a Ge adatom (middle panel) and on a Ge rest atom (right panel). Note that in Figure 6, red and blue colors are used to denote nondegenerate spin states, whereas green curves are used to denote degenerate spin states. We find that for the pristine surface, the highest occupied (valence band) surface state is doubly occupied and localized at rest atoms, whereas the lowest unoccupied (conduction band) surface state is localized at adatoms. It is, therefore, reasonable to assume that the promotion of an electron from the valence band to the conduction band via an H atom collision at the surface involves the transfer of an electron from a rest atom to an adatom. Figure 6 shows that H binding to a Ge rest atom results in a population of the previously unoccupied adatom surface state (bold red line in Figure 6), suggesting strongly that an H atom collision at a rest atom site can lead to electron transfer to an adatom site, promoting an electron from the valence to the conduction band. Hence, we hypothesize that when an H atom forms a 2-electron bond to a rest atom, the charge is simultaneously transferred back to an adatom, bringing the

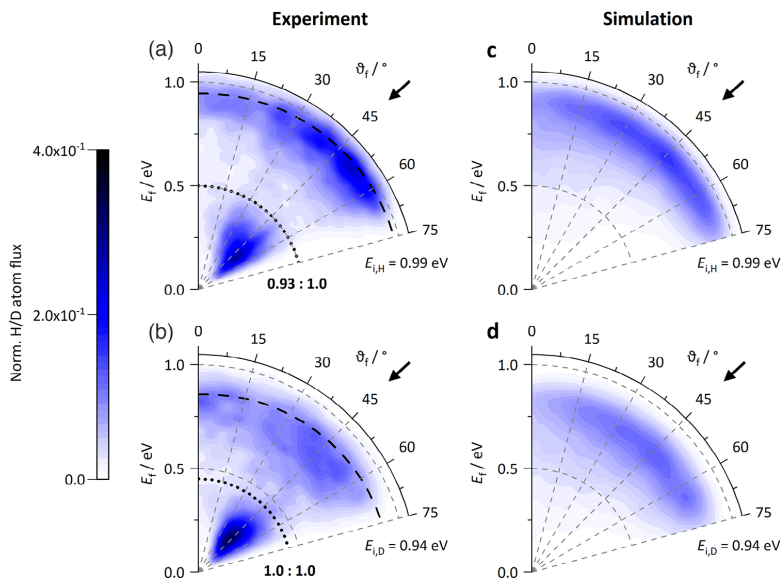


FIGURE 4 Energy-resolved angular distributions observed for H and D atom scattering from Ge(111)c(2×8). Distributions derived from in-plane scattering flux are shown for H (a & c) and D (b & d) atoms with incidence translational energies $E_{i,H} = 0.99$ eV (a & c) and $E_{i,D} = 0.94$ eV (b & d) at an incidence angle $\vartheta_i = 45^\circ$. Specular scattering angles are marked by black arrows. The surface temperature was $T_S = 300$ K. Experimental results (a & b) are compared to MD simulations (c & d). The MD simulations reproduce the behavior of the adiabatic channel only. To construct the experimental plots, data were recorded in 5° increments from $\vartheta_f = 0^\circ$ to 75° . Bold numbers show the ratios of the experimentally observed nonadiabatic channel (left) to the adiabatic channel (right). Each experimental distribution is normalized and the MD simulations are scaled to the respective experiment such that the integrated adiabatic channels are equal in both. The black dashed lines represent the final energy predicted by a line-of-centers binary collision model: $E_f = E_i \{1 - \cos^2[(\vartheta_i + \vartheta_f)/2] \times [1 - (m_H - m_{Ge})^2 / (m_H + m_{Ge})^2]\}$. The black dotted lines indicate the final energy of H and D atoms, respectively, that lost 0.49 eV during the interaction with the surface, corresponding to the value of the surface band gap.

previously unoccupied surface state below the Fermi level. Once the H atom again leaves the surfaces (a process requiring only ~ 25 fs), electron population remains in this adatom surface state, which once again belongs to the conduction band. This viewpoint can explain the lack of an isotope effect as electronic excitation probabilities are determined by the likelihood to hit a specific surface atom, which is equal for both isotopes.

The changes in electronic structure induced by an H atom collision can be more clearly seen in Figure 7. When H binds to the Ge adatom (Figure 7a), the previously unoccupied dangling bond now forms the H-Ge bond with the electron of hydrogen atom, borrowing electron density from nearby saturated Ge atoms. This leads to a drop of the Fermi energy. In contrast, Figure 7b shows the difference in charge density between the pristine surface and the surface with an H atom bonding to a rest atom. The calculations reveal that the additional electron is transferred to an adatom site.

H atom-induced electron transfer from rest to adatoms is also consistent with the results of scanning tunneling microscopy experiments, in which a charge transfer from the rest to the adatom upon H adsorption on the rest atom site was observed.^{34,35} As a consequence, the transferred electron fills the unoccupied adatom dangling bond band

originally in the conduction band, making it fall into the valence band. Interestingly, since there is only one additional electron, the drop of the energy level occurs only in one spin manifold. Note that in the case of an H atom binding at the adatom, no such charge transfer between ad and rest atoms is seen (see Figure 7a). Of course, electronically nonadiabatic dynamics calculations are needed. Nevertheless, the process just described could involve a crossing of electronic states during the collision of a hydrogen atom.

Site-specific scattering is also expected to produce a narrower angular distribution of the scattered H atoms. This might well explain why the electronically nonadiabatic channel exhibits a much narrower angular distribution than does the adiabatic one, which is not site-specific. Scattering from each of the surface sites contributes to the shape of the overall angular distribution. The potential, geometry, energy transfer, and sticking probability may differ for different surface sites, all of which will affect the contribution of one site to the overall angular distribution. While adiabatic MD simulations are not capable of reproducing the observed angular distributions, we can nevertheless analyze whether the angular distributions depend strongly on the scattering site. Such an analysis shows that the angular distribution of H atoms scattered from the adatom site shows the best agreement

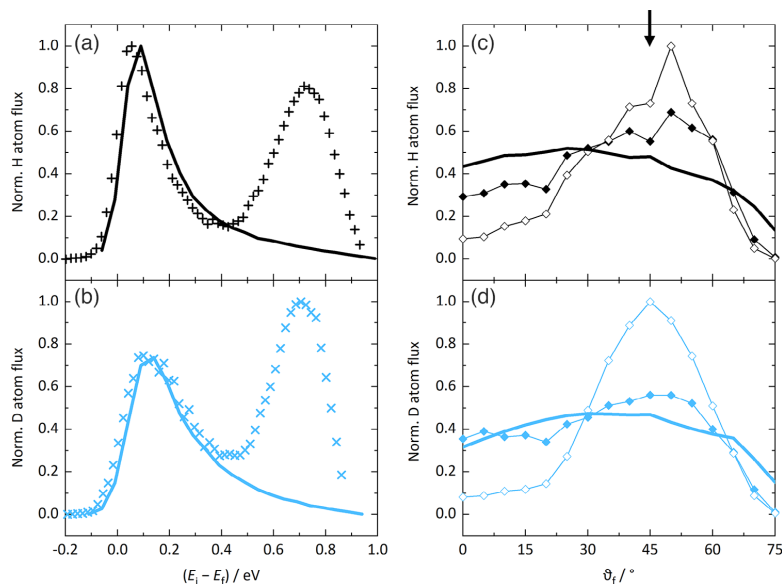


FIGURE 5 Comparison of energy loss and angular distributions for H and D atoms scattering from Ge(111)c(2x8). Angle-integrated translational energy-loss distributions (a & b) and energy-integrated angular distributions (c & d) derived from data given in Figure 4 are shown for H (a & c) and D (b & d) atoms with incidence translational energies $E_{i,H} = 0.99 \text{ eV}$ (a & c) and $E_{i,D} = 0.94 \text{ eV}$ (b & d) at an incidence angle $\vartheta_i = 45^\circ$. All other experimental conditions are the same as in Figure 4. To construct the angle-integrated energy-loss distributions, angle-resolved energy-loss distributions recorded in 5° increments from $\vartheta_f = 0^\circ$ to 75° , given in Figure 4, were summed up. The curves are further normalized to the peak intensity of the experimental data. To construct the energy-integrated angular distributions, the energy-loss distribution at each scattering angle was summed up in energy space; however, in the case of the experimental data, divided into the adiabatic channel (filled diamonds) and the nonadiabatic channel (open diamonds), separated by the surface band gap. The curves are normalized to the peak intensity of the nonadiabatic channel. The results from MD simulations are shown by solid lines. The specular scattering angle is marked by an arrow at the top of panel c.

with the observed angular distribution of the adiabatic channel. However, scattering from all surface sites exhibited rather broad angular distributions, and only small site-dependent differences are seen.

For both isotopes, the nonadiabatic channel is strongly promoted by incidence translational energy, as shown in Figure 2. Three factors have to be considered within the context of this observation. First, higher energy means higher speed which is known to promote nonadiabatic effects. However, since we see nearly no isotope effect on the branching ratio, we also do not expect a large effect due to an increased speed of the atoms. Second, higher translational energies make additional interband transitions energetically possible.³³ Additional transitions, which might not be constrained to certain surface sites, become accessible. The broadening of the angular distributions when going from 1 to 2 eV incidence energy (see Ref. 18 for H) is consistent with this interpretation. Third, the incidence energy dependence of the sticking probability can be expected to be different for both scattering channels and thus for different surface sites. As shown in Ref. 18, more integrated signal is observed for higher incidence energies, meaning that the sticking probability decreases with increasing incidence energy. Additionally, it was observed that the difference in signal is mainly due

to the nonadiabatic channel. Overall, the change of the branching ratio with increasing incidence translational energy—promoting the nonadiabatic channel—appears to be due to additional interband excitations that become accessible combined with a reduced sticking probability mainly attributed to the nonadiabatic channel.

As mentioned above, a quantitative theoretical model, capable of describing the experimental observations, is still lacking. An earlier attempt to use an electronic friction model failed to capture the bimodal energy-loss distributions,¹⁸ underscoring the inadequacy of the perturbative treatment of nonadiabatic transitions. Nevertheless, the evidence presented in this paper strongly suggests a site-specific process is responsible for the nonadiabatic excitation of electrons from the valence band to the conduction band. Specifically, we envision that as the H/D atom approaches the Ge surface, its high speed causes a strong perturbation of the local electronic structure at the impact site, which leads to a mixing of occupied and unoccupied surface states. The mixing enables the population of states lying above the surface band gap, converting the kinetic energy of the incident atom to electronic excitation. Finally, the atom is scattered from the surface with significant energy loss.

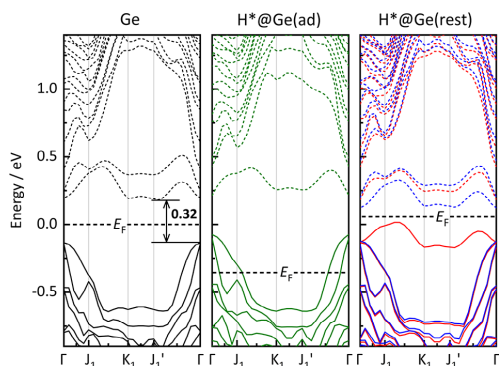


FIGURE 6 Change of band structures of Ge(111)c(2×8) upon H adsorption on different surface sites. Comparison of band structures of the Ge(111)c(2×8) surface (Ge, left), H adsorbing on the Ge adatom (H*@Ge(ad), middle), and on the Ge rest atom (H*@Ge(rest), right). Horizontal black dashed lines represent the Fermi level in different cases on the same energy scale. The calculated band gap of Ge(111)c(2×8) between conduction (dashed line) and valence band (solid line) is marked in the left panel by a vertical arrow (in eV). Spin-up and spin-down band structures are identical for the Ge and H*@Ge(ad) cases, but not for the H*@Ge(rest) case and thus shown in blue and red, respectively. Note that H adsorption on the adatom only results in a downward shift of the Fermi level, while on the rest atom, H atom adsorption causes a flip of one energy level from the conduction band to valence band (bold red).

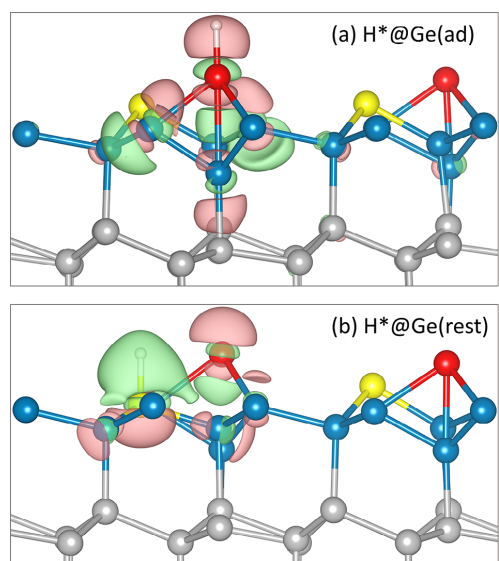


FIGURE 7 Differential charge density. Charge density of H*@Ge(ad) (a) and H*@Ge(rest) (b) minus that of the pristine Ge surface. Net charge gain is shown in pink and loss in green. The iso-surface value is $0.005 \text{ eV}/\text{\AA}^3$. Red, yellow, blue, and gray balls represent adatoms, rest atoms, saturated atoms, and sublayer atoms, respectively, the same as in Figure 1.

CONCLUSIONS

In summary, we used experimental data and results of electronically adiabatic MD simulations to investigate inelastic D atom scattering from Ge(111)c(2×8) and to study the isotope effect by comparing D to H atom scattering. The results confirm the existence of two channels that show fundamentally different scattering mechanisms: D and H atoms can either experience a mechanical interaction with the surface well described within the Born–Oppenheimer approximation (BOA) or a nonadiabatic interaction leading to electronic excitation across the surface band gap. To fully describe the experimentally observed energy loss and to understand the dynamics in detail, MD simulations beyond the limits of the BOA will be needed in the future. However, based on the observed branching between both scattering channels, which is only marginally influenced by isotopic substitution, we propose a surface site-specific energy transfer mechanism, which is supported by the change of the electronic band structure upon H adsorption at different surface sites. The experimental observations presented here pose a challenge to theory in providing a quantitative characterization of the nonadiabatic dynamics involving the excitation of EHPs across the semiconductor band gap.

AUTHOR CONTRIBUTIONS

A.M.W. and O.B. conceived the project. O.B. supervised the experiment and B.J. and H.G. supervised the theoretical simulations. K.K. performed the experiments. L.Z. and Y.W. performed the simulations. K.K. and Y.W. analyzed the data. K.K. and O.B. wrote the manuscript with feedback from A.M.W., L.Z., Y.W., B.J., and H.G.

ACKNOWLEDGMENTS

We thank Alexander Kandratsenka for the helpful discussions. O.B. and A.M.W. acknowledge support from the Deutsche Forschungsgemeinschaft (DFG) under SFB 1073, project A04 (217133147), and from the DFG, the Ministerium für Wissenschaft und Kultur, Niedersachsen, and the Volkswagenstiftung under grant number INST 186/902-1. H.G. acknowledges support from the National Science Foundation under grant nos. CHE-1951328 and CHE-2306975. B.J. acknowledges support from the K. C. Wong Education Foundation under grant number GJTD-2020-15. A.M.W. and H.G. acknowledge support from the Alexander von Humboldt Foundation. A.M.W. thanks the Max Planck Society for the Advancement of Science. B.J. thanks Dr. Wei Hu for the helpful discussion on band structure calculations.

Open access funding enabled and organized by Projekt DEAL.

CONFLICT OF INTEREST STATEMENT

The authors declare no conflict of interest.

DATA AVAILABILITY STATEMENT

The data that support the findings of this study are available from the corresponding author upon reasonable request.

ORCID

Kerstin Krüger  <https://orcid.org/0000-0002-5826-2674>

Bin Jiang  <https://orcid.org/0000-0003-2696-5436>

Hua Guo  <https://orcid.org/0000-0001-9901-053X>

Alec M. Wodtke  <https://orcid.org/0000-0002-6509-2183>

Oliver Bünermann  <https://orcid.org/0000-0001-9837-6548>

PEER REVIEW

The peer review history for this article is available at <https://www.webofscience.com/api/gateway/wos/peer-review/10.1002/ntls.20230019>

ETHICS STATEMENT

The authors confirm that they have followed the ethical policies of the journal.

REFERENCES

1. Rettner CT. Dynamics of the direct reaction of hydrogen-atoms adsorbed on Cu(111) with hydrogen-atoms incident from the gas-phase. *Phys Rev Lett.* 1992;69(2):383-386.
2. Rettner CT, Auerbach DJ. Quantum-state distributions for the HD product of the direct reaction of H(D)/Cu(111) with D(H) incident from the gas phase. *J Chem Phys.* 1996;104(7):2732-2739.
3. McMaster MC, Madix RJ. Kinetic isotope effect in direct ethane dissociation on Pt(111). *Surf Sci.* 1993;294(3):420-428.
4. Nesbitt A, Harder R, Golichowski A, Herrmann G, Snowdon KJ. Isotope effects in the dissociation dynamics of energetic hydrogen scattered from Cu(111) under glancing angles of incidence. *Chem Phys.* 1994;179(2):215-226.
5. Nienhaus H, Bergh HS, Gergen B, Majumdar A, Weinberg WH, McFarland EW. Electron-hole pair creation at Ag and Cu surfaces by adsorption of atomic hydrogen and deuterium. *Phys Rev Lett.* 1999;82(2):446-449.
6. Romm L, Citri O, Kosloff R, Asscher M. A remarkable heavy atom isotope effect in the dissociative chemisorption of nitrogen on Ru(001). *J Chem Phys.* 2000;112(19):8221-8224.
7. Bondarchuk O, Kim YK, White JM, Kim J, Kay BD, Dohnalek Z. Surface chemistry of 2-propanol on TiO₂(110): low- and high-temperature dehydration, isotope effects, and influence of local surface structure. *J Phys Chem C.* 2007;111(29):11059-11067.
8. Kandratenka A, Jiang HY, Dorenkamp Y, et al. Unified description of H-atom-induced chemisorption and inelastic scattering. *Proc Natl Acad Sci U S A.* 2018;115(4):680-684.
9. Kaufmann S, Shuai Q, Auerbach DJ, Schwarzer D, Wodtke AM. Associative desorption of hydrogen isotopologues from copper surfaces: characterization of two reaction mechanisms. *J Chem Phys.* 2018;148(19):194703.
10. Dorenkamp Y, Volkmann C, Roddatis V, Schneider S, Wodtke AM, Bünermann O. Inelastic H atom scattering from ultrathin aluminum oxide films grown by atomic layer deposition on Pt(111). *J Phys Chem C.* 2018;122(18):10096-10102.
11. Head-Gordon M, Tully JC. Molecular dynamics with electronic frictions. *J Chem Phys.* 1995;103(23):10137-10145.
12. Nienhaus H. Electronic excitations by chemical reactions on metal surfaces. *Surf Sci Rep.* 2002;45(1-2):3-78.
13. Krix D, Nunthel R, Nienhaus H. Generation of hot charge carriers by adsorption of hydrogen and deuterium atoms on a silver surface. *Phys Rev B.* 2007;75(7):073410.
14. Mildner B, Hasselbrink E, Dising D. Electronic excitations induced by surface reactions of H and D on gold. *Chem Phys Lett.* 2006;432(1-3):133-138.
15. Schindler B, Dising D, Hasselbrink E. Electronic excitations induced by hydrogen surface chemical reactions on gold. *J Chem Phys.* 2011;134(3):034705.
16. Dorenkamp Y, Jiang HY, Kockert H, et al. Hydrogen collisions with transition metal surfaces: universal electronically nonadiabatic adsorption. *J Chem Phys.* 2018;148(3):034706.
17. Jiang HY, Dorenkamp Y, Krüger K, Bünermann O. Inelastic H and D atom scattering from Au(111) as benchmark for theory. *J Chem Phys.* 2019;150(18):184105.
18. Krüger K, Wang Y, Tödter S, et al. Hydrogen atom collisions with a semiconductor efficiently promote electrons to the conduction band. *Nat Chem.* 2023;15(3):326-331.
19. Alducin M, Diez Muiño R, Juaristi JI. Non-adiabatic effects in elementary reaction processes at metal surfaces. *Prog Surf Sci.* 2017;92(4):317-340.
20. Bünermann O, Kandratenka A, Wodtke AM. Inelastic scattering of H atoms from surfaces. *J Phys Chem A.* 2021;125(15):3059-3076.
21. Bünermann O, Jiang HY, Dorenkamp Y, Auerbach DJ, Wodtke AM. An ultrahigh vacuum apparatus for H atom scattering from surfaces. *Rev Sci Instrum.* 2018;89(9):094101.
22. Schnieder L, Seekamprahn K, Liedeker F, Steuwe H, Welge KH. Hydrogen-exchange reaction H + D₂ in crossed beams. *Faraday Discuss.* 1991;91:259-269.
23. Weast RC. *CRC Handbook of Chemistry and Physics.* CRC Press; 1987.
24. Perdew JP, Burke K, Ernzerhof M. Generalized gradient approximation made simple. *Phys Rev Lett.* 1996;77(18):3865-3868.
25. Blöchl PE. Projector augmented-wave method. *Phys Rev B.* 1994;50(24):17953-17979.
26. Smith PV, Radny MW, Shah GA. Density functional study of the Ge(111)c(2×8) surface using the modified Becke-Johnson exchange potential with LDA correlation and spin-orbit interactions. *RSC Adv.* 2014;4(89):48245-48253.
27. Kresse G, Furthmüller J. Efficient iterative schemes for ab initio total-energy calculations using a plane-wave basis set. *Phys Rev B.* 1996;54(16):11169-11186.
28. Kresse G, Furthmüller J. Efficiency of ab-initio total energy calculations for metals and semiconductors using a plane-wave basis set. *Comput Mater Sci.* 1996;6(1):15-50.
29. Sun J, Haunschild R, Xiao B, Bulik IW, Scuseria GE, Perdew JP. Semilocal and hybrid meta-generalized gradient approximations based on the understanding of the kinetic-energy-density dependence. *J Chem Phys.* 2013;138(4):044113.
30. Krukau AV, Vydrov OA, Izmaylov AF, Scuseria GE. Influence of the exchange screening parameter on the performance of screened hybrid functionals. *J Chem Phys.* 2006;125(22):224106.
31. Wang V, Xu N, Liu J-C, Tang G, Geng W-T. VASPKIT: a user-friendly interface facilitating high-throughput computing and analysis using VASP code. *Comput Phys Commun.* 2021;267:108033.
32. Feenstra RM, Lee JY, Kang MH, Meyer G, Rieder KH. Band gap of the Ge(111)c(2×8) surface by scanning tunneling spectroscopy. *Phys Rev B.* 2006;73(3):035310.
33. Razado-Colambo I, He JP, Zhang HM, Hansson GV, Uhrberg RIG. Electronic structure of Ge(111)c(2×8): STM, angle-resolved photoemission, and theory. *Phys Rev B.* 2009;79(20):205410.
34. Klitsner T, Nelson JS. Site-specific hydrogen reactivity and reverse charge-transfer on Ge(111)-c(2×8). *Phys Rev Lett.* 1991;67(27):3800-3803.
35. Razado IC, Zhang HM, Hansson GV, Uhrberg RIG. Hydrogen-induced metallization on Ge(111) c(2×8). *Appl Surf Sci.* 2006;252(15):5300-5303.

How to cite this article: Krüger K, Wang Y, Zhu L, et al. Isotope effect suggests site-specific nonadiabaticity on Ge(111)c(2×8). *Nat Sci.* 2023;e20230019. <https://doi.org/10.1002/ntls.20230019>

4.3 The influence of surface temperature

Section 4.3 is comprised of a draft manuscript titled "*Inelastic H atom scattering as a probe for the surface electronic structure of Ge(111)*".

In this work, the influence of surface temperature on the energy-loss of H atoms scattered from Ge(111) is investigated. With increasing surface temperature, the energy-loss distributions drastically change, reflecting a continuous change of the surface electronic structure towards metallicity. The distributions are quantitatively decomposed into temperature-dependent contributions from an insulator, a metal and a semiconductor component. Furthermore, this work demonstrates the potential of inelastic H atom scattering as a method to probe the electronic structures of surfaces, while exhibiting exceptional surface sensitivity.

The manuscript is Ref. [152] in this thesis:

[152] K. Krüger, N. Hertl, A. M. Wodtke, O. Bünermann, Inelastic H atom scattering as a probe for the surface electronic structure of Ge(111), **2023**, (in preparation).

Author contributions:

K.K. performed the experiments and analyzed the data. N.H. performed the MD simulations. O.B. and K.K. wrote the manuscript with feedback from A.M.W. and N.H.

Inelastic H atom scattering as a probe for the surface electronic structure of Ge(111)

Kerstin Krüger¹, Nils Hertl^{2,4}, Alec M. Wodtke^{1,2,3}, Oliver Bünermann^{1,2,3,*}

¹ Institute of Physical Chemistry, Georg-August University, Göttingen, Germany.

² Department of Dynamics at Surfaces, Max-Planck-Institute for Multidisciplinary Sciences, Göttingen, Germany.

³ International Center of Advanced Studies of Energy Conversion, Georg-August University, Göttingen, Germany.

⁴ Present address: Department of Chemistry, University of Warwick, Coventry, United Kingdom.

* Corresponding author. E-mail: oliver.buenermann@chemie.uni-goettingen.de

Abstract

Measuring the surface electronic structure of materials is an experimental challenge. In this work, we introduce inelastic H atom scattering as a tool to probe the electronic structures of surfaces, which can be applied to both conducting and non-conducting samples while exhibiting exceptional surface sensitivity. We illustrate the method for the example of Ge(111) and observe three temperature-dependent contributions to the H atom inelasticity, representing insulating, semiconducting and metallic behavior.

Introduction

In the past, a variety of methods have been devised to characterize the bulk electronic properties of semiconductor materials. For example, optical absorption edge spectroscopy provides semiconductor band gaps ^[1–3] and photoelectron spectroscopy (PES) became one of the most powerful tools to probe the bulk electronic states of solids ^[4–6]. Surface properties, however, can differ significantly from bulk characteristics. The famous Si(111)(7 × 7) surface, for instance, is metallic due to a partially filled surface state ^[7], while Si is a bulk semiconductor.

The methods currently available, many of which are based on photo-absorption, are limited when probing surface electronic states. PES is not, strictly speaking, surface selective as photoelectrons originating from several atomic layers below the surface contribute to the signals. PES spectra therefore include information about bulk and surface states ^[4] and distinguishing between them can be a challenge. Furthermore, conventional PES is sensitive only to occupied electronic states. In order to avoid the use of photons, metastable atoms can be used to generate exo-electrons ^[8] and enhanced surface sensitivity is achieved. Electron energy loss spectroscopy (EELS) is another alternative and, while mainly used to study surface phonons and adsorbate vibrations ^[9], can be used to study electronic surface states ^[10]. When low energy incidence electrons are used, it is indeed more surface sensitive than PES. Unfortunately, it can be difficult to remove the influence of near elastic electron scattering, which often dominates the spectrum in the area of interest ^[11]. Scanning tunneling spectroscopy (STS) is another approach to obtaining information about electronic surface states ^[12], even providing in favorable cases the spatial properties of the surface states. However, the strong electric fields near the tip can alter the material’s electronic states, a complicating effect referred to as tip induced band-bending ^[13]. We note that all of these methods are limited to analysis of conducting materials.

In this work, we apply an entirely different concept where the detected particle is not an electron. Instead, neutral beams of monochromatic H atoms are scattered from the surface of the sample and the measured translational inelasticity becomes a probe of the surface electronic structure. H atom scattering offers the advantage of being exquisitely surface specific; this is due to the fact that H atoms that penetrate the surface are, for all practical purposes, guaranteed to remain adsorbed at or below the surface ^[14,15]. Furthermore, exchange of H atom translational energy with the solid is strongly sensitive to the electronic structure of the surface, exhibiting qualitatively different behavior for insulators, metals and semiconductor surfaces ^[14–17]. Another remarkable feature arises from the fact that H atoms are uncharged; hence, this approach is equally applicable

4 Hydrogen atom scattering from germanium surfaces

to non-conductive materials. Finally, because the method explicitly involves electronic transitions, information about both occupied and unoccupied electronic states can be obtained.

We illustrate this approach applied to a study of the temperature-dependence of the electronic structure of a semiconductor surface. At room temperature, Ge(111) exhibits a stable $c(2 \times 8)$ adatom surface reconstruction [18], the atomic geometry of which influences the nature of surface electronic states and leads to surface semiconducting behavior [19–21]. As the temperature increases, the surface structure changes and at 573 K, the entire surface exhibits a disordered adatom arrangement, characterized by an apparent “ (1×1) ” diffraction pattern [22–24]. A second reversible transition is observed around 1050 K [25–27]. Previous work suggests that a gradual metallization of the surface starting at about 600 K and increasing with temperature results in full surface metallization at 1050 K [28,29]. When using inelastic H atom scattering to follow the temperature-dependent electronic structure of the Ge(111) surface between 140 and 950 K, we find three distinct components in the energy-loss distribution that can be assigned to insulator, semiconductor and metal behavior. The relative quantitative contribution of these three components can be easily determined. H atom scattering therefore represents a valuable approach to obtaining the basic physical properties of a surface with complex electronic structure.

Experimental Methods

The H atom scattering apparatus has been described in detail [17,30]. In short, a hydrogen atom beam with an incidence translational energy of $E_i = 0.99$ eV is formed by ultraviolet photodissociation of a supersonic molecular beam of hydrogen iodide using an excimer laser operating at 248 nm. A small portion of the H atoms passes through a skimmer and two differential pumping apertures, enters an ultra-high vacuum (UHV) chamber and collides with a Ge crystal. The Ge sample is mounted on a five-axis manipulator, which allows the variation of the polar incidence angle ϑ_i with respect to the surface normal. The scattered H atoms are detected using Rydberg atom tagging time-of-flight (RAT-TOF) [31]. Here, the H atoms are excited to a long-lived Rydberg state just below the ionization limit and fly 250 mm, before they are field-ionized and detected by a multichannel plate (MCP) assembly. The detector is rotatable, enabling TOF distribution measurements at a variety of scattering angles ϑ_f . A multichannel scaler records the arrival time distribution. The time-of-flight distribution is converted to an energy-loss distribution applying the appropriate Jacobians. The surface temperature T_S can be adjusted between 130 K and 950 K using a liquid nitrogen flow cryostat com-

bined with resistive heating. The temperature of the crystal was measured by a K-type thermocouple; temperatures above 450 K were calibrated using an external pyrometer. The Ge crystal used in this work was undoped, with a nominal purity of 99.999%. The Ge(111) surface was cleaned by cycles of Ar⁺ ion sputtering and annealing at ≈ 950 K. Auger electron spectroscopy (AES) and low-energy electron diffraction (LEED) were used to validate the cleanliness and $c(2 \times 8)$ structure of the room temperature Ge(111) surface prior to experiments. We ensured that the energy-loss distributions did not change during the course of a measurement, to exclude any influence of the build-up of H coverage or other contaminations on the surface of the Ge(111) crystal during the measurement.

Results

Figure 4.1 shows translational energy-loss distributions of H atoms scattered from a Ge(111) surface at surface temperatures of $138 \text{ K} < T_S < 942 \text{ K}$. At 138 K, two well-separated features are visible. These features have been previously assigned to an electronically adiabatic scattering process at low energy-losses, reflecting insulator behavior, and an electronically non-adiabatic process at high energy-losses, where an electron is promoted from the valence band to the conduction band (VB-CB transition) of the surface reflecting its semiconducting nature [16]. With increasing T_S , the intensity of these two features decreases and H atom flux at intermediate energy-losses becomes increasingly apparent. In addition, the VB-CB transition shifts to lower energy as T_S increases. At $T_S = 942 \text{ K}$, the bimodal structure has vanished and a broad, nearly featureless energy-loss distribution arises.

This energy-loss distribution is remarkably similar to those obtained for H atom scattering from metal surfaces [32]; consistent with previous work, this suggests that the surface of Ge(111) is metallic at high temperatures. To test this idea, we performed full dimensional theoretical simulations of the H atom scattering from a copper surface using molecular dynamics with electronic friction (MDEF), which has been shown to accurately describe experimentally obtained H atom energy-loss distributions for metals [32,33]. We chose copper as its mass (63.5 u) is close to that of germanium (72.6 u); hence, the mechanical contributions to the H atom energy-loss are similar in the two cases [34]. Details of the MDEF calculations appear in the SI.

Figure 4.2 shows that the H atom energy-loss distribution obtained with Ge(111) at $T_S = 942 \text{ K}$ is nearly identical to the MDEF simulations of H scattering from Cu at a similar surface temperature. This strongly supports the hypothesis that the Ge(111) surface is at least partially metallic at high temperature, whereas it exhibits both insu-

4 Hydrogen atom scattering from germanium surfaces

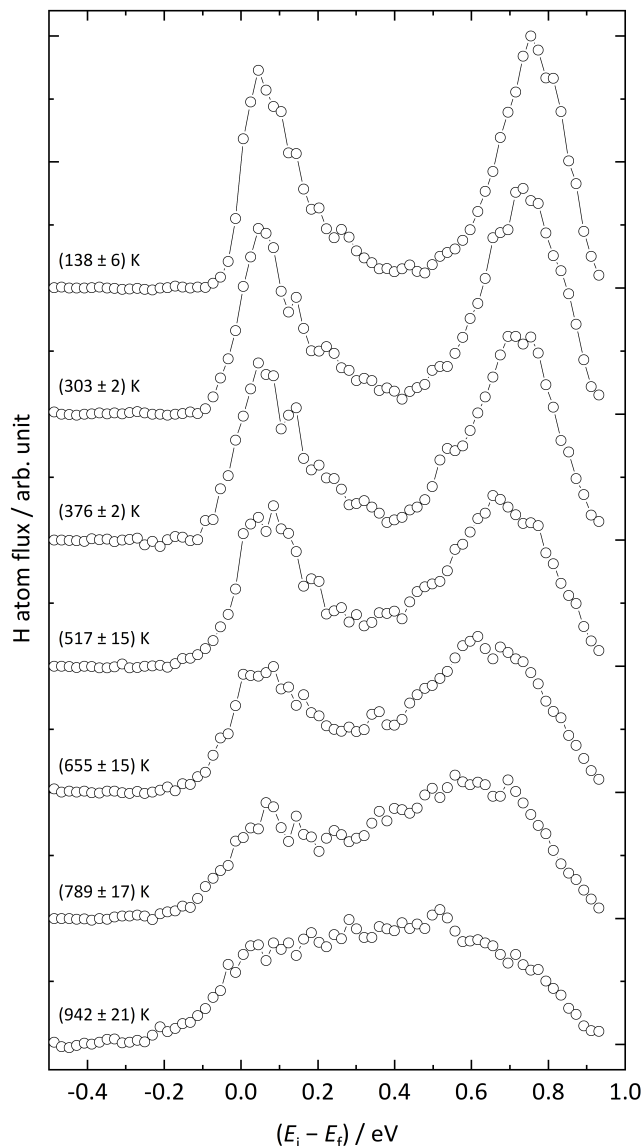


Figure 4.1: Temperature-dependent energy-loss distributions for H atoms scattered from a Ge(111) surface. The polar incidence ϑ_i and scattering ϑ_f angles are both 45° . The energy-loss distributions are normalized to the integrated signal. The incident H atoms have a translational energy of $E_i = 0.99$ eV and travel along the $[\bar{1}10]$ surface direction.

lator and semiconductor behavior at low T_S .

To treat this quantitatively, the energy-loss distributions of Fig. 4.1 were fitted to a three component model – see Fig. 4.3. First, the bimodal energy-loss distribution obtained at $T_S = 138$ K (Fig. 4.3 a) provides two well-resolved features that were separately fitted by a sum of Gaussian functions. In the following, the fit function of the low energy-loss

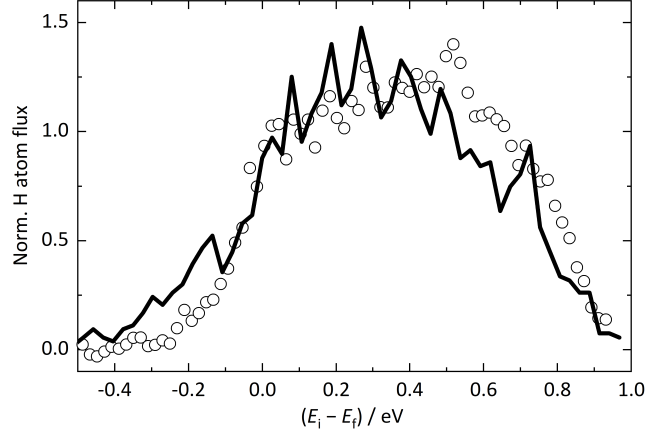


Figure 4.2: Partially metallized surface of Ge(111) at elevated surface temperature. Inelastic H atom scattering data for Ge(111) at $T_S = 942$ K (\circ) is compared to the results of MDEF simulations for Cu(111) at $T_S = 950$ K (black solid line). The H atoms travel along the $[10\bar{1}]$ direction of the Cu(111) surface. The energy-loss distributions are normalized to the integrated signal. Conditions are otherwise the same as in Fig. 4.1.

feature is referred to as insulator component and the VB-CB transition is denoted as the semiconductor component. To account for the broad and featureless component that evolves with increasing surface temperature, the results of MD simulations for Cu(111) at $T_S = 950$ K (Fig. 4.3 h) were used as a third "metallic" component. By varying the relative contributions of these three components, all six remaining energy-loss distributions could be fitted – see Fig. 4.3 b-g. The shape and position of the insulator and metal component were fixed, whereas the semiconductor component was allowed to broaden and shift with increasing T_S – this allows us to account for a reduction in the surface band gap with increasing surface temperature ^[29,35]. The three component model results in an excellent fit to the data.

Figure 4.4 shows the relative contribution of the three components vs. T_S . Both the insulator and semiconductor contributions decrease, while the metallic contribution increases with T_S and dominates above $T_S \approx 750$ K.

4 Hydrogen atom scattering from germanium surfaces

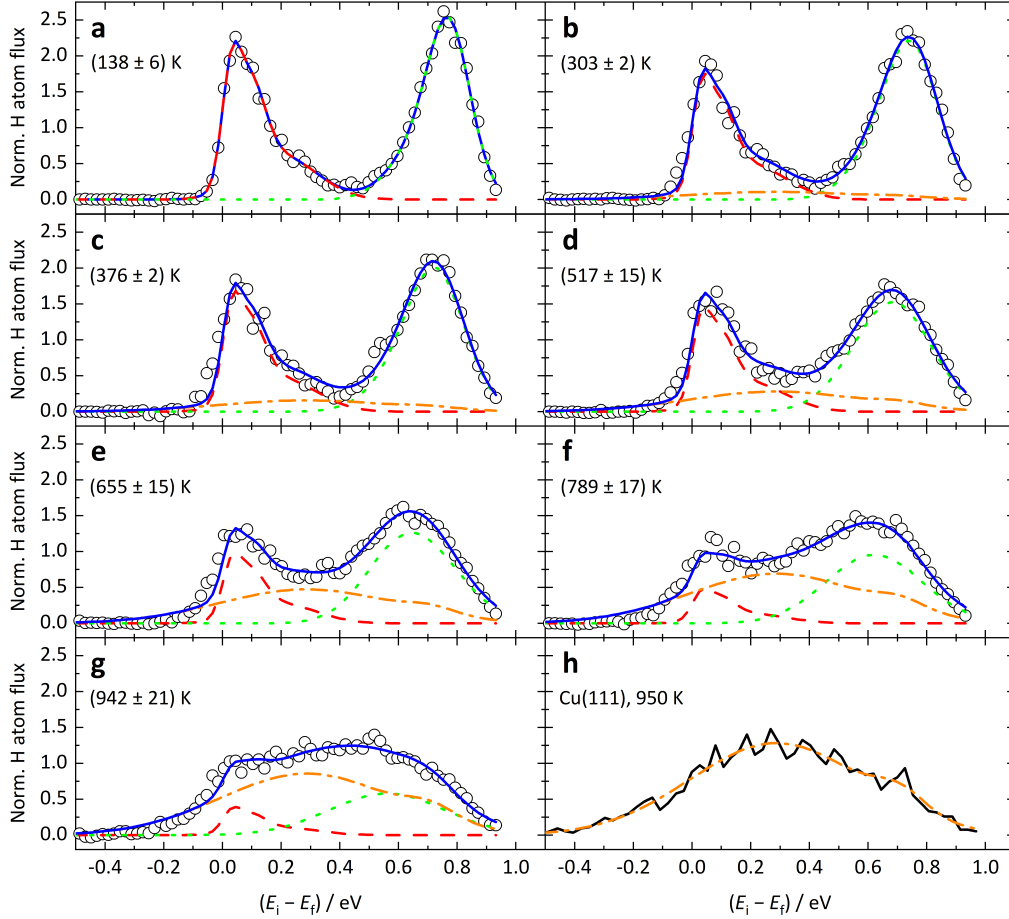


Figure 4.3: Fit of the energy-loss distributions for H atoms scattered from Ge(111) at different surface temperatures with three components. Panels a to g show a fit of the energy-loss distributions (\circ) of H atoms scattered from Ge(111) at different surface temperatures, T_S . The data was fitted to a sum of three components (blue solid line): an insulator (red dashed line), a semiconductor (green dotted line) and a metal (orange dash-dotted line) component. Panel h shows the fit of the energy-loss distribution of H atoms scattered from Cu(111) at $T_S = 950$ K that is used as the metal component. Details about the fit can be found in the text. The incidence translational energy is $E_i = 0.99$ eV, the polar incidence and scattering angles are $\vartheta_i = \vartheta_f = 45^\circ$. The incident H atoms travel along the $[\bar{1}10]$ surface direction for Ge(111), and along the $[10\bar{1}]$ direction for Cu(111).

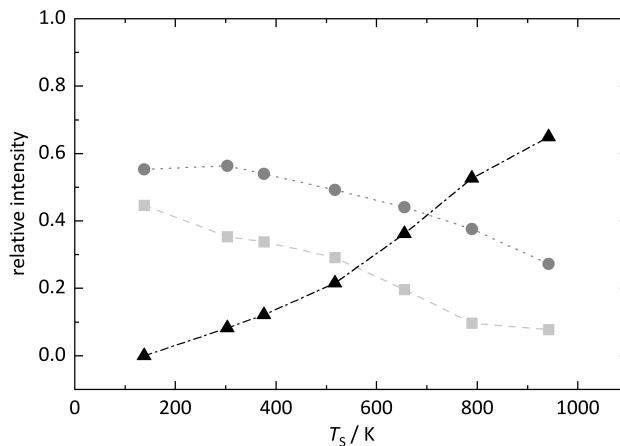


Figure 4.4: Electronic character of the Ge(111) surface as a function of surface temperature. The relative intensities are determined from the fits in Fig. 4.3 for the insulator component (■), the semiconductor component (●) and the metal component (▲). Lines between data points are given as a guide to the eye.

Discussion

The results of this work complement previous qualitative analyses using established methods such as LEED [22,23], PES [29,36–39], EELS [28,40] and STM [24]. LEED images from the room temperature semiconducting surface reflect its $c(2 \times 8)$ structure [19–21]. With increasing temperature, a structural transition [22] is revealed around 573 K as an apparent “ (1×1) ” diffraction pattern with weak half-order spots emerges that was attributed to the formation of an “incommensurate (2×2) surface structure” [23]. STM confirmed the coexistence of ordered and disordered regions at even lower temperatures – at 573 K, the entire surface was found to be disordered [24]. No abrupt changes in the electronic structure were observed in either PES [29,36,37] or EELS [40]. Instead it was suggested that a gradual metallization of the surface takes place [28,29,39]; a result that becomes evident in the energy-loss distributions obtained from inelastic H atom scattering, too. At low T_S , a bimodal energy-loss distribution is clearly seen reflecting the coexistence of insulating and semiconducting character. At elevated surface temperatures, the bimodality transforms to one broad energy-loss feature characteristic of a metallic surface. The relative importance of the three coexisting contributions – insulator, semiconductor and metal – can be easily quantified.

The physics of H atom inelasticity is quite different than that underlying established methods. Importantly, H atom energy-loss distributions can be quantitatively simulated for both insulating and metallic surfaces. In the case of metals, the partially filled

4 Hydrogen atom scattering from germanium surfaces

conduction band allows intraband excitations resulting in a very efficient transfer of H atom translational energy to electron-hole pair (EHP) excitation [14]. Classical MDEF simulations employing high dimensional potential energy surfaces derived from DFT data provide highly accurate energy-loss distributions [14,32–34,41]; here, the electronic friction picture is able to describe intraband EHP excitation induced by the H atom collision. In contrast, semiconductors and insulators have a band gap with occupied states below the Fermi energy and unoccupied states above the Fermi energy, only allowing interband excitations at low temperatures. In the case of insulators, the band gap is larger than the incidence translational energy of H atoms, making electronic interband excitations inaccessible so that energy can only be dissipated via phonon excitation. Thus, H atom collisions with insulators can be quantitatively reproduced by MD simulations within the Born-Oppenheimer approximation (BOA) [15,16]. In the case of semiconductors, H atoms with sufficient energy can excite electrons over the band gap [16] revealing interband excitations between occupied and unoccupied states. Based on the present work, we conclude that with increasing temperature, the surface conduction band becomes thermally occupied, which additionally allows intraband excitations in both the surface valence and conduction band. Thus, energetically low-lying EHP excitations – the predominant energy-loss channel in metal surfaces – become possible on semiconductor surfaces, giving rise to the metallic contribution to the surface electronic structure. Remarkably, the surface band gap’s reduction with increasing temperature [35] also becomes evident in the inelastic H atom scattering, an effect which leads to increased thermal occupation of the conduction band.

The H atom energy-loss distributions presented in this work show no abrupt change at any temperature. This reflects the co-existence of insulating, semiconducting and metallic character at the surface, whose respective contributions gradually change as a function of temperature. The detection of the coexistence of multiple material properties of the surface by the H atom scattering is straightforward as each H atom collision samples a different position on the surface and there is no intrinsic bias against any property. Furthermore, the analysis needed to extract this information is remarkably simple. Inelastic H atom scattering has great potential to give detailed insights into the electronic properties of surfaces.

Acknowledgments

We thank Alexander Kandratsenka, Yingqi Wang and Hua Guo for helpful discussions. O.B. and A.M.W. acknowledge support from the Deutsche Forschungsgemeinschaft (DFG) under SFB 1073 (217133147), project A04 and from the DFG, the Minis-

terium für Wissenschaft und Kultur, Niedersachsen and the Volkswagenstiftung under grant no. INST 186/902-1. A.M.W. thanks the Max Planck Society for the advancement of science.

Author Contributions

A.M.W. and O.B. conceived the project. O.B. supervised the experiment. K.K. performed the experiments. N.H. performed the MD simulations. K.K. analyzed the data. K.K. and O.B. wrote the manuscript with feedback from A.M.W. and N.H.

Competing Interests

The authors declare no competing interests.

Supplementary Information

Theoretical Methods

The calculations simulating H atom scattering from Cu(111) were performed in a similar way as in Ref. [33]. The potential energy surface on which the simulations were performed are based on Effective Medium Theory (EMT) [42–44] and the parameters characterizing the global H/Cu potential energy surface are taken from Ref. [45]. The Cu(111) surface was modeled as 6×6 slab with six layers with the bottom layer kept fixed. The initial slab configurations were acquired as follows: we thermalized an optimized 0 K copper slab to the desired temperature with the Andersen thermostat [46] and propagated it for 100 ps. Every 100 fs, a snapshot of the slab was taken which served as input geometry for the scattering simulations. The H atoms were placed 6 \AA above the surface with random x and y coordinates. The components of the projectile’s velocity vector were chosen so that the H atom possesses a kinetic energy of 0.99 eV and an incidence angle of 45° with respect to the surface normal. The crystallographic incidence direction corresponds to the $[10\bar{1}]$ direction. The propagation details of the H atom and the surface atoms are the same as in Ref. [33]. For the computation of the energy-loss distribution, we only used H atoms which scattered in-plane with a scattering angle of 45° and used a spherical angular tolerance of $\pm 5^\circ$ to mimic the circular detector geometry in the experiment. For each calculation set, we launched $3 \cdot 10^6$ trajectories with the intention to ensure proper numerical statistics. As shown in Fig. 4.5, the agreement between experiment and MD simulations including electronic friction is good at $T_S = 300 \text{ K}$ for H atom scattering from Cu(111).

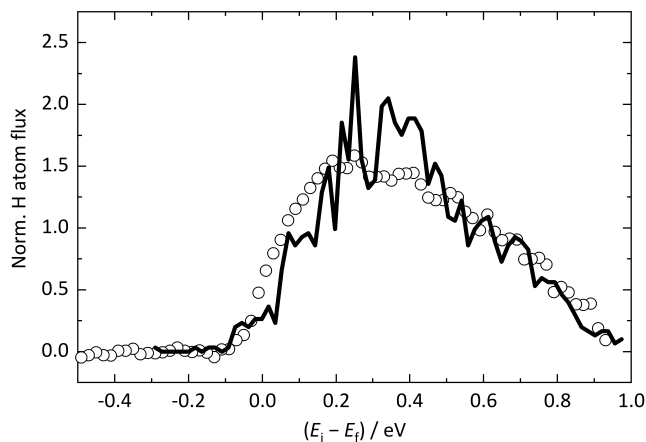


Figure 4.5: Comparison of energy-loss distributions from experiment and MD simulations for H atoms scattering from Cu(111) at $T_S = 300$ K. Experimental data (\circ) from Ref. [32] is compared to the results of molecular dynamics simulations including electronic friction (black solid line). The incidence translational energy of the H atoms is $E_i = 0.99$ eV and the incident H atoms travel along the $[10\bar{1}]$ surface direction. The polar incidence and scattering angles are $\vartheta_i = \vartheta_f = 45^\circ$. The distributions are normalized to their integrated intensity.

References

- [1] M. Becker and H. Y. Fan, Phys. Rev. **76**, 1531 (1949).
- [2] G. W. Gobeli and H. Y. Fan, Phys. Rev. **119**, 613 (1960).
- [3] R. Zallen and M. P. Moret, Solid State Commun. **137**, 154 (2006).
- [4] H. Y. Zhang, T. Pincelli, C. Jozwiak, T. Kondo, R. Ernstorfer, T. Sato, and S. Y. Zhou, Nat. Rev. Methods Primers **2**, 54 (2022).
- [5] G. Schoenhense and H. J. Elmers, J. Vac. Sci. Technol. A **40**, 020802 (2022).
- [6] J. A. Sobota, Y. He, and Z. X. Shen, Rev. Mod. Phys. **93**, 025006 (2021).
- [7] U. Backes and H. Ibach, Solid State Commun. **40**, 575 (1981).
- [8] S. Nannarone and L. Pasquali, Nucl. Instrum. Meth. B **182**, 227 (2001).
- [9] A. Politano, Phys. Chem. Chem. Phys. **23**, 26061 (2021).
- [10] M. Rocca, Surf. Sci. Rep. **22**, 1 (1995).
- [11] M. Stöger-Pollach, H. Franco, P. Schattschneider, S. Lazar, B. Schaffer, W. Grogger, and H. W. Zandbergen, Micron **37**, 396 (2006).

4.3 *The influence of surface temperature*

- [12] R. M. Feenstra, *Surf. Sci.* **299**, 965 (1994).
- [13] R. M. Feenstra, *Surf. Sci.* **603**, 2841 (2009).
- [14] O. Bünermann, H. Y. Jiang, Y. Dorenkamp, A. Kandratsenka, S. M. Janke, D. J. Auerbach, and A. M. Wodtke, *Science* **350**, 1346 (2015).
- [15] N. Hertl, A. Kandratsenka, O. Bünermann, and A. M. Wodtke, *J. Phys. Chem. A* **125**, 5745 (2021).
- [16] K. Krüger, Y. Wang, S. Tödter, F. Debbeler, A. Matveenko, N. Hertl, X. Zhou, B. Jiang, H. Guo, A. M. Wodtke, O. Bünermann, *Nat. Chem.* **15**, 326 (2023).
- [17] O. Bünermann, A. Kandratsenka, and A. M. Wodtke, *J. Phys. Chem. A* **125**, 3059 (2021).
- [18] D. J. Chadi and C. Chiang, *Phys. Rev. B* **23**, 1843 (1981).
- [19] R. S. Becker, B. S. Swartzentruber, J. S. Vickers, and T. Klitsner, *Phys. Rev. B* **39**, 1633 (1989).
- [20] F. J. Himpsel, *Surf. Sci. Rep.* **12**, 1 (1990).
- [21] R. M. Feenstra, J. Y. Lee, M. H. Kang, G. Meyer, and K. H. Rieder, *Phys. Rev. B* **73**, 035310 (2006).
- [22] P. W. Palmberg, *Surf. Sci.* **11**, 153 (1968).
- [23] R. J. Phaneuf and M. B. Webb, *Surf. Sci.* **164**, 167 (1985).
- [24] R. M. Feenstra, A. J. Slavin, G. A. Held, and M. A. Lutz, *Phys. Rev. Lett.* **66**, 3257 (1991).
- [25] E. G. McRae and R. A. Malic, *Phys. Rev. Lett.* **58**, 1437 (1987).
- [26] A. W. Denier van der Gon, J. M. Gay, J. W. M. Frenken, and J. F. van der Veen, *Surf. Sci.* **241**, 335 (1991).
- [27] C. A. Meli, E. F. Greene, G. Lange, and J. P. Toennies, *Phys. Rev. Lett.* **74**, 2054 (1995).
- [28] S. Modesti, V. R. Dhanak, M. Sancrotti, A. Santoni, B. N. J. Persson, and E. Tosatti, *Phys. Rev. Lett.* **73**, 1951 (1994).

4 Hydrogen atom scattering from germanium surfaces

- [29] A. Goldoni, A. Santoni, M. Sancrotti, V. R. Dhanak, and S. Modesti, *Surf. Sci.* **382**, 336 (1997).
- [30] O. Bünermann, H. Y. Jiang, Y. Dorenkamp, D. J. Auerbach, and A. M. Wodtke, *Rev. Sci. Instrum.* **89**, 094101 (2018).
- [31] L. Schnieder, K. Seekamprahn, F. Liedeker, H. Steuwe, and K. H. Welge, *Faraday Discuss.* **91**, 259 (1991).
- [32] Y. Dorenkamp, H. Y. Jiang, H. Kockert, N. Hertl, M. Kammler, S. M. Janke, A. Kandratsenka, A. M. Wodtke, and O. Bünermann, *J. Chem. Phys.* **148**, 034706 (2018).
- [33] N. Hertl, K. Krüger, and O. Bünermann, *Langmuir* **38**, 14162 (2022).
- [34] A. Kandratsenka, H. Y. Jiang, Y. Dorenkamp, S. M. Janke, M. Kammler, A. M. Wodtke, and O. Bünermann, *PNAS* **115**, 680 (2018).
- [35] J. E. Demuth, R. Imbihl, and W. A. Thompson, *Phys. Rev. B* **34**, 1330 (1986).
- [36] T. Yokotsuka, S. Kono, S. Suzuki, and T. Sagawa, *Jpn. J. Appl. Phys.* **23**, L69 (1984).
- [37] J. Aarts, A. Hoeven, and P. K. Larsen, *Phys. Rev. B* **38**, 3925 (1988).
- [38] K. Hricovini, G. Le Lay, M. Abraham, and J. E. Bonnet, *Phys. Rev. B* **41**, 1258 (1990).
- [39] L. Pasquali, S. Nannarone, M. Canepa, and L. Mattera, *Phys. Rev. B* **57**, 2507 (1998).
- [40] L. Pasquali, S. D'Addato, L. Tagliavini, A. M. Prandini, and S. Nannarone, *Surf. Sci.* **377-379**, 534 (1997).
- [41] H. Y. Jiang, Y. Dorenkamp, K. Krüger, and O. Bünermann, *J. Chem. Phys.* **150**, 184105 (2019).
- [42] K. W. Jacobsen, J. K. Norskov, and M. J. Puska, *Phys. Rev. B* **35**, 7423 (1987).
- [43] K. W. Jacobsen, P. Stoltze, and J. K. Norskov, *Surf. Sci.* **366**, 394 (1996).
- [44] N. Hertl, A. Kandratsenka, and A. M. Wodtke, *Phys. Chem. Chem. Phys.* **24**, 8738 (2022).

4.3 *The influence of surface temperature*

- [45] M. Kammler, S. M. Janke, A. Kandratsenka, and A. M. Wodtke, *Chem. Phys. Lett.* **683**, 286 (2017).
- [46] H. C. Andersen, *J. Chem. Phys.* **72**, 2384 (1980).

4 Hydrogen atom scattering from germanium surfaces

4.4 The influence of surface structure: Ge(100) vs. Ge(111)

This section presents H atom scattering from a Ge(100)(2×1) surface and compares the results to H atom scattering from Ge(111) $c(2 \times 8)$, as given in Refs. [150] and [152] in Sections 4.1 and 4.3, respectively. Energy-resolved angular distributions were measured for two incidence translational energies at room temperature. For H atoms scattered at the specular angle, the temperature dependence of the translational energy-loss distributions was additionally investigated.

Structural and electronic properties of Ge(100)

The Ge(100) surface shows especially complex structural and electronic properties, which are described in detail in Section 2.1. In short, (2×1)-type surface reconstructions are formed at room temperature that consist of rows of asymmetrically buckled dimers. Dimer rows on adjacent surface terraces, which are typically separated by single layer step edges, are rotated 90° to each other. Specifically, $p(2 \times 1)$, $p(2 \times 2)$ and $c(4 \times 2)$ structures are found to coexist on the Ge(100) surface, see also Fig. 2.4. Extremely clean and nearly defect-free Ge(100) surfaces consist of almost equally populated highly-ordered striped $c(4 \times 2)$ and $p(2 \times 1)$ domains. On surfaces with a higher concentration of defects, a more disordered structure with coexisting areas of $c(4 \times 2)$,

Table 4.1: Overview of surface reconstructions and band gaps of Ge(111) and Ge(100). The surface band gaps are given in Ref. [81] and [86] for Ge(111) and Ge(100), respectively. For Ge(100), both experimentally (exp.) and theoretically (th.) determined values of the surface band gaps are available. For details, the reader is referred to the main text and Section 2.1.

	Ge(111)		Ge(100)	
Surface reconstruction ^a	$c(2 \times 8)$	$p(2 \times 1)$	$c(4 \times 2)$	$p(2 \times 2)$
Surface band gap (exp.) / eV	0.49		0.2 ^b	
Surface band gap (th.) / eV		0.5	0.15	^c

a: Reconstructions present on annealed surfaces are considered only.

b: The band gap was determined on a Ge(100) surface with a highly-ordered $c(4 \times 2)/(2 \times 1)$ structure.

c: No value for the surface band gap of Ge(100) $p(2 \times 2)$ is given in Ref. [86], but the electronic properties of the $p(2 \times 2)$ reconstruction are described to be essentially identical to the $c(4 \times 2)$ surface.

$p(2 \times 2)$ and $p(2 \times 1)$ domains is found [84].

Fundamentally different surface electronic properties were found for the asymmetric $p(2 \times 1)$ and $c(4 \times 2)$ reconstructions on Ge(100), while the electronic properties of the $p(2 \times 2)$ structure are nearly identical to those of the $c(4 \times 2)$ surface [86]. Theoretical analysis revealed an energy gap of 0.5 eV between filled bulk and empty surface states for the $p(2 \times 1)$ structure. In contrast, for the $c(4 \times 2)$ reconstruction, a surface state located 0.15 eV above the VBM was found, leading to a much smaller surface band gap. Experimentally, a surface state was observed 0.2 eV above the VBM and 0.08 eV above the Fermi level, E_F , for a Ge(100) surface that exhibits a highly-ordered striped $c(4 \times 2)/(2 \times 1)$ domain pattern. This surface state was attributed to the $c(4 \times 2)$ reconstruction and found to be partially occupied by thermally excited electrons at room temperature, leading to a metallic character of the Ge(100) surface [86]. However, the theoretical findings suggest that semiconducting behavior would arise if it was possible to exclusively probe $p(2 \times 1)$ domains. An overview of the surface reconstructions and related band gaps of Ge(111) and Ge(100) surfaces is given in Table 4.1.

Surface structure and LEED analysis

Prior to inelastic H atom scattering experiments, the surface cleanliness was checked by AES to ensure that no contaminants were present. The surface structure was studied using LEED. A typical LEED pattern obtained at room temperature is shown in Fig. 4.6 a. Sharp half-order diffraction spots related to the $p(2 \times 1)$ structure were generally observed. Additionally, the LEED pattern shows weak and diffuse stripes through the center of each zone related to an alternating or antiferromagnetic-like ordering of the asymmetric dimers within one row [97], which is typical of the $c(4 \times 2)$ and $p(2 \times 2)$ surface reconstructions. However, the orientation of these dimer rows with respect to each other essentially remains random as otherwise $c(4 \times 2)$ diffraction spots at quarter-order positions should be visible. Fig. 4.6 b shows a LEED pattern of the Ge(100) surface consisting of a highly-ordered $c(4 \times 2)/(2 \times 1)$ domain pattern, reprinted from Ref. [86]. Diffraction spots related to the $p(2 \times 1)$ and $c(4 \times 2)$ double domains are labeled. In contrast, no sharp $c(4 \times 2)$ diffraction spots are visible in Fig. 4.6 a. However, due to the observed striped pattern, it is assumed that both $p(2 \times 1)$ and $c(4 \times 2)$ domains are present on the Ge(100) surface sample used in inelastic H atom scattering experiments. Moreover, $p(2 \times 2)$ domains could exist, too. Denoting the surface as Ge(100)(2×1) thus refers to a surface with coexisting areas of different (2×1)-type surface reconstructions and not only to a $p(2 \times 1)$ structure.

The different possible surface structures complicate the analysis and interpretation of

4.4 The influence of surface structure: $Ge(100)$ vs. $Ge(111)$

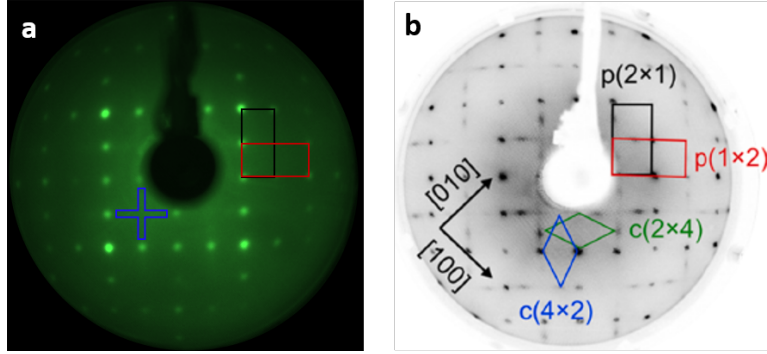


Figure 4.6: Room temperature LEED patterns of the $Ge(100)$ surface. Panel a shows a typical LEED pattern recorded after surface preparation with an electron energy of 120 eV. For clarification, red and black rectangular shapes connect diffraction spots related to the $p(2 \times 1)$ double domains. Diffuse stripes related to a $c(4 \times 2)$ -type ordering of the surface dimers are bordered by a blue shape. Panel b shows a LEED pattern of $Ge(100)$ with a highly-ordered $c(4 \times 2)/(2 \times 1)$ structure. The used electron energy is 110 eV. Diffraction spots related to the $p(2 \times 1)$ and $c(4 \times 2)$ double domains are labeled. An STM image of the surface is shown in Fig. 2.5 in Section 2.1. Panel b is reprinted from Ref. [86], Copyright 2021, with permission from Elsevier.

the data obtained for $Ge(100)(2 \times 1)$ since the ratio to which the different structures are present on the surface is essentially unknown. However, using H atom scattering, reproducible results were obtained on $Ge(100)(2 \times 1)$. This leads to the conclusion that either the procedure of surface preparation repeatedly resulted in the formation of similar surface structures or the actual surface structure and ratio of different reconstructions present on the surface have minor influence on the obtained results. However, the different reconstructions possess different electronic properties and temperature-dependent experiments on $Ge(111)c(2 \times 8)$ have previously shown that H atom scattering is sensitive to changing electronic properties. Consequently, the first assumption of a routinely utilized surface preparation resulting in reproducible surface structures seems to be more plausible.

Results: Energy-resolved angular distributions

Fig. 4.7 shows energy-resolved angular distributions observed for H atom scattering from $Ge(111)c(2 \times 8)$ and $Ge(100)(2 \times 1)$. The polar plots display the final translational energy E_f as a function of the final scattering angle ϑ_f . For both surfaces, similar bimodal distributions with energetically separated scattering channels are observed.

The results for $Ge(111)c(2 \times 8)$ are given in Fig. 4.7 a, b. Here, black dotted lines show

4 Hydrogen atom scattering from germanium surfaces

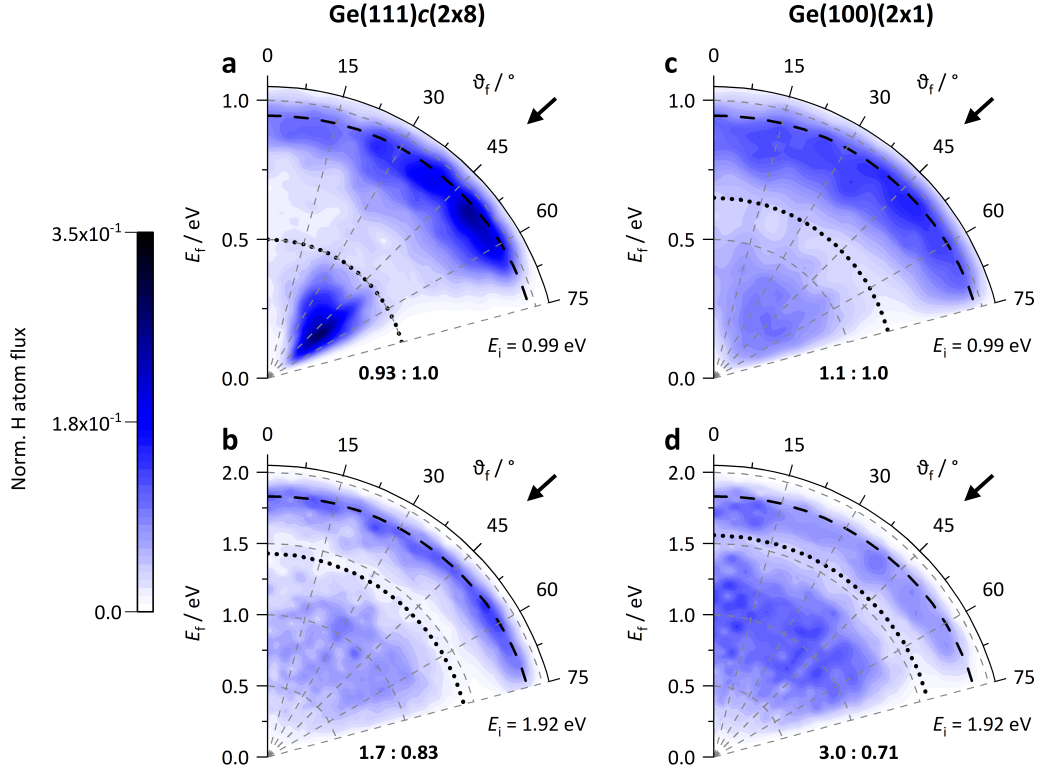


Figure 4.7: Comparison of H atom scattering from Ge(111)c(2 × 8) and Ge(100)(2 × 1). Energy-resolved angular distributions derived from in-plane scattering flux are shown for two incidence translational energies $E_i = 0.99\text{ eV}$ (a, c) and 1.92 eV (b, d). The surface temperature was $T_S = 300\text{ K}$ and the incidence angle is $\vartheta_i = 45^\circ$. The specular scattering angles are marked by arrows. H atom scattering from Ge(111)c(2 × 8) (a, b) is compared to Ge(100)(2 × 1) (c, d). On Ge(111)c(2 × 8), the incident H atoms travel along the $[\bar{1}10]$ surface direction, while on Ge(100)(2 × 1), they travel along $[001]$. To construct the plots, data was recorded in 5° increments from $\vartheta_f = 0$ to 75° . The integrated adiabatic channels are normalized to be equal for both surfaces at an incidence energy of $E_i = 0.99\text{ eV}$. The bold numbers show the ratios of the observed scattering channels with respect to the adiabatic channel for an incidence energy of $E_i = 0.99\text{ eV}$ for both surfaces, respectively. The left number corresponds to the electronically non-adiabatic channel and the right one to the adiabatic channel. The separation of both channels is indicated by black dotted lines. For Ge(111)c(2 × 8), the positions of the black dotted lines correspond to an energy-loss of 0.49 eV , i.e., the surface band gap [81]. For Ge(100)(2 × 1), the local minima between both channels are used as separation and correspond to energy-losses of 0.34 eV at an incidence energy of $E_i = 0.99\text{ eV}$ and 0.36 eV at $E_i = 1.92\text{ eV}$. The black dashed lines represent the final energy predicted by a line-of-centers binary collision model for an H atom impinging on a single Ge atom: $E_f = E_i \left\{ 1 - \cos^2[(\vartheta_i + \vartheta_f)/2] \times \left[1 - (m_H - m_{\text{Ge}})^2 / (m_H + m_{\text{Ge}})^2 \right] \right\}$.

4.4 The influence of surface structure: Ge(100) vs. Ge(111)

the minimal energy-loss that is expected for excitation of an electron across the band gap of the semiconducting surface. It demarcates the electronically adiabatic channel at high final energies from the non-adiabatic channel that involves transitions between electronic states and leads to much larger energy-losses.

For Ge(100)(2 × 1), it is more complicated to define a value that demarcates both scattering channels. Similar to Ge(111)*c*(2 × 8), Ge(100)(2 × 1) possesses bulk and surface electronic states. However, the positions of the surface states differ for the *c*(4 × 2) and *p*(2 × 1) reconstructions present on Ge(100), which makes it impossible to specify a certain energy gap between filled and empty states for the entire surface. Additionally, Ge(100)(2 × 1) exhibits a partially filled surface state at room temperature, which leads to its description as a metallic surface. Nevertheless, two energetically well-separated scattering channels are obtained on Ge(100)(2 × 1), too. Comparison with Ge(111)*c*(2 × 8) suggests that the low energy-loss channel is due to electronically adiabatic energy transfer to surface phonons, whereas the high energy-loss channel involves electronic excitation of the surface. To analyze the two channels individually, they were separated in energy at the local minimum between both channels, marked by the black dotted lines in Fig. 4.7 c, d. The local minima correspond to energy-losses of 0.34 eV at an incidence energy of $E_i = 0.99$ eV and 0.36 eV at $E_i = 1.92$ eV. However, it should be noted that these values are simply chosen because they accurately demarcate the two scattering channels at both incidence translational energies and thus have no explicit physical meaning in contrast to the surface band gap that separates both channels on Ge(111)*c*(2 × 8).

Separating the observed scattering channels allows an individual analysis of each channel as well as a comparison of their branching for both Ge surface facets. The branching ratios are given as bold numbers in Fig. 4.7. At low incidence translational energies, the adiabatic channel dominates on Ge(111)*c*(2 × 8), whereas on Ge(100)(2 × 1), the non-adiabatic channel is stronger than the adiabatic one. However, the difference between both surface facets is rather minor and could potentially be an effect of the chosen separation between both channels. In contrast, with increasing incidence translational energy, the non-adiabatic channel dominates on both facets, while it is clearly stronger on Ge(100)(2 × 1). For both surface facets, the energy-loss of the adiabatic channel follows a hard-sphere line-of-centers binary collision model (Fig. 4.7, black dashed lines), indicating that the H atoms scattering through the adiabatic channel experience binary collisions leading to a similar energy-loss on both Ge surfaces.

In Fig. 4.8, the polar plots are further analyzed. Fig. 4.8 a, b shows angle-integrated translational energy-loss distributions at two incidence energies for both Ge surface facets in direct comparison, illustrating the similar bimodal shapes of the distributions

4 Hydrogen atom scattering from germanium surfaces

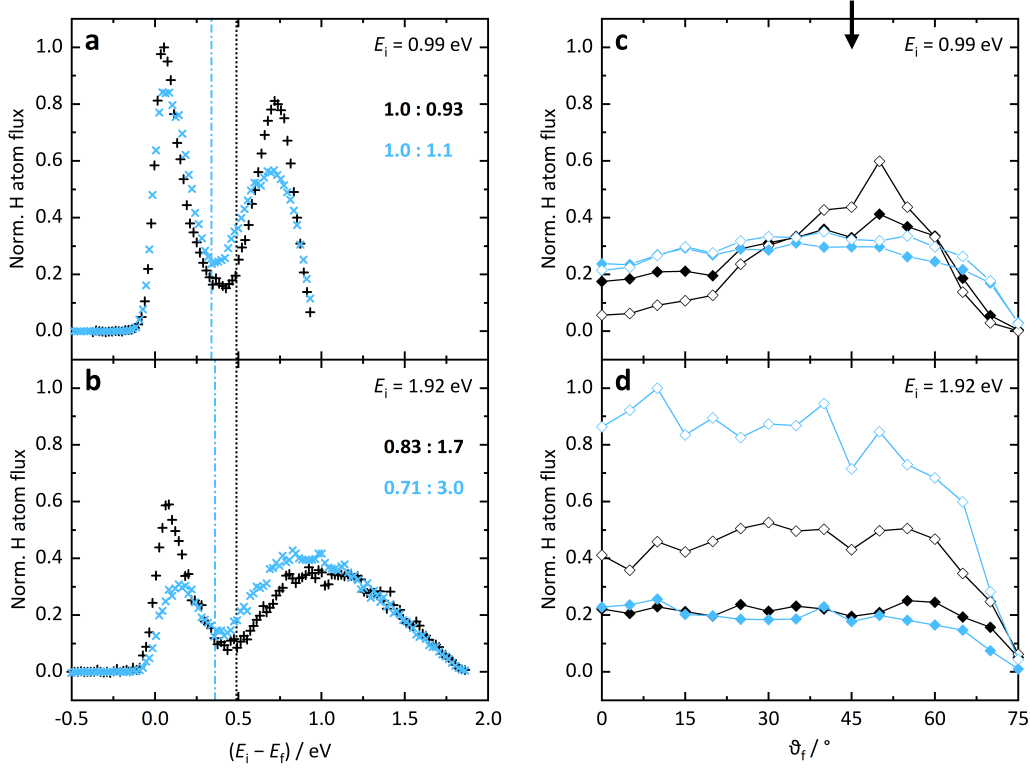


Figure 4.8: Comparison of H atom scattering from Ge(111)c(2 × 8) and Ge(100)(2 × 1). Angle-integrated translational energy-loss distributions (a, b) and energy-integrated angular distributions (c, d) derived from data given in Fig. 4.7 are shown for Ge(111)c(2 × 8) (black) and Ge(100)(2 × 1) (blue) for two incidence translational energies $E_i = 0.99$ eV (a, c) and 1.92 eV (b, d). All other experimental conditions are the same as in Fig. 4.7. To construct the angle-integrated energy-loss distributions (a, b), angle-resolved energy-loss distributions recorded in 5° increments from $\vartheta_f = 0$ to 75° , given in Fig. 4.7, were summed up. The curves are further normalized to the peak intensity of the adiabatic channel obtained for Ge(111)c(2 × 8) at an incidence energy of $E_i = 0.99$ eV. The black dotted and blue dash-dotted lines separate the two scattering channels for Ge(111)c(2 × 8) (black plus signs) and Ge(100)(2 × 1) (blue crosses), respectively. The bold numbers show the ratios of the observed scattering channels with respect to the adiabatic channel for an incidence energy of $E_i = 0.99$ eV, as in Fig. 4.7. Here, the left number corresponds to the adiabatic channel and the right one to the non-adiabatic channel. To construct the energy-integrated angular distributions (c, d), the energy-loss distribution at each scattering angle was summed up in energy-space; however, divided into the adiabatic (filled diamonds) and the non-adiabatic channel (open diamonds). The curves are normalized to the peak intensity of the non-adiabatic channel obtained for Ge(100)(2 × 1) at an incidence energy of $E_i = 1.92$ eV. The specular scattering angle is marked by an arrow at the top of panel c.

4.4 The influence of surface structure: Ge(100) vs. Ge(111)

Table 4.2: Angular full width at half maximum. Angular distributions of the non-adiabatic and adiabatic channel for Ge(111) $c(2 \times 8)$ and Ge(100)(2×1) are compared for two incidence energies $E_i = 0.99$ eV and 1.92 eV, as shown in Fig. 4.8.

E_i	Non-adiabatic		Adiabatic	
	0.99 eV	1.92 eV	0.99 eV	1.92 eV
Ge(111) $c(2 \times 8)$	31°	> 70°	44°	> 73°
Ge(100)(2×1)	> 70°	> 67°	> 71°	> 66°

in energy-space. Compared to Ge(111) $c(2 \times 8)$, the onset of the non-adiabatic channel is shifted towards slightly lower energy-losses for Ge(100)(2×1), arguing for a smaller energy gap that needs to be overcome for electronic excitation on the Ge(100)(2×1) surface. Fig. 4.8c,d shows angular distributions of the adiabatic and non-adiabatic scattering channels for Ge(100)(2×1) and Ge(111) $c(2 \times 8)$ at both incidence energies. Similarly broad angular distributions are observed for both channels except for Ge(111) $c(2 \times 8)$ at an incidence translational energy of $E_i = 0.99$ eV. Here, relatively narrow angular distributions are obtained, the non-adiabatic channel is even narrower than the adiabatic channel. The angular distributions of both channels broaden significantly between $E_i = 0.99$ eV and 1.92 eV. For Ge(100)(2×1), no such effect is observed since broad angular distributions are obtained already at $E_i = 0.99$ eV. The difference to Ge(111) $c(2 \times 8)$ becomes especially apparent when comparing the non-adiabatic channel for both facets at $E_i = 0.99$ eV. For Ge(111) $c(2 \times 8)$, a very narrow angular distribution is observed, whereas for Ge(100)(2×1), an evenly broad distribution is obtained. Table 4.2 summarizes the full widths at half maximum (FWHM) of the angular distributions obtained for both surface facets and incidence translational energies.

Results: Effect of surface temperature

The effect of surface temperature on the energy-loss distributions of H atoms scattered from Ge(100) is shown in Fig. 4.9. For Ge(111), a similar figure is given in Ref. [152] in Section 4.3.

Ge(111) $c(2 \times 8)$ is semiconducting at room temperature but shows a gradual metallization with increasing surface temperature [111, 114, 153]. In contrast, Ge(100)(2×1) is of metallic nature at room temperature due to thermal occupation of a surface state related to the $c(4 \times 2)$ structure close to the Fermi level [86]. Using ARPES, this state is observed at temperatures higher than 220 K [96].

4 Hydrogen atom scattering from germanium surfaces

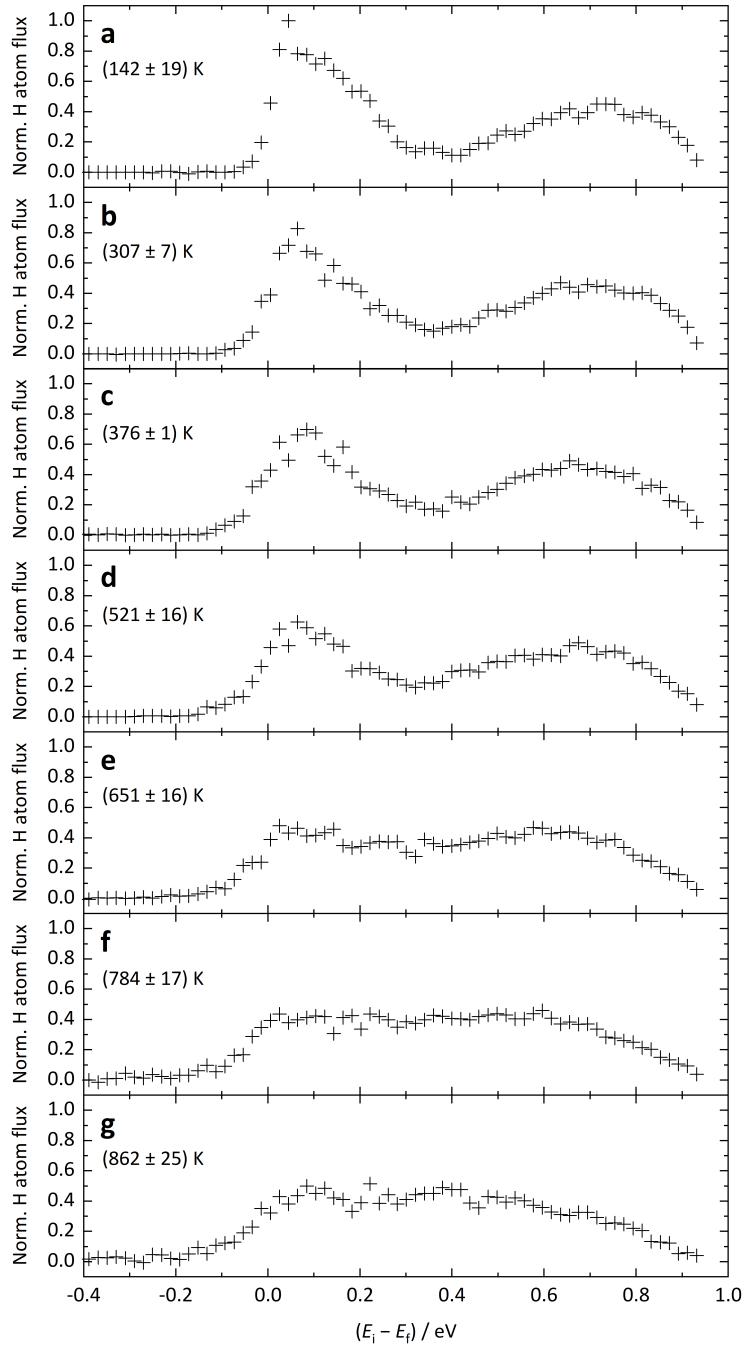


Figure 4.9: Translational energy-loss distributions for H atoms scattered from a Ge(100) surface at different surface temperatures. The incident H atoms travel along the [001] surface direction. The polar incidence and scattering angles ϑ_i and ϑ_f , respectively, are both 45° with respect to the surface normal. The incidence translational energy of the H atoms is $E_i = 0.99$ eV. Experiments were performed at seven different surface temperatures, T_S , given in each panel. The energy-loss distributions are normalized to the integrated signal.

4.4 The influence of surface structure: Ge(100) vs. Ge(111)

With inelastic H atom scattering, similar results are obtained for both Ge surface facets as a function of surface temperature. As the temperature is increased, the energy-loss distributions change: the bimodal structure vanishes and the obtained distributions become broader and structureless. This leads to the conclusion that for both surface facets, the same or very similar processes are relevant to the observed energy-loss with increasing surface temperature. For Ge(111), it was shown that the energy-loss consists of three components, an insulator, a semiconductor, and a metal component, whose relative contributions are temperature-dependent. With increasing surface temperature, the metal component becomes stronger, whereas the contributions of the insulator and semiconductor components decrease. Thus, at elevated temperatures, energy-loss to semiconductor and metal surfaces converge. Fig. 4.10 b shows nearly identical energy-loss distributions of H atoms scattering from Ge(100) and Ge(111) at surface temperatures of about $T_S = 900$ K, which agree with the results obtained on a Cu(111) surface. However, Ge(100) is described to be metallic at room temperature already. Nevertheless, the results from H atom scattering indicate that its metallicity further increases with surface temperature, too. For both surfaces, the increase in metallicity is potentially mainly due to thermal occupation of surface or bulk electronic states lying above the Fermi level, E_F . However, the lowest temperature at which metallic behavior is observed obviously differs for both surface facets; it is lower for Ge(100). Likewise, for Ge(100), a broad and metal-like energy-loss distribution is already observed at lower surface temperatures than for Ge(111). These observations suggest that a gradual metallization occurs on both Ge surface facets with increasing surface temperature. However, the starting temperature of this process is different, it is lower for Ge(100) than for Ge(111).

Fig. 4.10 a presents energy-loss distributions of H atoms scattering from Ge(111) $c(2 \times 8)$ and Ge(100) (2×1) at low surface temperatures in direct comparison. Although the observed overall trend with increasing surface temperature is similar for both surfaces, potential differences of the energy-loss distributions should be best resolved at low temperatures, where thermal broadening is least important. In this regard, it is noted that, with decreasing temperature, the structural and electronic properties of the surfaces might also change. For Ge(100), the $c(4 \times 2)$ reconstruction dominates at temperatures below $T_S = 220$ K and the surface state close to the Fermi level, which becomes thermally occupied at higher temperatures, is empty.

In Fig. 4.10 a, the non-adiabatic channels of both distributions show prominent differences. Both peak shape and onset differ for the two surface facets reflecting their diverse electronic structures. However, analyzing the peaks at low energy-losses can potentially

4 Hydrogen atom scattering from germanium surfaces

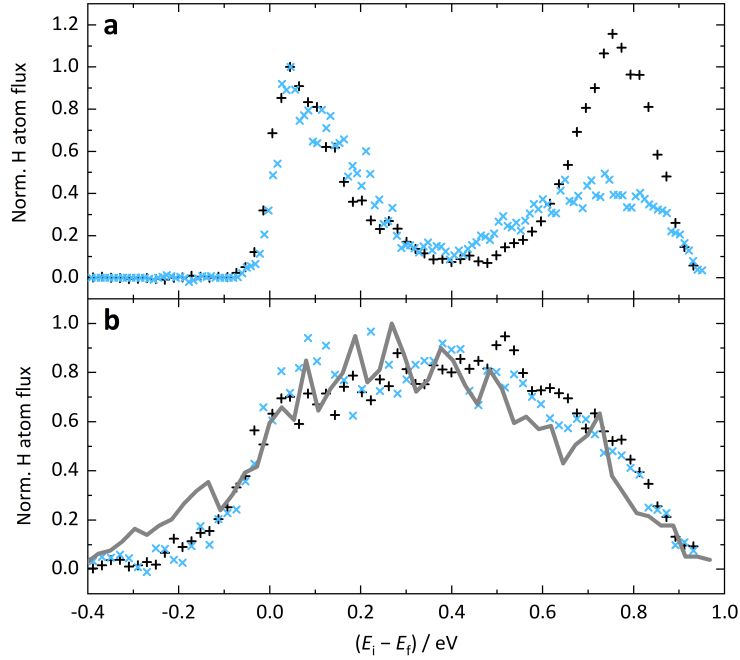


Figure 4.10: Comparison of inelastic H atom scattering from Ge(111) and Ge(100) at low (a) and high (b) surface temperatures. Translational energy-loss distributions derived from experiment are shown for Ge(111) (black plus signs) and Ge(100) (blue crosses). Theoretical results obtained for Cu(111) (gray line) are additionally shown in panel b. For Ge(100), Ge(111) and Cu(111), the incident H atoms travel along the $[001]$, $[\bar{1}10]$ and $[10\bar{1}]$ surface direction, respectively. All other scattering conditions are the same as in Fig. 4.9. Panel a: The surface temperature of Ge(111) was $T_S = (137 \pm 6)$ K, while the surface temperature of Ge(100) was $T_S = (142 \pm 19)$ K. The distribution obtained for Ge(111) is scaled to fit the peak maximum of the adiabatic channel of the energy-loss distribution recorded for H atoms scattering from Ge(100). Compared to Fig. 4.9 a, the energy increment between two data points is divided in half for the distribution obtained on Ge(100) and thus the number of data points shown is doubled. Panel b: The surface temperature of Ge(111) was $T_S = (942 \pm 21)$ K, the surface temperature of Ge(100) was $T_S = (862 \pm 25)$ K and the surface temperature of Cu(111) was $T_S = 950$ K. The energy-loss distributions are normalized to the integrated signal.

be rewarding, too. For Ge(100)(2×1), it would ideally be possible to observe energetically well-resolved scattering channels corresponding to electronically adiabatic energy transfer as well as electronic excitation from filled electronic states to empty surface states assignable to the respective reconstructions present on the surface. An energy gap of 0.5 eV was found for the $p(2 \times 1)$ structure, whereas a state lying approximately 0.2 eV above the VBM was attributed to the $c(4 \times 2)$ reconstruction. Considering Fig. 4.10 a, one could potentially argue that a shoulder arises in the energy-loss distribution ob-

4.4 The influence of surface structure: Ge(100) vs. Ge(111)

tained for Ge(100)(2×1) at an energy-loss of about 0.2 eV, which would perfectly agree with the $c(4 \times 2)$ -related surface state lying 0.2 eV above the VBM. However, this interpretation is very speculative, especially as it relies on one measurement with relatively noisy signal that can be delusive. To elucidate the scattering dynamics, experiments at even lower surface temperatures and H atom incidence energies are eligible. At an incidence energy of $E_i = 0.37$ eV for instance, electronic excitation would – if at all – only be possible on $c(4 \times 2)$ domains of the Ge(100) surface, whereas the energy gap inherent to $p(2 \times 1)$ domains exceeds the available energy, thereby preventing electronic excitation.

Discussion

For a general discussion of the H atom scattering results obtained on Ge(100)(2×1) and Ge(111) $c(2 \times 8)$, it is advantageous to first name the major differences of both surface facets again. Firstly, they possess completely different surface structures and thus, different types of surface atoms. Secondly, the electronic structure of both surface facets is different, with the electronic structure being strongly correlated to the atomic geometry. Surface states differ in both type and position for both of the surface facets. Furthermore, Ge(111) $c(2 \times 8)$ is semiconducting at room temperature, whereas Ge(100)(2×1) is of metallic nature.

H atoms that collide with a Ge surface can either experience a mechanical interaction or an electronically non-adiabatic interaction leading to electronic excitation of the surface. By now, the mechanism of energy transfer resulting in electronic excitation of the surface is not completely understood and a theoretical description will be required in the future to elucidate it. However, on Ge(111) $c(2 \times 8)$, electronic excitation is observed and this can only be due to the promotion of an electron from a filled bulk or surface electronic state to an initially empty state, corresponding to an interband excitation. In contrast, Ge(100)(2×1) additionally possesses partially filled states at room temperature. Thus, intraband excitations could be feasible, too. However, based on the very similar results for both surface facets, they can – if at all – only account for a minor contribution to the energy-loss due to electronic excitation of the surface.

Nevertheless, there are still some small differences in the results obtained for both surfaces, which will be discussed in the following.

Firstly, the angular distributions of both channels at low incidence translational energy are broader for H atom scattering from Ge(100)(2×1) than for Ge(111) $c(2 \times 8)$. Angular distributions can reflect the structural geometry of a surface. Thus, it is not surprising that they differ for both surface facets as they show completely different structures. Nev-

4 Hydrogen atom scattering from germanium surfaces

ertheless, the different widths of the non-adiabatic channels are particularly striking and in the case of $\text{Ge}(111)c(2 \times 8)$ it was argued that the narrow angular distribution reflects some steric restrictions for this channel (Section 4.1, Ref. [150]). Secondly, the branching ratio of the non-adiabatic to adiabatic channel is much larger for $\text{Ge}(100)(2 \times 1)$ than for $\text{Ge}(111)c(2 \times 8)$ at an incidence energy of $E_i = 1.92 \text{ eV}$. Both observations could serve as evidence that $\text{Ge}(100)(2 \times 1)$ is more prone to electronic excitation than $\text{Ge}(111)c(2 \times 8)$. Asymmetric surface dimers are formed on $\text{Ge}(100)(2 \times 1)$, with the remaining dangling bond of the down dimer-atom being empty and the remaining dangling bond of the up atom being filled due to a surface charge transfer [82, 86]. The filled up dimer-atom surface state was found to merge with bulk states at the VBM [86]. This could entail that electronic excitation of the surface is more probable if the impinging H atom hits the up dimer-atom compared to the down dimer-atom. Similarly, on $\text{Ge}(111)c(2 \times 8)$, a charge transfer between adatom and rest atom dangling bonds leads to a filled rest atom surface state merging with the bulk valence band and an empty adatom surface state. Here, it is conceivable that the impinging H atom needs to collide with a rest atom in order to entail electronic excitation. On $\text{Ge}(111)c(2 \times 8)$, one out of eight surface atoms is a rest atom. In contrast, on $\text{Ge}(100)(2 \times 1)$, each surface unit cell contains one up dimer-atom, while it is comprised of six surface atoms overall. Thus, hitting an up dimer-atom on the $\text{Ge}(100)(2 \times 1)$ surface is potentially more likely for an impinging H atom than colliding with a rest atom present on the $\text{Ge}(111)c(2 \times 8)$ surface. However, it should be noted here, that H atoms impinging on surface sites other than dimer atoms or rest and adatoms, respectively, might also be involved in the process of electronic excitation of the surface.

To conclude, similar results are obtained for H atom scattering from $\text{Ge}(100)(2 \times 1)$ and $\text{Ge}(111)c(2 \times 8)$, although both surfaces exhibit different structural and electronic properties. Small differences can be consistently interpreted based on the known properties of both surfaces and support the current understanding of H atom scattering from semiconductor surfaces. However, a theoretical model will be required in the future to obtain a detailed understanding of the involved processes.

4.5 Scattering from hydrogenated Ge(111)

This section presents H atom scattering from hydrogenated Ge(111) surfaces and compares the results to H atom scattering from clean Ge(111) $c(2 \times 8)$. Energy-integrated angular distributions and translational energy-loss distributions were measured for two incidence translational energies. H atom scattering from hydrogenated and deuterated Ge(111) surfaces is compared by means of translational energy-loss distributions.

Structural and electronic properties: Influence of hydrogenation

Hydrogenation strongly modifies the structural and electronic properties of the Ge(111) surface. This is described in detail in Section 2.3. In short, hydrogenation removes the $c(2 \times 8)$ reconstruction leading to a bulk-like surface structure with H atoms terminating the unsaturated Ge surface atoms [132, 136]. Prior to hydrogenation, the Ge sample was annealed at $T_S = 940$ K. During hydrogenation, the sample was kept at room temperature, which predominantly leads to the formation of monohydride on the surface [134]. LEED patterns recorded after hydrogenation show sharp (1×1) diffraction spots without any indication of extant $c(2 \times 8)$ structures, see Fig. 4.11 b.

Hydrogenation also changes the electronic properties of the Ge(111) surface. Surface states associated with adatom and rest atom dangling bonds as well as adatom back-bonds disappear as adatoms are removed from the surface and dangling bonds are saturated by H atoms. Simultaneously, new surface resonances are observed outside of

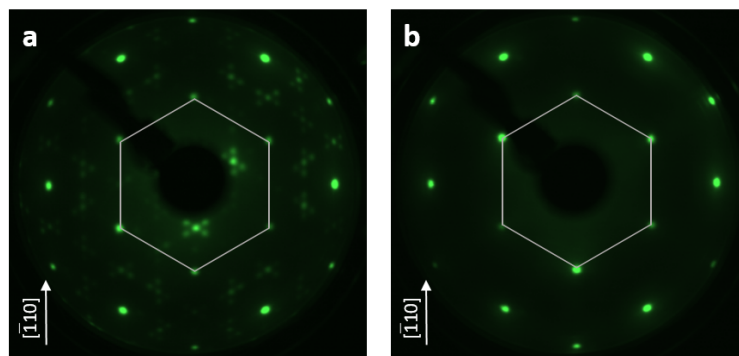


Figure 4.11: LEED patterns of the clean Ge(111) $c(2 \times 8)$ surface (a) and the hydrogenated Ge(111) (1×1) :H surface (b). Both LEED patterns were recorded within 1 h; prior to and after hydrogenation, respectively. The patterns were obtained at room temperature with an electron energy of 100 eV. For clarification, (1×1) diffraction spots are connected by a gray hexagonal shape. The Ge(111) $c(2 \times 8)$ surface (a) shows additional half-order and eighth-order spots associated with the $c(2 \times 8)$ superlattice.

4 Hydrogen atom scattering from germanium surfaces

the fundamental Ge bulk band gap. Compared to $\text{Ge}(111)c(2 \times 8)$, the surface band gap of $\text{Ge}(111)(1 \times 1):\text{H}$ is broadened as the unoccupied adatom-induced surface state vanishes upon hydrogenation [133].

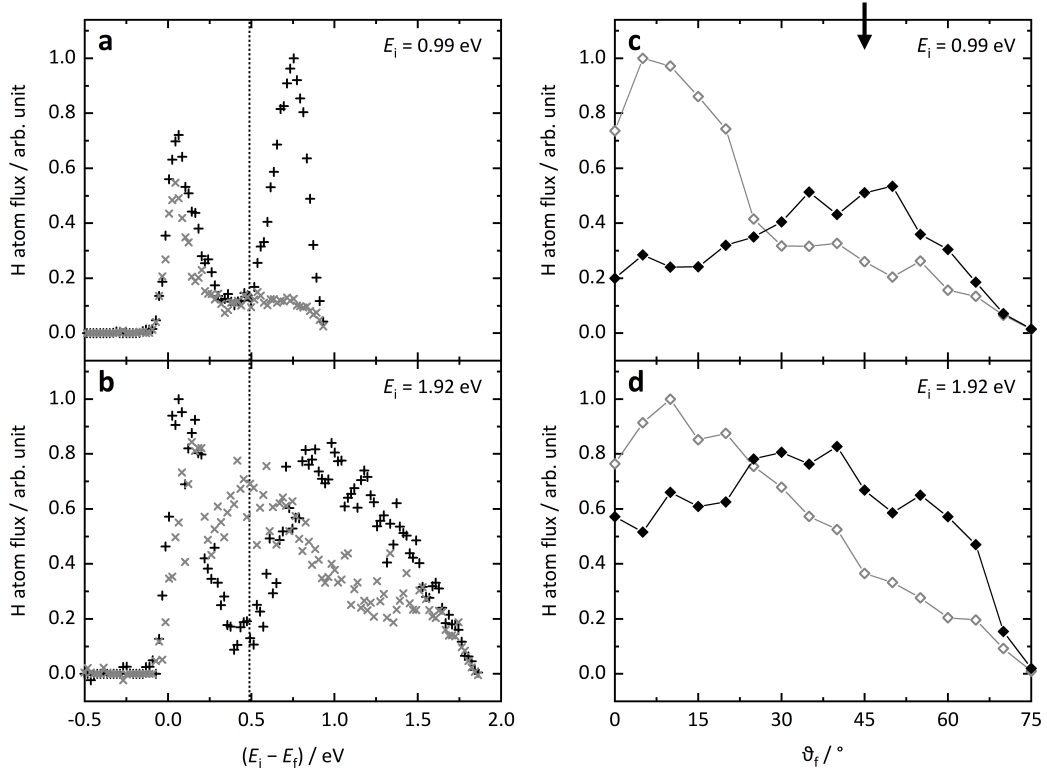


Figure 4.12: Comparison of H atom scattering from $\text{Ge}(111)c(2 \times 8)$ and hydrogenated $\text{Ge}(111)(1 \times 1):\text{H}$. Translational energy-loss distributions (a, b) and energy-integrated angular distributions (c, d) are shown for $\text{Ge}(111)c(2 \times 8)$ (black plus signs and filled diamonds) and $\text{Ge}(111)(1 \times 1):\text{H}$ (gray crosses and open diamonds) for two incidence translational energies $E_i = 0.99 \text{ eV}$ (a, c) and 1.92 eV (b, d). The incident H atoms travel along the $[\bar{1}10]$ surface direction. The surface temperature was $T_S = 300 \text{ K}$ and the polar incidence angle is $\vartheta_i = 45^\circ$. Within each panel, the most intensive distribution is normalized to peak intensity. The translational energy-loss distributions were recorded at a specular scattering angle of $\vartheta_f = 45^\circ$. The black dotted line indicates the surface band gap of 0.49 eV of $\text{Ge}(111)c(2 \times 8)$ as given in Ref. [81]. To construct the energy-integrated angular distributions, energy-loss distributions, measured at scattering angles ranging from $\vartheta_f = 0$ to 75° in 5° increments, were summed up each over the entire energy-space ranging from $(E_i - E_f) = -0.5$ to 1 eV or 2 eV , respectively. The specular scattering angle is marked by an arrow at the top of panel c.

Results

Fig. 4.12 shows translational energy-loss distributions and energy-integrated angular distributions for H atoms scattering from clean Ge(111) $c(2 \times 8)$ and hydrogenated Ge(111)(1×1):H surfaces with two incidence translational energies, $E_i = 0.99$ eV and 1.92 eV, in direct comparison. The translational energy-loss distributions were recorded for H atoms scattered at the specular angle.

At an incidence energy of $E_i = 0.99$ eV (Fig. 4.12 a), the energy-loss distribution of H atoms scattered from Ge(111)(1×1):H shows only one peak which is in excellent agreement with the adiabatic peak of the bimodal distribution obtained on Ge(111) $c(2 \times 8)$. The non-adiabatic channel at higher energy-losses is completely missing. Consequently, the experimental results obtained on the hydrogenated Ge surface resemble the results of electronically adiabatic MD simulations for H atom scattering from Ge(111) $c(2 \times 8)$, as given in Ref. [150] in Section 4.1. This leads to the conclusion that on Ge(111)(1×1):H, the energy-loss from H atoms to the surface can be described entirely electronically adiabatic and no electronic excitation of the surface is involved. The electronically adiabatic energy-loss, extending from negative energy-losses to an energy-loss corresponding to the value of the surface band gap of Ge(111) $c(2 \times 8)$, is similar for clean and hydrogenated Ge(111). Most probable energy-losses of 45 meV and 65 meV are found for Ge(111)(1×1):H and Ge(111) $c(2 \times 8)$, respectively, and the same average energy-loss of 0.14 eV each. This leads to the conclusion that the impinging H atoms mainly hit Ge surface atoms on Ge(111)(1×1):H. Otherwise, if collisions with hydrogen atoms adsorbed on the surface were important, larger energy-losses would be expected for Ge(111)(1×1):H. This is due to the more efficient energy transfer between atoms of equal masses compared to the more inefficient energy transfer between light H atoms and heavier Ge surface atoms that certainly dominates on Ge(111) $c(2 \times 8)$ and apparently also on Ge(111)(1×1):H.

Translational energy-loss distributions for H atoms with an incidence energy of $E_i = 1.92$ eV are shown in Fig. 4.12 b. Again, the shape of the distributions differs for H atom scattering from clean and hydrogenated Ge(111). While the adiabatic feature at low energy-losses is present for both surfaces, the well-resolved non-adiabatic channel is missing for Ge(111)(1×1):H. However, in contrast to the distribution obtained at a lower incidence energy of $E_i = 0.99$ eV, another feature emerges at intermediate energy-losses. This channel could either be due to electronically adiabatic or non-adiabatic energy transfer to the surface. The latter case would lead to electronic excitation of the surface. However, as previously described, the electronic structure of the Ge(111) surface changes upon hydrogenation and the surface band gap increases since the sur-

4 Hydrogen atom scattering from germanium surfaces

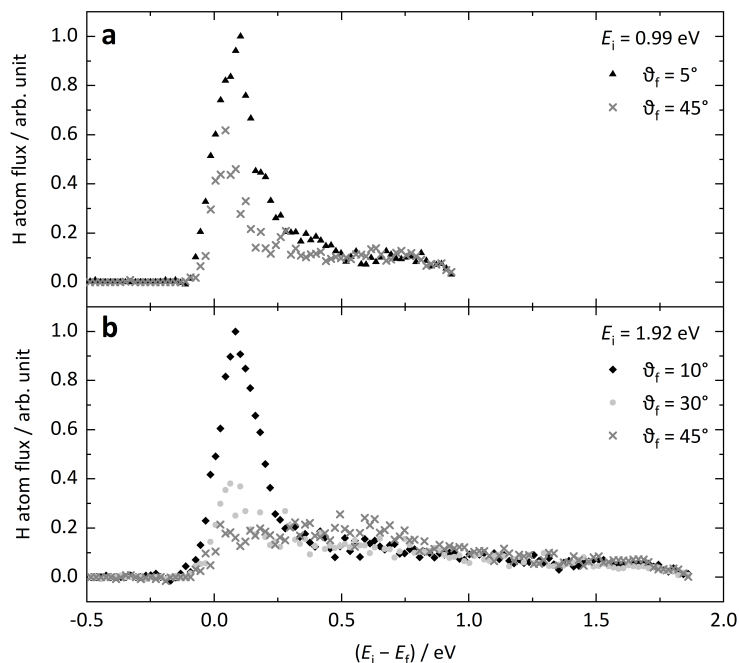


Figure 4.13: Scattering angle-dependent translational energy-loss distributions of H atoms scattered from hydrogenated Ge(111)(1 × 1):H. Translational energy-loss distributions are shown for two incidence translational energies $E_i = 0.99$ eV (a) and 1.92 eV (b). The incident H atoms travel along the $[\bar{1}10]$ surface direction, while the polar incidence angle is $\vartheta_i = 45^\circ$. The surface temperature was $T_S = 300$ K. For an incidence energy of $E_i = 0.99$ eV (a), the translational energy-loss distributions were recorded at scattering angles of $\vartheta_f = 5^\circ$ (black triangles) and 45° (dark gray crosses). For $E_i = 1.92$ eV (b), the translational energy-loss distributions were recorded at scattering angles of $\vartheta_f = 10^\circ$ (black diamonds), 30° (light gray circles) and 45° (dark gray crosses). Within each panel, the most intensive distribution is normalized to peak intensity.

face state associated with Ge adatoms, lying within the bulk band gap, is removed. Consequently, even higher energy-losses would be expected if electronic excitation of the hydrogenated Ge(111) surface was feasible at all. In the more probable case that electronically adiabatic energy transfer induces the occurrence of the new channel at intermediate energy-losses, adiabatic MD simulations should be able to reproduce the experimental results and elucidate the underlying scattering mechanism. However, at this particular time, MD simulations for H atom scattering from Ge(111)(1 × 1):H are not yet available.

Energy-integrated angular distributions for H atoms scattering from clean and hydrogenated Ge(111) surfaces are shown in Fig. 4.12 c, d for incidence translational energies

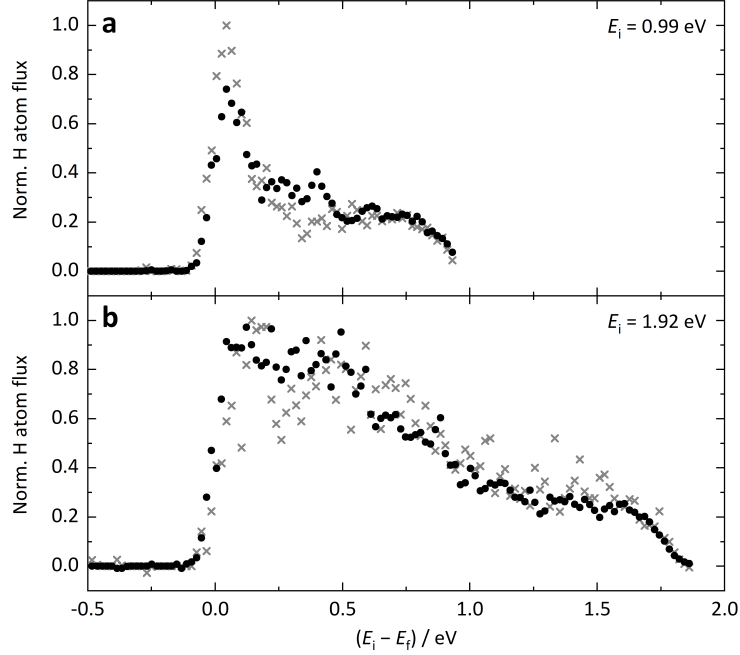


Figure 4.14: Comparison of H atom scattering from hydrogenated Ge(111)(1 × 1):H and deuterated Ge(111)(1 × 1):D. Translational energy-loss distributions are shown for Ge(111)(1 × 1):H (gray crosses) and Ge(111)(1 × 1):D (black circles) for two incidence translational energies $E_i = 0.99$ eV (a) and 1.92 eV (b). The incident H atoms travel along the $[\bar{1}10]$ surface direction, while the polar incidence and scattering angles ϑ_i and ϑ_f , respectively, were both 45° with respect to the surface normal. The surface temperature was $T_S = 300$ K. The energy-loss distributions are normalized to the integrated signal.

of $E_i = 0.99$ eV and 1.92 eV, respectively. For Ge(111)(1 × 1):H, the relatively narrow angular distributions peak close to the surface normal. In contrast, the maxima of the angular distributions obtained on clean Ge(111) $c(2 \times 8)$ are found close to the specular scattering angle. The signal increase towards smaller scattering angles observed for Ge(111)(1 × 1):H is particularly striking in direct comparison to the results obtained on Ge(111) $c(2 \times 8)$. Furthermore, it is reflected in the scattering angle-dependent translational energy-loss distributions shown in Fig. 4.13. Here, energy-loss distributions for H atoms scattering from hydrogenated Ge(111)(1 × 1):H are displayed for various scattering angles, ϑ_f , and two incidence translational energies, $E_i = 0.99$ eV (Fig. 4.13 a) and 1.92 eV (Fig. 4.13 b). With decreasing scattering angle, a strong signal increase is observed at both incidence energies. At $E_i = 0.99$ eV, the shape of the energy-loss distributions is similar for both scattering angles investigated. In contrast, at $E_i = 1.92$ eV, the shape of the distributions changes with scattering angle. As previously described,

4 Hydrogen atom scattering from germanium surfaces

H atom flux at intermediate energy-losses around $(E_i - E_f) = 0.5$ eV is observed for specularly scattered H atoms ($\vartheta_f = 45^\circ$). With decreasing scattering angle, this energy-loss channel vanishes. Thus, the new scattering channel appears to possess a relatively narrow angular distribution and only contributes to the signal obtained at specular and – potentially – superspecular scattering angles. For $\vartheta_f \leq 30^\circ$, the peak at low energy-losses dominates leading to a distribution that resembles the distribution at lower incidence energy as well as the results of adiabatic MD simulations for Ge(111) $c(2 \times 8)$. The angular distribution of the intermediate energy-loss channel observed at $E_i = 1.92$ eV possibly also accounts for the different shapes of the total angular distributions given in Fig. 4.12 c, d for Ge(111)(1×1):H at the two incidence energies, respectively. Around the specular scattering angle, it adds signal to the angular distribution obtained at $E_i = 1.92$ eV, making the peak of the distribution close to the surface normal less pronounced compared to the distribution obtained at $E_i = 0.99$ eV, where the intermediate energy-loss channel is absent.

In Fig. 4.14, translational energy-loss distributions for H atom scattering from hydrogenated and deuterated Ge(111) surfaces are compared. Very similar results are obtained for the Ge(111) surface terminated with the two different hydrogen isotopes, confirming that the energy transfer primarily occurs during H–Ge collisions as H–H and H–D collisions should result in an isotope effect reflected in the observed energy-loss. Most probable and average energy-losses are given in Table 4.3 for both incidence energies and surfaces. The shape of the energy-loss distributions obtained at an incidence energy of $E_i = 1.92$ eV (Fig. 4.14 b) are nearly identical. Based on the previous analyses, two – presumably adiabatic – scattering channels are expected. At $E_i = 0.99$ eV, small

Table 4.3: Comparison of the most probable and average energy-losses of H atom scattering from hydrogenated and deuterated Ge(111) surfaces. The most probable energy-loss $(E_i - E_f)_p$ and the average energy-loss $(E_i - E_f)_{\text{avg}}$ are given for H atoms with incidence translational energies of $E_i = 0.99$ eV and 1.92 eV, which are specularly scattered from Ge(111)(1×1):H and Ge(111)(1×1):D, respectively. The corresponding translational energy-loss distributions are shown in Fig. 4.14.

	$E_i = 0.99$ eV		$E_i = 1.92$ eV	
	$(E_i - E_f)_p$	$(E_i - E_f)_{\text{avg}}$	$(E_i - E_f)_p$	$(E_i - E_f)_{\text{avg}}$
Ge(111)(1×1):H	0.045 eV	0.29 eV	0.14 eV	0.70 eV
Ge(111)(1×1):D	0.045 eV	0.33 eV	0.12 eV	0.63 eV

differences are observed in the shape of the distributions that could either be due to noisy signal or indicate the emergence of the intermediate energy-loss channel on the deuterated surface, whereas on Ge(111)(1 × 1):H it is not yet visible.

Using the deuterated Ge(111) surface, an experiment to reveal a potential H–D atom exchange reaction on the surface was additionally performed. Here, H atoms were shot onto the surface, while employing experimental settings specific to D atom detection. This way, it is in principle possible to detect D atoms desorbing from the deuterated surface after interaction with the impinging H atoms. Different experimental settings, such as timings and detector positions, were applied. However, no D atoms were detected leading to the conclusion that no significant H–D atom exchange happens on the surface.

Discussion

Upon hydrogenation, the $c(2 \times 8)$ adatom reconstruction of Ge(111) is removed and surface dangling bonds are saturated. Simultaneously, the electronic structure of the surface is altered as adatom and dangling bond related surface states vanish. Compared to clean Ge(111) $c(2 \times 8)$, the surface band gap broadens, affecting at least the onset of the non-adiabatic channel in translational energy-loss distributions obtained from inelastic H atom scattering. In fact, the non-adiabatic channel is completely absent for H atoms impinging on the Ge(111)(1 × 1):H surface with an incidence energy of $E_i = 0.99$ eV.

The indirect bulk band gap of Ge is 0.664 eV [63] at room temperature. However, no energy-loss component with an onset close to this value is observed. Even though the incidence translational energy exceeds the value of the bulk band gap, the energy could still be insufficient to engender electronic excitation. Moreover, coupling to bulk states might be generally less efficient for H atoms impinging on the surface. In any case, higher H atom incidence energies should enhance the probability to observe electronic excitation on hydrogenated Ge(111), too.

In fact, with increasing incidence energy, a scattering channel with larger energy-losses is observed. However, the energy-loss is still too small to be explained by the promotion of an electron across the bulk band gap or any even larger energy gap between surface states. Thus, it is more probable that this scattering channel stems from an electronically adiabatic energy transfer to the surface. In this regard, a comparison of the experimental results to the results of electronically adiabatic MD simulations will be very fruitful to, first of all, confirm the electronically adiabatic process and, secondly, elucidate the underlying scattering mechanism. In view of MD simulations,

4 Hydrogen atom scattering from germanium surfaces

Ge(111)(1 × 1):H further has the advantage of a relatively simple surface structure with a much smaller surface unit cell compared to Ge(111)*c*(2 × 8).

Angular distributions of H atoms scattering from hydrogenated Ge(111) are relatively narrow as they possess a strong peak close to the surface normal. At large scattering angles, decreased signal compared to scattering from clean Ge(111)*c*(2 × 8) is found. Based on the comparison of translational energy-losses of H atoms scattered from clean and hydrogenated Ge surfaces, it is concluded that the majority of scattering events on Ge(111)(1 × 1):H include H–Ge atom interactions. After such a collision, the H atom leaves the surface and thereby passes adsorbed H atoms that bind perpendicular to the surface plane on top of the first Ge surface layer. When the scattered H atom hits one of the adsorbed H atoms, it can additionally lose a certain amount of its parallel momentum and leave the surface at a scattering angle closer to the surface normal. Alternatively, an H atom leaving the surface at a large scattering angle after collision with a Ge surface atom could experience a second collision with an adsorbed H atom, bounce back towards the surface and stick to the surface, thereby being lost for detection.

To conclude, hydrogenation of the Ge(111) surface strongly alters the results of inelastic H atom scattering. For relatively low incidence translational energies of about 1 and 2 eV, the scattering dynamics probably involve no electronic excitation of the surface. In contrast to H atom scattering from Ge(111)*c*(2 × 8), where electronically adiabatic MD simulations can only reproduce half of the experimental findings at these incidence energies, H atom scattering from Ge(111)(1 × 1):H represents a system that can possibly be entirely described and understood based on adiabatic MD simulations. Experiments using higher H atom incidence translational energies would be interesting to test if electronic excitation of the surface was feasible at all.

Additionally, H atom scattering experiments could be performed using a hydrogenated Ge(100) surface and various incidence translational energies. In terms of their electronic structure, hydrogenated Ge(111) and Ge(100) surfaces are similar and would allow to study the pure influence of surface geometry on H atom scattering. However, as described in Section 2.3, hydrogenated Ge(100) surfaces must be carefully prepared to ensure formation of either monohydride or dihydride at room temperature.

5 Conclusion and Outlook

Inelastic H atom scattering from insulating, semiconducting and metallic surfaces yield qualitatively different results and the electronic character of a respective surface gives a distinct H atom energy-loss spectrum. Previous studies have shown that H atom scattering from insulating surfaces proceeds electronically adiabatically, while on metal surfaces, excitations of the phononic and electronic system are inextricably linked to each other [16, 154]. This work represents the first detailed study on inelastic H atom scattering from semiconducting surfaces and reveals an electronically non-adiabatic scattering channel leading to electronic interband excitations of the surface.

H atoms colliding with a $\text{Ge}(111)c(2 \times 8)$ surface transfer energy to either phonon excitation or – provided that the translational energy of the H atoms exceeds the surface band gap – electronic excitation of the surface. In the latter case, an electron is promoted across the surface band gap corresponding to an electronic interband excitation. This process contrasts with previous results found on metal surfaces, where relatively low-energetic intraband excitations constitute the most prominent energy-loss channel due to the metal's partly-filled electronic states around the Fermi level [16, 24]. In general, three different energy-loss channels can be identified for H atoms interacting with solid surfaces, schematically shown in Fig. 5.1: (1) electronically adiabatic energy transfer to phonon excitation, (2) non-adiabatic electronic interband excitations, and (3) non-adiabatic electronic intraband excitations. Energy-loss to phonon excitation is consistently observed, independent of the investigated surface sample and governed by classical collisional mechanics. Due to the H atom's low mass, which is typically much smaller than the mass of its surface atom collision partner, the phonon contribution to energy transfer is rather low. Non-adiabatic interband excitations are observed for band gap materials with energetically widely-separated electronic states. Induced by an impinging H atom, a single electron is promoted from an occupied electronic state to a vacant state, provided that enough energy is available. This energy threshold is the reason for the two energetically well-separated channels observed for H atoms scattering from $\text{Ge}(111)c(2 \times 8)$: low energy-loss to phonon excitation and high energy-loss to electronic interband excitation. Finally, if electronic intraband excitations are available and dominate the energy-loss of scattered H atoms, broad and structureless energy-loss

5 Conclusion and Outlook

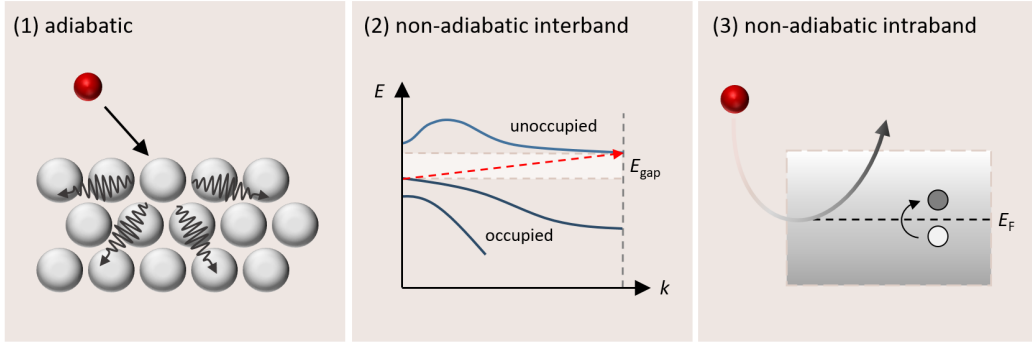


Figure 5.1: Schematics of three different energy transfer processes relevant to inelastic H atom scattering from semiconductor surfaces. (1) Electronically adiabatic energy transfer to phonon excitation. (2) Non-adiabatic electronic interband excitation promoting an electron from an occupied to an unoccupied electronic state. The exemplary electronic transition is indirect and requires momentum transfer to the electron, delivered by the impinging H atom. E is the energy, k is the wavevector and E_{gap} is the electronic (surface) band gap energy. (3) Non-adiabatic intraband excitation leading to an excited low-energy EHP. E_{F} is the Fermi level. The figure is adapted from Fig. 1 in Ref. [155].

distributions are observed. This applies to metal surfaces but also to the surfaces of semiconductors at high temperatures, where thermal occupation leads to partly-filled electronic states and intraband excitations become available. The observed energy-loss can be modeled with contributions of an insulating component capturing the energy-loss to phonons, a semiconductor component corresponding to interband excitations and a metal component describing electronic intraband excitations.

While it is well-known that photons can efficiently couple to the electronic system of semiconductors and induce electronic transitions, the physical mechanisms underlying electronic excitations induced by neutral H atom scattering are not yet understood. In particular, the high efficiency of the process is striking. A detailed theoretical model that can thoroughly reproduce experimental results is highly desired. Currently, adiabatic MD simulations performed on a high-dimensional neural network potential energy surface are available and quantitatively reproduce the energy-loss to phonon excitation but cannot describe the high energy-loss channel that involves non-adiabatic interband excitation. Electronic friction theories, which are able to capture electronic intraband excitations of metal surfaces in terms of a weak perturbation of the adiabatic description [16], failed to reproduce the energy-loss observed for H atoms scattering from Ge(111) $c(2 \times 8)$ at room temperature. Entailing a new level of BOA failure in atom-surface interactions, the H/Ge(111) $c(2 \times 8)$ system thus represents a challenge for theoretical models of electronically non-adiabatic effects.

Although no theoretical description is available to date, different experimental approaches have been used within this work to fortify and extend the understanding of energy transfer processes relevant to the $\text{H}/\text{Ge}(111)c(2 \times 8)$ system. Most strikingly, the non-adiabatic high energy-loss channel is only observed at incidence energies exceeding the band gap energy, whereas lower incidence energies lead to phonon excitation only. As long as the incidence energy exceeds the surface band gap, the non-adiabatic channel is observed and possesses an onset of the energy-loss that is coincident with the value of the surface band gap, independent of the respective incidence energy. Additionally, the isotope effect has been studied using both H and D atoms as impinging particles. As the efficiency of non-adiabatic processes often depends on the velocity of the involved particles, they can show strong isotope effects when substituting H with D atoms at equal translational energies [35, 36]. However, on $\text{Ge}(111)c(2 \times 8)$, nearly no isotope effect is observed for the non-adiabatic channel, suggesting that it is not determined by the particle's probability to induce non-adiabatic processes but by the probability to hit a specific surface site – $\text{Ge}(111)c(2 \times 8)$ has a complex surface structure with different types of surface atoms and localized surface states [71]. While there are sites where electronic interband excitation might not be possible or would require particularly large excitation energies, on other sites the electronic excitation probability could be close to 1 for both isotopes. The adiabatic scattering channel shows an isotope effect as expected for a purely mechanical interaction: the D atom is twice as heavy as the H atom and can therefore transfer more energy during a collision with a Ge surface atom. Apart from $\text{Ge}(111)c(2 \times 8)$, other germanium surfaces have been investigated in the course of this study, too, namely $\text{Ge}(100)(2 \times 1)$ and hydrogenated $\text{Ge}(111)(1 \times 1):\text{H}$. $\text{Ge}(100)(2 \times 1)$ is of metallic character at room temperature due to a partly-filled electronic surface state [86]. Nevertheless, electronic interband excitations are found to be the most prominent H atom energy-loss channel at room temperature and the obtained energy-loss distributions resemble those measured on $\text{Ge}(111)c(2 \times 8)$. Still, $\text{Ge}(100)(2 \times 1)$ seems to be more prone to electronic excitation than $\text{Ge}(111)c(2 \times 8)$. In contrast, hydrogenated $\text{Ge}(111)(1 \times 1):\text{H}$ possesses a wider surface band gap than $\text{Ge}(111)c(2 \times 8)$ [129, 133], which is reflected in the observed energy-loss of scattered H atoms. The non-adiabatic scattering channel is absent. Thus, H atom scattering from $\text{Ge}(111)(1 \times 1):\text{H}$ represents a promising system to investigate using electronically adiabatic MD simulations. Additionally, compared to $\text{Ge}(111)c(2 \times 8)$, the smaller surface unit cell of $\text{Ge}(111)(1 \times 1):\text{H}$ makes it an even better candidate for theoretical studies.

In the following paragraph, several ideas for future inelastic H atom scattering experiments are introduced. All of them are well suited to further verify the current

5 Conclusion and Outlook

interpretation of energy transfer processes relevant to H–Ge interactions and could be performed using the existing H atom scattering apparatus, requiring at most minor experimental modifications.

Firstly, the surface temperature dependent study on Ge(111) $c(2 \times 8)$ could be repeated using H atoms with a translational energy of $E_i = 0.37$ eV, i.e., lower than previously employed. At room temperature, only the adiabatic scattering channel is observed at this energy as the surface band gap of Ge(111) $c(2 \times 8)$ is 0.49 eV [81] and thus exceeds the available translational energy of the impinging H atoms, preventing electronic interband excitation. However, if the current interpretation is valid, a metal component would arise at elevated surface temperatures and its emergence would undoubtedly prove the availability of electronic intraband excitations in a semiconductor surface at sufficiently high surface temperatures. Of course, the surface band gap also shrinks with increasing temperature [114, 156] and it remains debatable whether a semiconductor component corresponding to interband excitations would arise too. Nevertheless, such a channel should possess a certain energy threshold, while electronic intraband excitations would overall shift and broaden the observed energy-loss distribution.

Secondly, H atoms with translational energies of $E_i = 0.37$ eV could be scattered from Ge(100)(2×1) at room temperature. Ge(100)(2×1) exhibits domains of different surface reconstructions that can be distinguished in terms of their electronic properties [86]. At $E_i = 0.37$ eV, electronic interband excitations should be possible on $c(4 \times 2)$ and $p(2 \times 2)$ domains, while the $p(2 \times 1)$ structure has a surface band gap of 0.5 eV, exceeding the available energy. The obtained results could be compared to Ge(111) $c(2 \times 8)$ that shows energy-loss to phonon excitation at $E_i = 0.37$ eV only. If electronic interband excitations were feasible in certain domains of Ge(100)(2×1), differences to the results obtained on Ge(111) $c(2 \times 8)$ would arise. The purely adiabatic scattering channel should be very similar on both Ge surface facets. However, the resolution at room temperature could be too low to observe marked differences. To solve this issue, Ge(100)(2×1) could also be investigated at low surface temperatures, offering a better energy resolution. Below a surface temperature of $T_S = 220$ K, the surface shows an ordered $c(4 \times 2)$ structure [96, 97], in principle allowing electronic interband excitations even at low H atom energies. By now, the lowest surface temperature used to record H atom energy-loss on Ge(100)(2×1) was $T_S = (142 \pm 19)$ K, showing no drastic difference to room temperature data. However, a sample holder that is specifically designed to allow experiments at even lower temperatures is currently being developed.

With better energy resolution, features corresponding to transitions between different electronic states may also become resolved in the energy-loss distributions of H atoms with higher initial translational energies. In this regard, it could also be promising to

record energy-loss distributions as a function of the incidence translational energy of the H atoms, for example by tuning the translational energy in small steps from around $E_i = 0.1$ eV up to $E_i = 7$ eV. With increasing energy, more and more electronic inter-band excitations should become accessible and might become resolved in the energy-loss spectra. Such an experiment could nicely illustrate the potential of inelastic H atom scattering as a technique to probe electronic structures of surfaces, although this is more involved experimentally. To generate H atom beams with various translational energies by photodissociation of hydrogen iodide precursor molecules, photolysis laser systems operating at a variety of photon energies would be required. For UV photolysis of HI [50], the available Nd:YAG pumped dye laser system could be used. To generate H atom beams with higher ($E_i > 4$ eV) and lower ($E_i < 0.5$ eV) translational energies, VUV photolysis via pre-dissociating Rydberg states [52] could be employed, equally using the dye laser system in combination with non-linear degenerate four-wave mixing. Alternatively, lower energies could be generated by vibrationally exciting the HI molecules prior to direct UV photodissociation. Vibrational excitation shifts the Franck-Condon region of the excitation so that lower parts of the repulsive states become accessible [157]. However, within this approach, an additional laser system to generate IR photons for vibrational excitation of HI would be required.

H atoms with high translational energies may induce additional energy dissipation processes in the Ge surface sample, for example electron emission or H^- formation. To detect negatively charged particles, another detector will be added to the H atom scattering machine soon. Detection of exoelectrons would undoubtedly prove that an amount of energy exceeding the work function of Ge, which is about 4.8 eV [158], can be transferred from an impinging H atom to a single electron within a semiconducting material like Ge. Moreover, electron emission probabilities represent convenient benchmark data for theoretical models.

Apart from Ge, other band gap materials could be investigated in future studies. Carbon (C) and silicon (Si) are lower homologs of Ge and elemental band gap materials with indirect bulk band gaps of 5.50 eV [159] and 1.13 eV [62], respectively, when crystallized in the diamond cubic lattice structure. For comparison, Ge has an indirect bulk band gap of 0.664 eV [63]. Compared to Ge, Si and C are lighter and impinging H atoms can transfer more energy in purely mechanical collisions. Thus, the adiabatic scattering channel should shift towards larger energy-losses, potentially complicating the separation to an electronically non-adiabatic high energy-loss channel. Nevertheless, Si is particularly interesting because of its tremendous technological relevance in the semiconductor industry, while diamond offers the possibility to study a wide band gap material. The (100) surfaces of diamond, Si and Ge possess similar (2×1)-type

5 Conclusion and Outlook

reconstructions due to the formation of surface dimers [65]. In contrast, the annealed (111) surfaces of Ge, Si and diamond show very diverse surface reconstructions at room temperature [160]. While Ge(111) exhibits a $c(2 \times 8)$ adatom structure [49], Si(111) shows a complex (7×7) dimer-adatom-stacking fault reconstruction [47, 48] and diamond(111) reconstructs to form a (2×1) π -bonded chain geometry [65], similar to the (2×1) tilted chain reconstructions found on Si(111) and Ge(111) following crystal cleavage at room temperature [65, 67]. Interestingly, the (7×7) reconstruction of Si(111) leads to a metallic character of the surface [161, 162], while the surface band-structure of diamond(111) (2×1) is semiconducting [65]. Thus, diamond(111) (2×1) should be well-suited to further study electronic interband excitations on semiconducting surfaces, whereas Si(111) (7×7) would offer another metallic surface to investigate, apart from Ge(100) (2×1) .

Beyond that, more general ideas for future investigations of semiconductor surfaces using inelastic H atom scattering include the technologically relevant oxygen-covered Si surfaces [65], n- and p-doped samples to study the effect of doping and compound semiconductors to further extend the range of band gap materials.

Based on the H atom scattering apparatus utilized in this work, two more atom-surface scattering machines have been developed and constructed in our research group; both of the machines could be used to study semiconductor surface samples, too. One of them produces short, sub-ns H atom pulses to be used in pump-probe style experiments to probe time-resolved surface dynamics [163, 164]. Moving away from H atoms as probing particles, the other surface scattering apparatus has been designed to perform inelastic carbon, nitrogen and oxygen atom scattering and has recently been installed at the *Dalian Coherent Light Source*. The free electron laser operates in the extreme ultraviolet wavelength region and will be used to generate high-energetic carbon, nitrogen and oxygen atoms via photodissociation of respective diatomic precursor molecules. Scattering from semiconducting surfaces, they may induce electronic excitations and provide further evidence of non-adiabatic interactions between atoms and band gap materials.

To conclude, inelastic H atom scattering experiments from Ge surfaces have the potential to contribute significantly to the debate on surface electronic excitations induced by atom or molecule scattering. Furthermore, they form the basis for a great many of new fascinating investigations that I believe will deeply strengthen our understanding of energy transfer processes between atoms and semiconductor surfaces.

List of Abbreviations

AES	Auger electron spectroscopy
AIMD	<i>ab-initio</i> molecular dynamics
ARPES	angle-resolved photoelectron spectroscopy
BOA	Born-Oppenheimer approximation
CB	conduction band
DFT	density-functional theory
DS	differential pumping stage
EANN	embedded-atom neural network
EEL	electron energy loss
EELS	electron energy loss spectroscopy
EF	electronic friction
E_F	Fermi level
EHP	electron-hole pair
fcc	face-centered cubic
Fig.	Figure
FWHM	full width at half maximum
FWM	four-wave mixing
GGA	generalized gradient approximation
HT	high-temperature
IESH	independent-electron surface hopping
IR	infrared
LDFA	local density friction approximation
LDOS	local density of states
LEED	low-energy electron diffraction
MCP	multichannel plate
MD	molecular dynamics
ML	monolayer
MT	moderate-temperature
Nd:YAG	neodymium-doped yttrium aluminum garnet
NN	neural network

List of Abbreviations

PAW	projector augmented wave
PBE	Perdew-Burke-Ernzerhof
PES	photoelectron/photoemission spectroscopy (in Chapter 2 and Section 4.3)
PES	potential energy surface (in Chapter 1 and Sections 4.1 and 4.2)
RAT	Rydberg atom tagging
Ref.	Reference
RMSE	root-mean-square error
SI	supplementary information
STM	scanning tunneling microscopy
STS	scanning tunneling spectroscopy
TDDFT	time-dependent density functional theory
TOF	time-of-flight
TPD	temperature programmed desorption
UHV	ultra-high vacuum
UV	ultraviolet
VASP	Vienna <i>ab initio</i> simulation package
VB	valence band
VBM	valence band maximum
VUV	vacuum-ultraviolet

Bibliography

- [1] I. Langmuir, A chemically active modification of hydrogen, *J. Am. Chem. Soc.* **1912**, *34*, 1310–1325, <https://doi.org/10.1021/ja02211a004>.
- [2] I. Langmuir, Part II.—"Heterogeneous reactions". Chemical reactions on surfaces, *Trans. Faraday Soc.* **1922**, *17*, 607–620, <https://doi.org/10.1039/TF9221700607>.
- [3] M. Born, R. Oppenheimer, Zur Quantentheorie der Molekeln, *Ann. Phys.* **1927**, *389*, 457–484, <https://doi.org/10.1002/andp.19273892002>.
- [4] J. Tully, Perspective on "Zur Quantentheorie der Molekeln", *Theor. Chem. Acc.* **2000**, *103*, 173–176, <https://doi.org/10.1007/s002149900049>.
- [5] J. C. Tully, Chemical dynamics at metal surfaces, *Annu. Rev. Phys. Chem.* **2000**, *51*, 153–178, <https://doi.org/10.1146/annurev.physchem.51.1.153>.
- [6] C. Díaz, R. A. Olsen, D. J. Auerbach, G. J. Kroes, Six-dimensional dynamics study of reactive and non reactive scattering of H₂ from Cu(111) using a chemically accurate potential energy surface, *Phys. Chem. Chem. Phys.* **2010**, *12*, 6499–6519, <https://doi.org/10.1039/C001956A>.
- [7] B. Jackson, S. Nave, The dissociative chemisorption of methane on Ni(100): Reaction path description of mode-selective chemistry, *J. Chem. Phys.* **2011**, *135*, 114701, <https://doi.org/10.1063/1.3634073>.
- [8] G. R. Darling, S. Holloway, Rotational motion and the dissociation of H₂ on Cu(111), *J. Chem. Phys.* **1994**, *101*, 3268–3281, <https://doi.org/10.1063/1.467574>.
- [9] J. E. Hurst, C. A. Becker, J. P. Cowin, K. C. Janda, L. Wharton, D. J. Auerbach, Observation of direct inelastic scattering in the presence of trapping-desorption scattering: Xe on Pt(111), *Phys. Rev. Lett.* **1979**, *43*, 1175–1177, <https://doi.org/10.1103/PhysRevLett.43.1175>.

Bibliography

- [10] J. E. Hurst, L. Wharton, K. C. Janda, D. J. Auerbach, Direct inelastic scattering Ar from Pt(111), *J. Chem. Phys.* **1983**, *78*, 1559–1581, <https://doi.org/10.1063/1.444847>.
- [11] B. D. Kay, T. D. Raymond, M. E. Coltrin, Observation of direct multiquantum vibrational excitation in gas-surface scattering: NH₃ on Au(111), *Phys. Rev. Lett.* **1987**, *59*, 2792–2794, <https://doi.org/10.1103/PhysRevLett.59.2792>.
- [12] P. Nieto, E. Pijper, D. Barredo, G. Laurent, R. A. Olsen, E.-J. Baerends, G.-J. Kroes, D. Farías, Reactive and nonreactive scattering of H₂ from a metal surface is electronically adiabatic, *Science* **2006**, *312*, 86–89, <https://doi.org/10.1126/science.1123057>.
- [13] H. Jiang, M. Kammler, F. Ding, Y. Dorenkamp, F. R. Manby, A. M. Wodtke, T. F. Miller III, A. Kandratsenka, O. Bünermann, Imaging covalent bond formation by H atom scattering from graphene, *Science* **2019**, *364*, 379–382, <https://doi.org/10.1126/science.aaw6378>.
- [14] E. K. Watts, J. L. W. Siders, G. O. Sitz, Vibrational excitation of NO scattered from Cu(110), *Surf. Sci.* **1997**, *374*, 191–196, [https://doi.org/10.1016/S0039-6028\(96\)01194-6](https://doi.org/10.1016/S0039-6028(96)01194-6).
- [15] Y. Huang, C. T. Rettner, D. J. Auerbach, A. M. Wodtke, Vibrational promotion of electron transfer, *Science* **2000**, *290*, 111–114, <https://doi.org/10.1126/science.290.5489.111>.
- [16] O. Bünermann, H. Jiang, Y. Dorenkamp, A. Kandratsenka, S. M. Janke, D. J. Auerbach, A. M. Wodtke, Electron-hole pair excitation determines the mechanism of hydrogen atom adsorption, *Science* **2015**, *350*, 1346–1349, <https://dx.doi.org/10.1126/science.aad4972>.
- [17] J. Werdecker, P. R. Shirhatti, K. Golibrzuch, C. Bartels, A. M. Wodtke, D. J. Harding, Electronically nonadiabatic vibrational excitation of N₂ scattered from Pt(111), *J. Phys. Chem. C* **2015**, *119*, 14722–14727, <https://doi.org/10.1021/acs.jpcc.5b00202>.
- [18] B. C. Krüger, S. Meyer, A. Kandratsenka, A. M. Wodtke, T. Schäfer, Vibrational inelasticity of highly vibrationally excited NO on Ag(111), *J. Phys. Chem. Lett.* **2016**, *7*, 441–446, <https://doi.org/10.1021/acs.jpcclett.5b02448>.

- [19] R. J. V. Wagner, B. C. Krüger, G. B. Park, M. Wallrabe, A. M. Wodtke, T. Schäfer, Electron transfer mediates vibrational relaxation of CO in collisions with Ag(111), *Phys. Chem. Chem. Phys.* **2019**, *21*, 1650–1655, <https://doi.org/10.1039/C8CP06041J>.
- [20] J. Geweke, A. M. Wodtke, Vibrationally inelastic scattering of HCl from Ag(111), *J. Chem. Phys.* **2020**, *153*, 164703, <https://doi.org/10.1063/5.0026228>.
- [21] A. M. Wodtke, J. C. Tully, D. J. Auerbach, Electronically non-adiabatic interactions of molecules at metal surfaces: Can we trust the Born–Oppenheimer approximation for surface chemistry?, *Int. Rev. Phys. Chem.* **2004**, *23*, 513–539, <https://doi.org/10.1080/01442350500037521>.
- [22] Y. Dorenkamp, H. Jiang, H. Köckert, N. Hertl, M. Kammler, S. M. Janke, A. Kandratsenka, A. M. Wodtke, O. Bünermann, Hydrogen collisions with transition metal surfaces: Universal electronically nonadiabatic adsorption, *J. Chem. Phys.* **2018**, *148*, 034706, <https://doi.org/10.1063/1.5008982>.
- [23] H. Jiang, Y. Dorenkamp, K. Krüger, O. Bünermann, Inelastic H and D atom scattering from Au(111) as benchmark for theory, *J. Chem. Phys.* **2019**, *150*, 184704, <https://doi.org/10.1063/1.5094693>.
- [24] A. Kandratsenka, H. Jiang, Y. Dorenkamp, S. M. Janke, M. Kammler, A. M. Wodtke, O. Bünermann, Unified description of H-atom-induced chemi-currents and inelastic scattering, *PNAS* **2018**, *115*, 680–684, <https://doi.org/10.1073/pnas.1710587115>.
- [25] N. Hertl, K. Krüger, O. Bünermann, Electronically nonadiabatic H atom scattering from low Miller index surfaces of silver, *Langmuir* **2022**, *38*, 14162–14171, <https://doi.org/10.1021/acs.langmuir.2c02140>.
- [26] J. K. Norskov, B. I. Lundqvist, Correlation between sticking probability and adsorbate-induced electron structure, *Surf. Sci.* **1979**, *89*, 251–261, [https://doi.org/10.1016/0039-6028\(79\)90611-3](https://doi.org/10.1016/0039-6028(79)90611-3).
- [27] M. Head-Gordon, J. C. Tully, Molecular dynamics with electronic frictions, *J. Chem. Phys.* **1995**, *103*, 10137–10145, <https://doi.org/10.1063/1.469915>.
- [28] W. Dou, J. E. Subotnik, Perspective: How to understand electronic friction, *J. Chem. Phys.* **2018**, *148*, 230901, <https://doi.org/10.1063/1.5035412>.

Bibliography

- [29] J. C. Tully, Molecular dynamics with electronic transitions, *J. Chem. Phys.* **1990**, *93*, 1061–1071, <https://doi.org/10.1063/1.459170>.
- [30] N. Shenvi, S. Roy, J. C. Tully, Nonadiabatic dynamics at metal surfaces: Independent-electron surface hopping, *J. Chem. Phys.* **2009**, *130*, 174107, <https://doi.org/10.1063/1.3125436>.
- [31] N. Shenvi, S. Roy, J. C. Tully, Dynamical steering and electronic excitation in NO scattering from a gold surface, *Science* **2009**, *326*, 829–832, <https://doi.org/10.1126/science.1179240>.
- [32] B. C. Krüger, N. Bartels, C. Bartels, A. Kandratsenka, J. C. Tully, A. M. Wodtke, T. Schäfer, NO vibrational energy transfer on a metal surface: Still a challenge to first-principles theory, *J. Phys. Chem. C* **2015**, *119*, 3268–3272, <https://doi.org/10.1021/acs.jpcc.5b00388>.
- [33] M. Lindenblatt, E. Pehlke, *Ab initio* simulation of the spin transition during chemisorption: H/Al(111), *Phys. Rev. Lett.* **2006**, *97*, 216101, <https://doi.org/10.1103/PhysRevLett.97.216101>.
- [34] M. S. Miziański, D. M. Bird, M. Persson, S. Holloway, Newns-Anderson model of chemisorption in H/Cu and H/Ag, *Surf. Sci.* **2008**, *602*, 2617–2622, <https://doi.org/10.1016/j.susc.2008.06.015>.
- [35] Y. Dorenkamp, C. Volkmann, V. Roddatis, S. Schneider, A. M. Wodtke, O. Bünermann, Inelastic H atom scattering from ultrathin aluminum oxide films grown by atomic layer deposition on Pt(111), *J. Phys. Chem. C* **2018**, *122*, 10096–10102, <https://doi.org/10.1021/acs.jpcc.8b02692>.
- [36] H. Nienhaus, H. S. Bergh, B. Gergen, A. Majumdar, W. H. Weinberg, E. W. McFarland, Electron-hole pair creation at Ag and Cu surfaces by adsorption of atomic hydrogen and deuterium, *Phys. Rev. Lett.* **1999**, *82*, 446–449, <https://doi.org/10.1103/PhysRevLett.82.446>.
- [37] B. Gergen, H. Nienhaus, W. H. Weinberg, E. W. McFarland, Chemically induced electronic excitations at metal surfaces, *Science* **2001**, *294*, 2521–2523, <https://doi.org/10.1126/science.1066134>.
- [38] P. Y. Yu, M. Cardona, *Fundamentals of semiconductors: Physics and materials properties*, Springer-Verlag, Heidelberg, Dordrecht, London, New York, **2010**.

- [39] A. Amirav, M. J. Cardillo, Electron-hole pair creation by atomic scattering at surfaces, *Phys. Rev. Lett.* **1986**, *57*, 2299–2302, <https://doi.org/10.1103/PhysRevLett.57.2299>.
- [40] P. S. Weiss, A. Amirav, P. L. Trevor, M. J. Cardillo, Hyperthermal gas-surface scattering, *J. Vac. Sci. Technol. A* **1988**, *6*, 889–894, <https://doi.org/10.1116/1.575069>.
- [41] A. Amirav, W. R. Lambert, M. J. Cardillo, P. L. Trevor, P. N. Luke, E. E. Haller, Electron-hole pair creation at a Ge(100) surface by ground-state neutral Xe atoms, *J. Appl. Phys.* **1986**, *59*, 2213–2215, <https://doi.org/10.1063/1.336361>.
- [42] B. C. Krüger, *From diatomic to polyatomic quantum-state-resolved molecule-surface scattering*, Dissertation, Georg-August-Universität Göttingen, **2017**.
- [43] A. Mödl, H. Robota, J. Segner, W. Vielhaber, M. C. Lin, G. Ertl, Rotational state distribution of NO molecules after interaction with germanium surfaces, *J. Chem. Phys.* **1985**, *83*, 4800–4807, <https://doi.org/10.1063/1.449006>.
- [44] F. Budde, A. Mödl, A. V. Hamza, P. M. Ferm, G. Ertl, State-resolved investigation of the dynamics of scattering and formation of NO at Ge surfaces, *Surf. Sci.* **1987**, *192*, 507–528, [https://doi.org/10.1016/S0039-6028\(87\)81143-3](https://doi.org/10.1016/S0039-6028(87)81143-3).
- [45] A. Mödl, T. Gritsch, F. Budde, T. J. Chuang, G. Ertl, Dynamics of NO molecular-beam scattering from a Ge surface, *Phys. Rev. Lett.* **1986**, *57*, 384–387, <https://doi.org/10.1103/PhysRevLett.57.384>.
- [46] T. Miyake, M. Sakai, H. Kato, T. Nakamura, A. Namiki, H. Kamba, T. Suzuki, Resonance-enhanced multiphoton ionization study of NO scattering from a corrugated Si(100) surface with oxygen coverage, *Jpn. J. Appl. Phys.* **1991**, *30*, 349–355, <https://dx.doi.org/10.1143/JJAP.30.349>.
- [47] K. Takayanagi, Y. Tanishiro, M. Takahashi, S. Takahashi, Structural analysis of Si(111)- 7×7 by UHV-transmission electron diffraction and microscopy, *J. Vac. Sci. Technol. A* **1985**, *3*, 1502–1506, <https://doi.org/10.1116/1.573160>.
- [48] K. Takayanagi, Y. Tanishiro, S. Takahashi, M. Takahashi, Structure analysis of Si(111)-(7×7) reconstructed surface by transmission electron diffraction, *Surf. Sci.* **1985**, *164*, 367–392, [https://doi.org/10.1016/0039-6028\(85\)90753-8](https://doi.org/10.1016/0039-6028(85)90753-8).
- [49] D. J. Chadi, C. Chiang, New c - 2×8 unit cell for the Ge(111) surface, *Phys. Rev. B* **1981**, *23*, 1843–1846, <https://doi.org/10.1103/PhysRevB.23.1843>.

Bibliography

- [50] S. R. Langford, P. M. Regan, A. J. Orr-Ewing, M. N. R. Ashfold, On the UV photodissociation dynamics of hydrogen iodide, *Chem. Phys.* **1998**, *231*, 245–260, [https://doi.org/10.1016/S0301-0104\(98\)00013-5](https://doi.org/10.1016/S0301-0104(98)00013-5).
- [51] P. M. Regan, S. R. Langford, A. J. Orr-Ewing, M. N. R. Ashfold, The ultraviolet photodissociation dynamics of hydrogen bromide, *J. Chem. Phys.* **1999**, *110*, 281–288, <https://doi.org/10.1063/1.478063>.
- [52] P. M. Regan, D. Ascenzi, E. Wrede, P. A. Cook, M. N. R. Ashfold, A. J. Orr-Ewing, Photodissociation and photoionization of highly excited HI molecules, *Phys. Chem. Chem. Phys.* **2000**, *2*, 5364–5374, <https://doi.org/10.1039/B005663O>.
- [53] S. Su, Y. Dorenkamp, S. Yu, A. M. Wodtke, D. Dai, K. Yuan, X. Yang, Vacuum ultraviolet photodissociation of hydrogen bromide, *Phys. Chem. Chem. Phys.* **2016**, *18*, 15399–15405, <https://doi.org/10.1039/C6CP01956K>.
- [54] L. Schnieder, W. Meier, K. H. Welge, M. N. R. Ashfold, C. M. Western, Photodissociation dynamics of H₂S at 121.6 nm and a determination of the potential energy function of SH(*A* ²Σ⁺), *J. Chem. Phys.* **1990**, *92*, 7027–7037, <https://doi.org/10.1063/1.458243>.
- [55] L. Schnieder, K. Seekamp-Rahn, F. Liedeker, H. Steuwe, K. H. Welge, Hydrogen exchange reaction H+D₂ in crossed beams, *Faraday Discuss. Chem. Soc.* **1991**, *91*, 259–269, <https://doi.org/10.1039/DC9919100259>.
- [56] F. Bechstedt, *Principles of surface physics*, Advanced texts in physics, Springer-Verlag, Berlin, Heidelberg, **2003**.
- [57] J. B. Hudson, *Surface science: an introduction*, A Wiley-Interscience publication, John Wiley & Sons, New York, Weinheim, **1998**.
- [58] R. E. Schlier, H. E. Farnsworth, Structure and adsorption characteristics of clean surfaces of germanium and silicon, *J. Chem. Phys.* **1959**, *30*, 917–926, <https://doi.org/10.1063/1.1730126>.
- [59] H. C. Gatos, Semiconductor electronics and the birth of modern science of surfaces, *Surf. Sci.* **1994**, *299/300*, 1–23, [https://doi.org/10.1016/0039-6028\(94\)90642-4](https://doi.org/10.1016/0039-6028(94)90642-4).
- [60] J. Bardeen, W. H. Brattain, The transistor, a semi-conductor triode, *Phys. Rev.* **1948**, *74*, 230–231, <https://doi.org/10.1103/PhysRev.74.230>.

- [61] B. S. Meyerson, High-speed silicon-germanium electronics, *Sci. Am.* **1994**, *270*, 62–67, <https://www.jstor.org/stable/24942626>.
- [62] W. Bludau, A. Onton, W. Heinke, Temperature dependence of the band gap of silicon, *J. Appl. Phys.* **1974**, *45*, 1846–1848, <https://doi.org/10.1063/1.1663501>.
- [63] G. G. MacFarlane, T. P. McLean, J. E. Quarrington, V. Roberts, Fine structure in the absorption-edge spectrum of Ge, *Phys. Rev.* **1957**, *108*, 1377–1383, <https://doi.org/10.1103/PhysRev.108.1377>.
- [64] J. F. C. Baker, M. Hart, An absolute measurement of the lattice parameter of germanium using multiple-beam X-ray diffractometry, *Acta Cryst.* **1975**, *A31*, 364–367, <https://doi.org/10.1107/S0567739475000769>.
- [65] W. Mönch, *Semiconductor surfaces and interfaces*, 3. edition, Springer series in surface sciences, Springer-Verlag, Berlin, Heidelberg, **2001**.
- [66] K. Oura, V. G. Lifshits, A. A. Saranin, A. V. Zotov, M. Katayama, *Surface science – An introduction*, Advanced texts in physics, Springer-Verlag, Berlin, Heidelberg, **2003**.
- [67] N. Takeuchi, A. Selloni, A. I. Shkrebtii, E. Tosatti, Structural and electronic properties of the $(111)2 \times 1$ surface of Ge from first-principles calculations, *Phys. Rev. B* **1991**, *44*, 13611–13617, <https://doi.org/10.1103/PhysRevB.44.13611>.
- [68] R. M. Feenstra, A. J. Slavin, Scanning tunneling microscopy and spectroscopy of cleaved and annealed Ge(111) surfaces, *Surf. Sci.* **1991**, *251/252*, 401–407, [https://doi.org/10.1016/0039-6028\(91\)91023-Q](https://doi.org/10.1016/0039-6028(91)91023-Q).
- [69] R. S. Becker, J. A. Golovchenko, B. S. Swartzentruber, Tunneling images of germanium surface reconstructions and phase boundaries, *Phys. Rev. Lett.* **1985**, *54*, 2678–2680, <https://doi.org/10.1103/PhysRevLett.54.2678>.
- [70] E. S. Hirschorn, D. S. Lin, F. M. Leibsle, A. Samsavar, T.-C. Chiang, Charge transfer and asymmetry on Ge(111)- $c(2 \times 8)$ studied by scanning tunneling microscopy, *Phys. Rev. B* **1991**, *44*, 1403–1406, <https://doi.org/10.1103/PhysRevB.44.1403>.
- [71] I. Razado-Colambo, J. He, H. M. Zhang, G. V. Hansson, R. I. G. Uhrberg, Electronic structure of Ge(111) $c(2 \times 8)$: STM, angle-resolved photoemission, and theory, *Phys. Rev. B* **2009**, *79*, 205410, <https://doi.org/10.1103/PhysRevB.79.205410>.

Bibliography

- [72] N. Takeuchi, A. Selloni, E. Tosatti, Do we know the true structure of Ge(111) $c(2 \times 8)$?, *Phys. Rev. Lett.* **1992**, *69*, 648–651, <https://doi.org/10.1103/PhysRevLett.69.648>.
- [73] P. V. Smith, M. W. Radny, G. A. Shah, Density functional study of the Ge(111) $c(2 \times 8)$ surface using the modified Becke-Johnson exchange potential with LDA correlation and spin-orbit interactions, *RSC Adv.* **2014**, *4*, 48245–48253, <https://doi.org/10.1039/C4RA05636A>.
- [74] R. D. Bringans, H. Höchst, Electronic structure of Ge(111) and Ge(111):H from angle-resolved-photoemission measurements, *Phys. Rev. B* **1982**, *25*, 1081–1089, <https://doi.org/10.1103/PhysRevB.25.1081>.
- [75] T. Yokotsuka, S. Kono, S. Suzuki, T. Sagawa, Study of electronic structures of Ge(111) 7×7 -Sn and Ge(111) " 2×8 " surfaces by angle-resolved UPS, *J. Phys. Soc. Japan* **1984**, *53*, 696–701, <https://doi.org/10.1143/JPSJ.53.696>.
- [76] J. M. Nicholls, G. V. Hansson, R. I. G. Uhrberg, New surface states on the annealed Ge(111) surface, *Phys. Rev. B* **1986**, *33*, 5555–5559, <https://doi.org/10.1103/PhysRevB.33.5555>.
- [77] R. D. Bringans, R. I. G. Uhrberg, R. Z. Bachrach, J. E. Northrup, Surface band dispersion of Ge(111) $c(2 \times 8)$ and Ge(111):As 1×1 , *J. Vac. Sci. Technol.* **1986**, *4*, 1380–1384, <https://doi.org/10.1116/1.573575>.
- [78] J. Aarts, A. J. Hoeven, P. K. Larsen, Electronic structure of the Ge(111)- $c(2 \times 8)$ surface, *Phys. Rev. B* **1988**, *37*, 8190–8197, <https://doi.org/10.1103/PhysRevB.37.8190>.
- [79] R. S. Becker, B. S. Swartzentruber, J. S. Vickers, T. Klitsner, Dimer-atom-stacking-fault (DAS) and non-DAS (111) semiconductor surfaces: A comparison of Ge(111)- $c(2 \times 8)$ to Si(111)- (2×2) , $-(5 \times 5)$, $-(7 \times 7)$, and $-(9 \times 9)$ with scanning tunneling microscopy, *Phys. Rev. B* **1989**, *39*, 1633–1647, <https://doi.org/10.1103/PhysRevB.39.1633>.
- [80] G. Lee, H. Mai, I. Chizhov, R. F. Willis, Voltage-dependent scanning tunneling microscopy images of the Ge(111)- $c(2 \times 8)$ surface, *J. Vac. Sci. Technol. A* **1998**, *16*, 1006–1009, <https://doi.org/10.1116/1.581222>.
- [81] R. M. Feenstra, J. Y. Lee, M. H. Kang, G. Meyer, K. H. Rieder, Band gap of the Ge(111) $c(2 \times 8)$ surface by scanning tunneling spectroscopy, *Phys. Rev. B* **2006**, *73*, 035310, <https://doi.org/10.1103/PhysRevB.73.035310>.

- [82] H. J. W. Zandvliet, The Ge(001) surface, *Phys. Rep.* **2003**, *388*, 1–40, <https://doi.org/10.1016/j.physrep.2003.09.001>.
- [83] J. A. Kubby, J. E. Griffith, R. S. Becker, J. S. Vickers, Tunneling microscopy of Ge(001), *Phys. Rev. B* **1987**, *36*, 6079–6093, <https://doi.org/10.1103/PhysRevB.36.6079>.
- [84] H. J. W. Zandvliet, B. S. Swartzentruber, W. Wulfhekel, B. J. Hattink, B. Poelsema, Spontaneous formation of an ordered $c(4 \times 2)-(2 \times 1)$ domain pattern on Ge(001), *Phys. Rev. B* **1998**, *57*, R6803–R6806, <https://doi.org/10.1103/PhysRevB.57.R6803>.
- [85] O. Gurlu, H. J. W. Zandvliet, B. Poelsema, Electronic properties of (2×1) and $c(4 \times 2)$ domains on Ge(001) studied by scanning tunneling spectroscopy, *Phys. Rev. Lett.* **2004**, *93*, 066101, <https://doi.org/10.1103/PhysRevLett.93.066101>.
- [86] F. Reichmann, E. Scalise, A. P. Becker, E. V. S. Hofmann, J. Dabrowski, F. Montalenti, L. Miglio, M. Mulazzi, W. M. Klesse, G. Capellini, New insights into the electronic states of the Ge(001) surface by joint angle-resolved photoelectron spectroscopy and first-principle calculation investigation, *Appl. Surf. Sci.* **2022**, *571*, 151264, <https://doi.org/10.1016/j.apsusc.2021.151264>.
- [87] M. Needels, M. C. Payne, J. D. Joannopoulos, High-order reconstructions of the Ge(100) surface, *Phys. Rev. B* **1988**, *38*, 5543–5546, <https://doi.org/10.1103/PhysRevB.38.5543>.
- [88] Y. Yoshimoto, Y. Nakamura, H. Kawai, M. Tsukada, M. Nakayama, Ge(001) surface reconstruction studied using a first-principles calculation and a Monte Carlo simulation, *Phys. Rev. B* **2000**, *61*, 1965–1970, <https://doi.org/10.1103/PhysRevB.61.1965>.
- [89] T. Sato, M. Iwatsuki, H. Tochiyama, Detection of the flip-flop motion of buckled dimers on a Ge(001) surface by STM, *J. Electron Microsc.* **1998**, *48*, 1–7, <https://doi.org/10.1093/oxfordjournals.jmicro.a023644>.
- [90] B. Röttger, T. Bertrams, H. Neddermeyer, Low-temperature scanning tunneling microscopy on vicinal Ge(100), *J. Vac. Sci. Technol. B* **1996**, *14*, 925–928, <https://doi.org/10.1116/1.589176>.
- [91] J. E. Griffith, J. A. Kubby, P. E. Wierenga, R. S. Becker, J. S. Vickers, Tunneling microscopy of steps on vicinal Ge(001) and Si(001) surfaces, *J. Vac. Sci. Technol. A* **1988**, *6*, 493–496, <https://doi.org/10.1116/1.575366>.

Bibliography

- [92] B. A. G. Kersten, H. J. W. Zandvliet, D. H. A. Blank, A. van Silfhout, Step structure of vicinal Ge(001) surfaces, *Surf. Sci.* **1995**, *322*, 1–7, [https://doi.org/10.1016/0039-6028\(95\)90011-X](https://doi.org/10.1016/0039-6028(95)90011-X).
- [93] S. J. Murray, M. Mian, F. M. Leibsle, R. McGrath, Defect- and contamination-induced pinning of higher-order reconstructions on Ge(001), *Surf. Sci.* **1994**, *307-309*, 741–746, [https://doi.org/10.1016/0039-6028\(94\)91486-9](https://doi.org/10.1016/0039-6028(94)91486-9).
- [94] P. C. Weakliem, G. W. Smith, E. A. Carter, Subpicosecond interconversion of buckled and symmetric dimers on Si(100), *Surf. Sci. Lett.* **1990**, *232*, L219–L223, [https://doi.org/10.1016/0039-6028\(90\)90112-L](https://doi.org/10.1016/0039-6028(90)90112-L).
- [95] E. Landemark, C. J. Karlsson, L. S. O. Johansson, R. I. G. Uhrberg, Electronic structure of clean and hydrogen-chemisorbed Ge(001) surfaces studied by photoelectron spectroscopy, *Phys. Rev. B* **1994**, *49*, 16523–16533, <https://doi.org/10.1103/PhysRevB.49.16523>.
- [96] S. D. Kevan, N. G. Stoffel, Metal-insulator transition on the Ge(001) surface, *Phys. Rev. Lett.* **1984**, *53*, 702–705, <https://doi.org/10.1103/PhysRevLett.53.702>.
- [97] S. D. Kevan, Surface states and reconstruction on Ge(001), *Phys. Rev. B* **1985**, *32*, 2344–2350, <https://doi.org/10.1103/PhysRevB.32.2344>.
- [98] L. Kipp, R. Manzke, M. Skibowski, An intrinsic metallic surface state on Ge(001) 2×1 , *Solid State Commun.* **1995**, *93*, 603–607, [https://doi.org/10.1016/0038-1098\(94\)00598-7](https://doi.org/10.1016/0038-1098(94)00598-7).
- [99] K. Nakatsuji, Y. Takagi, F. Komori, H. Kusunohara, A. Ishii, Electronic states of the clean Ge(001) surface near Fermi energy, *Phys. Rev. B* **2005**, *72*, 241308, <https://doi.org/10.1103/PhysRevB.72.241308>.
- [100] C. Jeon, C. C. Hwang, T.-H. Kang, K.-J. Kim, B. Kim, Y. Chung, C. Y. Park, Evidence from ARPES that the Ge(001) surface is semiconducting at room temperature, *Phys. Rev. B* **2006**, *74*, 125407, <https://doi.org/10.1103/PhysRevB.74.125407>.
- [101] H. Seo, R. C. Hatch, P. Ponath, M. Choi, A. B. Posadas, A. A. Demkov, Critical differences in the surface electronic structure of Ge(001) and Si(001): *Ab initio* theory and angle-resolved photoemission spectroscopy, *Phys. Rev. B* **2014**, *89*, 115318, <https://doi.org/10.1103/PhysRevB.89.115318>.

- [102] B. Yan, C. Yam, A. L. da Rosa, T. Frauenheim, Comment on "Valence Surface Electronic States on Ge(001)", *Phys. Rev. Lett.* **2009**, *103*, 189701, <https://doi.org/10.1103/PhysRevLett.103.189701>.
- [103] M. W. Radny, G. A. Shah, S. R. Schofield, P. V. Smith, N. J. Curson, Valence surface electronic states on Ge(001), *Phys. Rev. Lett.* **2008**, *100*, 246807, <https://doi.org/10.1103/PhysRevLett.100.246807>.
- [104] P. W. Palmberg, Structure transformations on cleaved and annealed Ge(111) surfaces, *Surf. Sci.* **1968**, *11*, 153–158, [https://doi.org/10.1016/0039-6028\(68\)90047-2](https://doi.org/10.1016/0039-6028(68)90047-2).
- [105] R. J. Phaneuf, M. B. Webb, A LEED study of Ge(111); A high-temperature incommensurate structure, *Surf. Sci.* **1985**, *164*, 167–195, [https://doi.org/10.1016/0039-6028\(85\)90706-X](https://doi.org/10.1016/0039-6028(85)90706-X).
- [106] Z. Gai, H. Yu, W. S. Yang, Adatom diffusion on Ge(111) and the corresponding activation energy barrier, *Phys. Rev. B* **1996**, *53*, 13547–13550, <https://doi.org/10.1103/PhysRevB.53.13547>.
- [107] R. M. Feenstra, A. J. Slavin, G. A. Held, M. A. Lutz, Surface diffusion and phase transition on the Ge(111) surface studied by scanning tunneling microscopy, *Phys. Rev. Lett.* **1991**, *66*, 3257–3260, <https://doi.org/10.1103/PhysRevLett.66.3257>.
- [108] X. Zeng, B. Lin, I. El-Kholy, H. E. Elsayed-Ali, Time-resolved reflection high-energy electron diffraction study of the Ge(111)- $c(2 \times 8)-(1 \times 1)$ phase transition, *Phys. Rev. B* **1999**, *59*, 14907–14910, <https://doi.org/10.1103/PhysRevB.59.14907>.
- [109] J. Aarts, A.-J. Hoeven, P. K. Larsen, Core-level study of the phase transition on the Ge(111)- $c(2 \times 8)$ surface, *Phys. Rev. B* **1988**, *38*, 3925–3930, <https://doi.org/10.1103/PhysRevB.38.3925>.
- [110] E. G. McRae, R. A. Malic, A new phase transition at the Ge(111) surface observed by low-energy electron diffraction, *Phys. Rev. Lett.* **1987**, *58*, 1437–1439, <https://doi.org/10.1103/PhysRevLett.58.1437>.
- [111] S. Modesti, V. R. Dhanak, M. Sancrotti, A. Santoni, B. N. J. Persson, E. Tosatti, High temperature surface metallization of Ge(111) detected by electron energy loss spectroscopy, *Phys. Rev. Lett.* **1994**, *73*, 1951–1954, <https://doi.org/10.1103/PhysRevLett.73.1951>.

Bibliography

- [112] N. Takeuchi, A. Selloni, E. Tosatti, Metallization and incomplete melting of a semiconductor surface at high temperature, *Phys. Rev. Lett.* **1994**, *72*, 2227–2230, <https://doi.org/10.1103/PhysRevLett.72.2227>.
- [113] A. Di Cicco, B. Giovanali, R. Gunella, E. Principi, S. Simonucci, Metallization of the Ge(111) surface at high-temperature probed by energy-loss and Auger spectroscopies, *Solid State Commun.* **2005**, *134*, 577–582, <https://doi.org/10.1016/j.ssc.2005.03.022>.
- [114] A. Goldoni, A. Santoni, M. Sancrotti, V. R. Dhanak, S. Modesti, Photoemission and photoabsorption study of the high-temperature phases of the Ge(111) surface, *Surf. Sci.* **1997**, *382*, 336–348, [https://doi.org/10.1016/S0039-6028\(97\)00207-0](https://doi.org/10.1016/S0039-6028(97)00207-0).
- [115] A. W. Denier van der Gon, J. M. Gay, J. W. M. Frenken, J. F. van der Veen, Order-disorder transitions at the Ge(111) surface, *Surf. Sci.* **1991**, *241*, 335–345, [https://doi.org/10.1016/0039-6028\(91\)90093-8](https://doi.org/10.1016/0039-6028(91)90093-8).
- [116] A. Mak, K. W. Evans-Lutterodt, K. Blum, D. Y. Noh, J. D. Brocl, G. A. Held, R. J. Birgeneau, Synchrotron x-ray diffraction study of the disordering of the Ge(111) surface at high temperatures, *Phys. Rev. Lett.* **1991**, *66*, 2002–2005, <https://doi.org/10.1103/PhysRevLett.66.2002>.
- [117] D. Farías, G. Lange, K. H. Rieder, J. P. Toennies, Helium scattering structure analyses of the $c(2 \times 8)$ reconstruction and the high-temperature (1×1) structures of Ge(111), *Phys. Rev. B* **1997**, *55*, 7023–7033, <https://doi.org/10.1103/PhysRevB.55.7023>.
- [118] C. A. Meli, E. F. Greene, G. Lange, J. P. Toennies, Evidence for an order-order transition on the Ge(111) surface near 1050 K from high-resolution helium atom scattering experiments, *Phys. Rev. Lett.* **1995**, *74*, 2054–2057, <https://doi.org/10.1103/PhysRevLett.74.2054>.
- [119] A. L. Glebov, J. P. Toennies, S. Vollmer, Behavior of single adatoms on the Ge(111) surface above the 1050 K phase transition, *Phys. Rev. Lett.* **1999**, *82*, 3300–3303, <https://doi.org/10.1103/PhysRevLett.82.3300>.
- [120] A. D. Johnson, C. Norris, J. W. M. Frenken, H. S. Derbyshire, J. E. MacDonald, R. G. van Silfhout, J. F. van der Veen, Combined $(1 \times 2) \rightarrow (1 \times 1)$ transition and atomic roughening of Ge(001) studied with surface x-ray diffraction, *Phys. Rev. B* **1991**, *44*, 1134–1138, <https://doi.org/10.1103/PhysRevB.44.1134>.

- [121] D. Cvetko, L. Floreano, A. Crottini, A. Morgante, F. Tommasini, Disordering of the Ge(001) surface studied by He atom scattering, *Surf. Sci.* **2000**, *447*, L147–L151, [https://doi.org/10.1016/S0039-6028\(99\)01205-4](https://doi.org/10.1016/S0039-6028(99)01205-4).
- [122] X. Zeng, H. E. Elsayed-Ali, Time-resolved electron diffraction study of the Ge(100)-(2 × 1)-(1 × 1) phase transition, *Surf. Sci.* **2002**, *497*, 373–384, [https://doi.org/10.1016/S0039-6028\(01\)01675-2](https://doi.org/10.1016/S0039-6028(01)01675-2).
- [123] E. van Vroonhoven, H. J. W. Zandvliet, B. Poelsema, (2 × 1)-(1 × 1) phase transition on Ge(100): dimer breakup and surface roughening, *Phys. Rev. Lett.* **2003**, *91*, 116102, <https://doi.org/10.1103/PhysRevLett.91.116102>.
- [124] E. van Vroonhoven, H. J. W. Zandvliet, B. Poelsema, A quantitative evaluation of the dimer concentration during the (2 × 1)-(1 × 1) phase transition on Ge(001), *Surf. Sci.* **2005**, *574*, L23–L28, <https://doi.org/10.1016/j.susc.2004.11.009>.
- [125] G. Le Lay, J. Kanski, P. O. Nilsson, U. O. Karlsson, K. Hricovini, Surface core-level shifts on Ge(100): $c(4 \times 2)$ to 2×1 and 1×1 phase transitions, *Phys. Rev. B* **1992**, *45*, 6692–6699, <https://doi.org/10.1103/PhysRevB.45.6692>.
- [126] L. Persichetti, A. Sgarlata, M. Fanfoni, A. Balzarotti, Irreversible order-disorder transformation of Ge(001) probed by scanning tunnelling microscopy, *J. Phys.: Condens. Matter* **2015**, *27*, 435001, <https://www.doi.org/10.1088/0953-8984/27/43/435001>.
- [127] A. Santoni, V. R. Dhanak, Electronic structure of the high-temperature Ge(100) surface studied by valence band photoemission, *Surf. Sci.* **2003**, *537*, L423–L428, [https://doi.org/10.1016/S0039-6028\(03\)00693-9](https://doi.org/10.1016/S0039-6028(03)00693-9).
- [128] J. J. Boland, Hydrogen as a probe of semiconductor surface structure: the Ge(111)- $c(2 \times 8)$ surface, *Science* **1992**, *255*, 186–188, <https://doi.org/10.1126/science.255.5041.186>.
- [129] A. J. Mayne, D. Riedel, G. Comtet, G. Dujardin, Atomic-scale studies of hydrogenated semiconductor surfaces, *Prog. Surf. Sci.* **2006**, *81*, 1–51, <https://doi.org/10.1016/j.progsurf.2006.01.001>.
- [130] G. Underwood, L. Keller Ballast, A. Champion, On the existence of a stable, room temperature dihydride-terminated Ge(100) surface in ultrahigh vacuum, *Surf. Sci.* **2008**, *602*, 2055–2060, <https://doi.org/10.1016/j.susc.2008.03.030>.

Bibliography

- [131] R. Imbihl, J. E. Demuth, F. J. Himpsel, P. M. Marcus, W. A. Thompson, F. Jona, Structure analysis of Ge(111) 1×1 -H by low-energy electron diffraction, *Phys. Rev. B* **1987**, *36*, 5037–5040, <https://doi.org/10.1103/PhysRevB.36.5037>.
- [132] C. Su, C.-S. Tsai, C.-E. Lin, K.-H. Chen, J.-K. Wang, J.-C. Lin, Interaction of atomic hydrogen with a Ge(111) surface: low-energy electron diffraction and surface Raman studies, *Surf. Sci.* **2000**, *445*, 139–150, [https://doi.org/10.1016/S0039-6028\(99\)00991-7](https://doi.org/10.1016/S0039-6028(99)00991-7).
- [133] L. Surnev, M. Tikhov, Comparative study of hydrogen adsorption on Ge(100) and Ge(111) surfaces, *Surf. Sci.* **1984**, *138*, 40–50, [https://doi.org/10.1016/0039-6028\(84\)90494-1](https://doi.org/10.1016/0039-6028(84)90494-1).
- [134] J. E. Crowell, G. Lu, The adsorption of hydrogen, digermane, and disilane on Ge(111): a multiple internal reflection infrared spectroscopy study, *J. Electron Spectrosc. Relat. Phenom.* **1990**, *54/55*, 1045–1057, [https://doi.org/10.1016/0368-2048\(90\)80294-K](https://doi.org/10.1016/0368-2048(90)80294-K).
- [135] T. Sakurai, H. D. Hagstrum, Study of clean and CO-covered Ge(111) surfaces by photoemission and ion-neutralization spectroscopies, *Phys. Rev. B* **1979**, *20*, 2423–2430, <https://doi.org/10.1103/PhysRevB.20.2423>.
- [136] I. Razado-Colambo, H. M. Zhang, R. I. G. Uhrberg, Electronic structure of H/Ge(111) 1×1 studied by angle-resolved photoelectron spectroscopy, *Phys. Rev. B* **2009**, *80*, 193403, <https://doi.org/10.1103/PhysRevB.80.193403>.
- [137] T. Klitsner, J. S. Nelson, Site-specific hydrogen reactivity and reverse charge transfer on Ge(111)- $c(2 \times 8)$, *Phys. Rev. Lett.* **1991**, *67*, 3800–3803, <https://doi.org/10.1103/PhysRevLett.67.3800>.
- [138] I. Razado-Colambo, H. M. Zhang, G. V. Hansson, R. I. G. Uhrberg, Hydrogen-induced metallization on Ge(111) $c(2 \times 8)$, *Appl. Surf. Sci.* **2006**, *252*, 5300–5303, <https://doi.org/10.1016/j.apsusc.2005.12.062>.
- [139] Y. J. Chabal, High-resolution infrared spectroscopy of adsorbates on semiconductor surfaces: hydrogen on Si(100) and Ge(100), *Surf. Sci.* **1986**, *168*, 594–608, [https://doi.org/10.1016/0039-6028\(86\)90890-3](https://doi.org/10.1016/0039-6028(86)90890-3).
- [140] J. A. Appelbaum, G. A. Baraff, D. R. Hamann, H. D. Hagstrum, T. Sakurai, Hydrogen chemisorption on the 100 (2×1) surfaces of Si and Ge, *Surf. Sci.* **1978**, *70*, 654–673, [https://doi.org/10.1016/0039-6028\(78\)90437-5](https://doi.org/10.1016/0039-6028(78)90437-5).

- [141] L. Papagno, X. Y. Shen, J. Anderson, G. Schirripa Spagnolo, G. J. Lapeyre, Hydrogen adsorption on Ge(100) studied by high-resolution energy-loss spectroscopy, *Phys. Rev. B* **1986**, *34*, 7188–7191, <https://doi.org/10.1103/PhysRevB.34.7188>.
- [142] O. Bünermann, H. Jiang, Y. Dorenkamp, D. J. Auerbach, A. M. Wodtke, An ultrahigh vacuum apparatus for H atom scattering from surfaces, *Rev. Sci. Instrum.* **2018**, *89*, 094101, <https://doi.org/10.1063/1.5047674>.
- [143] J. Czochralski, Ein neues Verfahren zur Messung der Kristallisationsgeschwindigkeit der Metalle, *Z. Phys. Chem.* **1918**, *92*, 219–221, <https://doi.org/10.1515/zpch-1918-9212>.
- [144] J. F. Ogilvie, Semi-experimental determination of a repulsive potential curve for hydrogen iodide, *Trans. Faraday Soc.* **1971**, *67*, 2205–2215, <https://doi.org/10.1039/TF9716702205>.
- [145] C. E. Brion, M. Dyck, G. Cooper, Absolute photoabsorption cross-sections (oscillator strengths) for valence and inner shell excitations in hydrogen chloride, hydrogen bromide and hydrogen iodide, *J. Electron Spectrosc. Relat. Phenom.* **2005**, *144-147*, 127–130, <https://doi.org/10.1016/j.elspec.2005.01.010>.
- [146] R. S. Mulliken, Low electronic states of simple heteropolar diatomic molecules: III. Hydrogen and univalent metal halides, *Phys. Rev.* **1937**, *51*, 310–332, <https://doi.org/10.1103/PhysRev.51.310>.
- [147] A. B. Alekseyev, H.-P. Liebermann, D. B. Kokh, R. J. Buenker, On the ultraviolet photofragmentation of hydrogen iodide, *J. Chem. Phys.* **2000**, *113*, 6174–6185, <https://doi.org/10.1063/1.1308552>.
- [148] G. N. A. van Veen, K. A. Mohamed, T. Baller, A. E. de Vries, Photofragmentation of HI in the first continuum, *Chem. Phys.* **1983**, *80*, 113–120, [https://doi.org/10.1016/0301-0104\(83\)85172-6](https://doi.org/10.1016/0301-0104(83)85172-6).
- [149] J. P. Marangos, N. Shen, H. Ma, M. H. R. Hutchinson, J. P. Connerade, Broadly tunable vacuum-ultraviolet radiation source employing resonant enhanced sum-difference frequency mixing in krypton, *J. Opt. Soc. Am. B* **1990**, *7*, 1254–1259, <https://doi.org/10.1364/JOSAB.7.001254>.
- [150] K. Krüger, Y. Wang, S. Tödter, F. Debbeler, A. Matveenko, N. Hertl, X. Zhou, B. Jiang, H. Guo, A. M. Wodtke, O. Bünermann, Hydrogen atom collisions with a semiconductor surface efficiently promote electrons to the conduction band, *Nat. Chem.* **2023**, *15*, 326–331, <https://doi.org/10.1038/s41557-022-01085-x>.

Bibliography

- [151] K. Krüger, Y. Wang, L. Zhu, B. Jiang, H. Guo, A. M. Wodtke, O. Bünermann, Isotope effect suggests site-specific nonadiabaticity on Ge(111) $c(2 \times 8)$, *Nat. Sci.* **2023**, e20230019, <https://doi.org/10.1002/ntls.20230019>.
- [152] K. Krüger, N. Hertl, A. M. Wodtke, O. Bünermann, Inelastic H atom scattering as a probe for the surface electronic structure of Ge(111), **2023**, (in preparation).
- [153] L. Pasquali, S. Nannarone, M. Canepa, L. Mattera, Surface electronic structure of Ge(111) from 300 to 1100 K by metastable deexcitation spectroscopy, *Phys. Rev. B* **1998**, *57*, 2507–2513, <https://doi.org/10.1103/PhysRevB.57.2507>.
- [154] N. Hertl, A. Kandratsenka, O. Bünermann, A. M. Wodtke, Multibounce and subsurface scattering of H atoms colliding with a van der Waals solid, *J. Phys. Chem. A* **2021**, *125*, 5745–5752, <https://doi.org/10.1021/acs.jpca.1c03433>.
- [155] H. Nienhaus, Mysterious energy losses, *Nat. Chem.* **2023**, *15*, 301–302, <https://doi.org/10.1038/s41557-023-01145-w>.
- [156] J. E. Demuth, R. Imbihl, W. A. Thompson, Temperature-dependent electronic excitations of the Ge(111)- 2×1 surface, *Phys. Rev. B* **1986**, *34*, 1330–1332, <https://doi.org/10.1103/PhysRevB.34.1330>.
- [157] J. P. Camden, H. A. Bechtel, D. J. Ankeny Brown, A. E. Pomerantz, R. N. Zare, R. J. Le Roy, Probing excited electronic states using vibrationally mediated photolysis: Application to hydrogen iodide, *J. Phys. Chem. A* **2004**, *108*, 7806–7813, <https://doi.org/10.1021/jp049051z>.
- [158] J. A. Dillon, H. E. Farnsworth, Work-function studies of germanium crystals cleaned by ion bombardment, *J. Appl. Phys.* **1957**, *28*, 174–184, <https://doi.org/10.1063/1.1722701>.
- [159] F. J. Himpsel, J. A. Knapp, J. A. VanVechten, D. E. Eastman, Quantum photoyield of diamond(111) – A stable negative-affinity emitter, *Phys. Rev. B* **1979**, *20*, 624–627, <https://doi.org/10.1103/PhysRevB.20.624>.
- [160] F. Bechstedt, A. A. Stekolnikov, J. Furthmüller, P. Käckell, Origin of the different reconstructions of diamond, Si, and Ge(111) surfaces, *Phys. Rev. Lett.* **2001**, *87*, 016103, <https://doi.org/10.1103/PhysRevLett.87.016103>.
- [161] U. Backes, H. Ibach, Evidence for a 2D-metallic state of the clean 7×7 Si(111) surface, *Solid State Commun.* **1981**, *40*, 575–577, [https://doi.org/10.1016/0038-1098\(81\)90577-9](https://doi.org/10.1016/0038-1098(81)90577-9).

- [162] R. J. Hamers, R. M. Tromp, J. E. Demuth, Surface electronic structure of Si(111)-(7 × 7) resolved in real space, *Phys. Rev. Lett.* **1986**, *56*, 1972–1975, <https://doi.org/10.1103/PhysRevLett.56.1972>.
- [163] S. Kaufmann, D. Schwarzer, C. Reichardt, A. M. Wodtke, O. Bünermann, Generation of ultra-short hydrogen atom pulses by bunch-compression photolysis, *Nat. Commun.* **2014**, *5*, 5373, <https://doi.org/10.1038/ncomms6373>.
- [164] K. Golibrzuch, V. Walpole, A.-M. Schönemann, A. M. Wodtke, Generation of subnanosecond H atom pulses for scattering from single-crystal epitaxial graphene, *J. Phys. Chem. A* **2022**, *126*, 8101–8110, <https://doi.org/10.1021/acs.jpca.2c05364>.

Acknowledgments

I started working on my PhD thesis in the group of Prof. Dr. Alec Wodtke in 2018 and right from the beginning, I enjoyed the particularly welcoming and inspiring atmosphere in his research group. A lot of people have played a role in making the last few years unique and unforgettable for me and in the following I want to express my deep gratitude to all of you.

First of all, I would like to thank my thesis advisor Prof. Dr. Alec Wodtke for giving me the opportunity to work in his research group on an exceedingly interesting project. Alec, I would like to thank you for all of your advice and motivation as well as the freedom you gave me to work on a project that became a matter of the heart to me. I feel honoured to have learned a lot about surface science and science in general from you.

Secondly, I would like to thank Prof. Dr. Dirk Schwarzer for being the second reviewer of this work as well as the other members of the examination board, Prof. Dr. Burkhard Geil, Prof. Dr. Christian Jooß, J. Prof. Dr. Daniel Obenchain and Prof. Dr. Martin Suhm.

A great thank-you goes to my supervisor and project leader PD Dr. Oliver Bünermann. Oliver was not only my supervisor during the time of my PhD thesis but also already during my bachelor's and master's theses. Thank you for teaching me basically everything I know in the lab, be it ultra-high vacuum systems, lasers or complex surface scattering experiments. Thank you for your willingness to immediately discuss new interesting and – sometimes – surprising results, your motivation and all your helpful advice in both data analysis and preparation of this thesis. Last but not least, I would like to say thanks for lots of much-needed cake-breaks in the afternoon during which we could continue to discuss scientific problems if we weren't talking about new sportive activities and challenges.

Many thanks go to our collaborators Prof. Dr. Hua Guo, Prof. Dr. Bin Jiang, Dr. Yingqi Wang, Dr. Sascha Kandratsenka and Dr. Nils Hertl for providing theoretical

Acknowledgments

calculations on H atom scattering from semiconductor and metal surfaces as well as lots of fruitful discussions. It was a pleasure to work with all of you. Moreover, I would like to thank all members of the collaborative research center 1073 for constructive scientific exchange.

For proofreading this thesis, I kindly thank Dr. Oliver Bünermann, Dr. Roman Wagner and Emma Elsdon.

I would like to thank all members of the Wodtke group for the friendly atmosphere, for the tremendous joint knowledge on surface science and for the willingness to always provide a helping hand if it is needed in the lab. Moreover, I will never forget our group barbecues and hiking trips in the summer time as well as the Christmas parties and skiing trips in the winter. Special thanks go to my colleagues and friends Emma Elsdon, Dr. Georg Westphal, Dr. Sven Meyer, Dr. Bastian Krüger, Dr. Rasika Dissanayake and Tim Diedrichs for your help and support but also for our joint trips and holidays and lots of happy moments that enriched my life during the past few years.

I would like to thank my predecessors working on the RAT Machine, Dr. Yvonne Dorenkamp and Dr. Hongyan Jiang for introducing me to the experiment as well as all the Bachelor and Master students I worked with during the time of my PhD thesis: Henri Schmerberg, Malte Opfermann, Felix Debbeler, Anna Matveenko and Sophia Tödter. Sophia is my successor working on the H atom scattering project and I wish her all the best for her PhD thesis and a successful time working on the RAT machine.

Talking about the RAT machine, I feel like I should also express my gratitude to this apparatus, especially as we often jokingly talked about its unique personality and obstinacy. For me, however, it was a pleasure to work on such a complex machine and to try to keep all systems running, to extend, repair and improve the apparatus over the years.

I appreciate any kind of support by the CRC 1073 secretary Friederike Schnelle and coordinator Dr. Jörg Hoffmann, by the IPC manager Dr. Markus Hold, by the secretaries Ilke Haase and Nektaria Saridaki and by the IPC technical staff Clemens Heymann, Josef Schikowski and Norbert Neisen. Special thanks go to the staff of the electronics and mechanics workshops, especially Mike Zippert and Reinhard Hildebrandt. It was a great experience to design the new transfer chamber, which was manufactured at the fine mechanics workshop. Moreover, I would like to thank the technicians Reinhard Bürsing and Tim Diedrichs for many valuable tips and help in the lab.

Acknowledgments

Special thanks go to my friends Kristin Fricke, Dana Dedeck and Julia Büschges. Thank you for lots of unforgettable moments as well as your continuous support, understanding and motivation.

Last but not least, I would like to thank my family, especially my sister Judith Krüger for both challenging and supporting me during my whole life. I would like to thank my grandpa Günter Bartels for unlimited patience, trust and love. Special thanks go to my partner Roman Wagner for countless discussions and all your support. Finally, I would like to thank my parents Gabriele Bartels-Krüger and Bernd Krüger for their encouragement, patience and confidence as long as I can remember. I am more than thankful that both of you opened my eyes for the fascinating world we are living in and piqued my interest in natural sciences.

List of Publications

1. K. Krüger, Y. Wang, L. Zhu, B. Jiang, H. Guo, A. M. Wodtke, O. Bünermann, Isotope effect suggests site-specific nonadiabaticity on Ge(111) $c(2 \times 8)$, *Nat. Sci.* **2023**; e20230019, <https://doi.org/10.1002/ntls.20230019>.
2. K. Krüger, Y. Wang, S. Tödter, F. Debbeler, A. Matveenko, N. Hertl, X. Zhou, B. Jiang, H. Guo, A. M. Wodtke, O. Bünermann, Hydrogen atom collisions with a semiconductor surface efficiently promote electrons to the conduction band, *Nat. Chem.* **2023**, *15*, 326-331, <https://doi.org/10.1038/s41557-022-01085-x>.
3. N. Hertl, K. Krüger, O. Bünermann, Electronically nonadiabatic H atom scattering from low Miller index surfaces of silver, *Langmuir* **2022**, *38*, 14162-14171, <https://doi.org/10.1021/acs.langmuir.2c02140>.
4. H. Jiang, Y. Dorenkamp, K. Krüger, O. Bünermann, Inelastic H and D atom scattering from Au(111) as benchmark for theory, *J. Chem. Phys.* **2019**, *150*, 184704, <https://doi.org/10.1063/1.5094693>.
5. M. A. Beckett, S. J. Coles, P. N. Horton, C. L. Jones, K. Krüger, Synthesis, XRD studies and NLO properties of $[p - \text{H}_2\text{NC}_6\text{H}_4\text{CH}_2\text{NH}_3] [\text{B}_5\text{O}_6(\text{OH})_4] \cdot 1/2 \text{H}_2\text{O}$ and NLO properties of some related pentaborate(1⁻) salts, *J. Clust. Sci.* **2017**, *28*, 2087-2095, <https://doi.org/10.1007/s10876-017-1205-1>.
6. J. Altnöder, K. Krüger, D. Borodin, L. Reuter, D. Rohleder, F. Hecker, R. A. Schulz, X. T. Nguyen, H. Preiß, M. Eckhoff, M. Levien, M. A. Suhm, The guinness molecules for the carbohydrate formula, *Chem. Rec.* **2014**, *14*, 1116-1133, <https://doi.org/10.1002/tcr.201402059>.